UILU-ENG-76-2026

CIVIL ENGINEERING STUDIES
STRUCTURAL RESEARCH SERIES NO. 435

NONLINEAR ANALYSIS OF INTERSECTING CYLINDERS BY THE FINITE ELEMENT METHOD
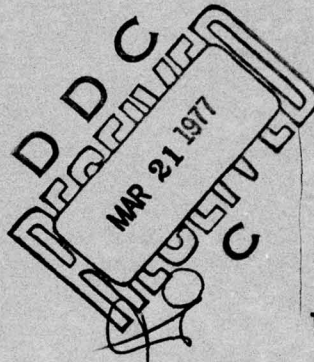
By
H. C. CHEN
W. C. SCHNOBRICH

D D C
MAR 21 1977

UNIVERSITY OF ILLINOIS
AT URBANA-CHAMPAIGN
URBANA, ILLINOIS
DECEMBER 1976

NONLINEAR ANALYSIS OF INTERSECTING CYLINDERS
BY THE FINITE ELEMENT METHOD

By

H. C. Chen

W. C. Schnobrich

UNIVERSITY OF ILLINOIS
AT URBANA-CHAMPAIGN
URBANA, ILLINOIS

December 1976

ii

ACKNOWLEDGMENT

iv

TABLE OF CONTENTS

LIST OF FIGURES

CHAPTER 1

INTRODUCTION

1.1 General

Elastic analysis produces satisfactory results when the
loading develops stress below the elastic limit. But it obviously begins
to experience trouble in predicting the structural behavior once the
yield stress has been exceeded. For intersecting cylinders, a stress
concentration exists in the vicinity of the intersection curve. It is
therefore impractical or at least uneconomical to let this concentration
control the design while retaining the same allowable stress throughout
the whole structure unless that concentrated stress critically determines
the failure load. Actually, to tolerate a small amount of plastic
deformation in the region of high stress gradient helps the material to
accommodate the imposed distortion pattern and smooths out the stress
concentration as long as the material is ductile and no fatigue crack
occurs. For structures operating in a high pressure state or for large
diameter intersecting cylinders, this allowance saves material and serves
as a safety valve. Design procedures based on this principle have been
formalized, for example, the ASME Pressure Vessel Code [1] allows self-
equilibrating thermal stresses calculated by elastic procedures to be up
to twice the value of the yield stress. However, the accurate and detailed
determination of the stresses in the vicinity of the intersection region
of the cylinders would be of little value unless the designer recognized
the significance of those stresses in relation to failure. A better
understanding of the post-elastic behavior and the possibility of achieving

a more reliable design of the cylindrical intersections can be obtained from a plastic analysis.

Cylinder-to-cylinder intersections are a very common occurrence in many industrial applications such as boilers, pressure vessels, pipe connections, etc. However, until only a few years ago most of the research investigations reported in the literature were limited to experimental work. Recently analytical treatment of this subject area has been given some attention. Most of this recent work is still incomplete [2].

Difficulties in obtaining analytical evaluations of the stress distributions in the disturbed regions near the intersection of comparable size shells originally stemmed from the complicated geometrical shape of the intersection line. The intersection curve of the middle surfaces of the cylinders is neither rotational symmetric nor on a plane curve but rather is a spacial curve. Early efforts required one cylinder to be of a much smaller diameter in comparison to the cylinder that it is intersecting so that the intersection curve could be approximated by a circle, thus simplifying the problem. Besides, the sharp discontinuities of curvatures across the intersection curve function as a stress raiser. Therefore, the presence of the stress concentration is inevitable and, as a consequence, constitutes a major consideration in the design.

With the aid of high-speed digital computers, numerical solutions are now playing a significant role in obtaining solutions to engineering applications. During the past decade, the development of the finite element method has increased markedly the capability of engineering problem solving. Many complicated design problems which were considered

unfeasible to a realistic analysis several years ago can now be solved almost routinely by using the finite element method. The method provides a powerful tool to attack shell structures and has been applied lately to evaluate the stress distribution for intersecting cylinders [3]. By subdividing the whole structure into a finite number of regions, referred to as the "elements", it has the advantage of being able to adjust to complicated configurations and irregular geometrical boundaries. Therefore the troublesome boundary conditions along the intersection curve of intersecting shells is effectively overcome. In addition, the finite element method is a very convenient and efficient method for programming for electronic computers compared with other numerical methods [4].

One of the most advantageous applications of the finite element method is to nonlinear problems. Nonlinear behavior can occur in two different forms. The first is material nonlinearity which arises because of the material possessing nonlinear constitutive laws. The second is geometric nonlinearity. This nonlinearity is associated with large displacements that cause sufficiently large changes in the geometry of the structure that the deformed configuration is used when writing the equilibrium conditions. Superposition techniques are no longer valid for loadings increased beyond the proportional limit. However, with the aid of incremental or iterative techniques, the finite element method can handle both of these two different categories of nonlinearities without major changes in numerical procedures.

Accuracy and efficiency are two considerations, even essential issues, that enter into the development of computer programs that are to be applied to large nonlinear problems. For intersecting cylinders, since

a large amount of core storage (or input-output operations if secondary devices are used) and computational efforts are required for the nonlinear solutions, special techniques such as the reduced integration concept should be considered to make the problem tractable in a practical sense. Very little mathematical development of the reduced integration technique has been published to date. Most publications have centered around a demonstration rather than a development.

1.2 Objective and Scope

It is the object of this study to develop a general procedure for nonlinear analysis of intersecting cylinders. The finite element method is selected for its high efficiency and convenience in computer work.

The progression of yield is of particular interest in this study. The three-dimensional isoparametric elements are layered through the thickness of the intersecting cylinders in the region where the high stress gradieint exists while two-dimensional curved shell elements are used throughout the remainder of the structure. Transitional elements are employed to connect these dissimilar three-dimensional and shell elements together.

Since small deformations are assumed, only the material nonlinearity is considered. The study is limited to isotropic, homogeneous materials with elastic, linear strain-hardening behavior. Isotropic strain hardening is applied with monotonically increasing loadings. In the plastic range, a mixed incremental-iterative method is included in the stress analysis. The Von Mises yield criterion is

used to predict the nonlinearity of elements. The reduced integration technique is also employed to economize on computer operations.

The reliability and the effectiveness of the procedure are verified by solving several examples. Finally, a problem of two normally intersecting cylinders subjected to increasing internal pressure is solved. The stresses at the outer and inner fibers of the shells are evaluated and compared with available experimental data.

1.3 Notations

$[A]$ = T3D transformation matrix (Appendix A)

$[B]$, $[B']$ = matrix relating nodal displacement and strains, based on global and local coordinate systems

$[C]$, $[C_s]$ = transformation matrix for 3D and shell transition elements, respectively

$[D]$, $[D']$ = material property matrix in global and local coordinates

$[D_{ep}]$ = incremental stress-strain relations

D = diameter of the main cylindrical shell

d = diameter of the branch pipe

E = modulus of elasticity

f_a = average stress concentration factor

f_b = correction factor when bending stresses are included

f_c = stress concentration factor of normally intersecting cylinders

f_i = body force components

$[G^U]$, $[G^L]$ = upper and lower triangular matrices of the structural stiffness matrix

G, G' = effective area of the main cylinder and the branch pipe, respectively

$H = d\bar{\sigma}/d\bar{\epsilon}^P$

[I] = unit diagonal matrix

[J], |J| = Jacobin and determinant of Jacobin

J_2, J_3 = the second and the third invariant of stress deviator

[K_c] = initial elastic stiffness matrix

[K'] = the stiffness caused by nonlinearity of material

[K] = element stiffness matrix

[K_s] = stiffness matrix of Ahmad's shell element

[K_T] = stiffness matrix of shell transitional element

K = element stiffness matrix, and the hardening parameter

M_β, M_α = applied moments along the x', y' axes

[N], [N*] = shape functions in curvilinear coordinates for 3D element and shell element, respectively

$\underline{P}$ = generalized load vector

P = internal pressure

$\{\Delta P\}_n$ = residual nodal forces at nth iteration

$\{\Delta P\}$ = applied load increment

$\{P\}$ = load vector

$P_o = 4b\sigma_o$

Q = distributed surface load

R = radius of the main cylinder also residual nodal forces

r = radius of the branch pipe

S_{ij} = stress deviator tensor

S = nominal hoop stress of the main cylinder, r/R, and Ahmad's shell element

s = nominal hoop stress of the branch pipe

ST = shell transitional element

T_i = surface traction

T = thickness of the main cylinder

t = thickness of the branch pipe

T3D = three-dimensional transitional element

$\underline{u}$ = nodal displacement vector

$u_{top}, u_{bot}, u_{mid}$ = displacement components of the top, the bottom, and the mid-nodes on the interface of T3D element

U_{AB} = displacement variation along the edge AB

$\overline{U}$ = nodal displacement vector excluding those on the interface of T3D element

U_A, U_B, U_C = nodal displacement at nodes A, B, C

$\overline{U}_C$ = departure displacement of node C (Fig. 4)

u, v, w = components of displacement in the X, Y, Z directions

u', v', w' = components of displacement in the x', y', z' directions

ΔU = incremental displacement vector

V = volume of a given solid domain

$\overline{V}_1, \overline{V}_2, \overline{V}_3$ = unit direction vector in the x', y', z' directions, respectively

W_o^* = the center or the tip deflection when yielding starts

W_o = the center (or the tip) deflection of simply supported beam (or cantilevered beam)

x, y, z = global coordinate system

x', y', z' = local coordinate system

$\underline{\varepsilon}$ = strain vector

$\{\varepsilon\}, \{\varepsilon'\}$ = strain vector in global and local coordinates, respectively

ξ, η, ζ = curvilinear coordinates

β, α = rotations about the x', y' axes

δW = virtual work

σ_{ij} = stress tensor

$d\sigma_{ij}, \Delta\sigma_{ij}$ = stress increment

σ_o = initial yield stress in simple tensile test

$\overline{\sigma}, \Delta\overline{\sigma}$ = effective stress and effective stress increment, respectively

σ_r = normal stress of cylindrical shell

$\{d\varepsilon_e\}$ = elastic strain increment

$\{d\varepsilon^P\}$ = plastic strain increment

$d\overline{\varepsilon}^P$ = effective plastic strain increment

$d\lambda$ = nonnegative constant

γ = the rate of convergence

λ_o = step length

ρ = nondimensional load parameter

μ = Poisson's ratio

$[\theta]$ = direction cosine matrix $[\overline{V}_1, \overline{V}_2, \overline{V}_3]$

δ = distance as defined in Fig. 1

α = linear interpolation factor, intersection angle of intersecting cylinders

3D = three-dimensional element

CHAPTER 2

THE STRESS ANALYSIS OF INTERSECTING CYLINDERS

2.1 Previous Work

Intersecting cylinders can occur in a variety of engineering applications. Therefore, a number of engineering solutions have been sought for these problems using different approaches such as experimental, analytical, or numerical methods. These procedures have been performed to investigate both the stress distribution and the structural behavior of such intersecting shells. The previous work directed to this problem is grouped and summarized below.

2.1.1 Experimental Work

Experiments conducted on the intersection region can commonly be classed within two broad categories.

A. Metal Specimens

This application consists of measuring the surface strains at some particular points on an actual shell or a scale model machined or milled out of metal. Mechanical or electrical resistance strain gages are used for this purpose. Experimental studies conducted by Mehringer [5] and Cranch [6] have been published. The work presented by Corum [7] represents some recent careful experiments. This latter study is well documented and has already been referred to by other researchers. Electrical resistance strain gages were used on both the inner and outer surfaces of the models in the test series. The series involved four

models that had different geometric variables and were subjected to various loading patterns, including internal pressure and end forces on the nozzle.

Strain gages were placed in two opposite quadrants. Each quadrant had four lines of gages which ran along the nozzle then when on the cylinder radiated from the junction. The space between two gages on each line was based on the anticipated stress concentration and on the distance from function. The test results were compared with theoretical predictions derived from a finite element solution obtained by using flat triangular elements.

B. Photoelasticity

This method gives an overall picture of stress distribution. The differences of principal stresses are optically measured from isotropic transparent models which become doubly refractive when polarized light is passed through the model. The newly developed freeze techniques are available for three-dimensional models. Upon the completion of the "stress freezing" operation, slices are removed from the model and then the stresses are determined by standard photoelastic techniques.

Schneider [8] tested a series of intersecting cylinders which were made of epoxy resin and subjected to internal pressure. Stress concentration factors, or stress indices, were investigated by these photoelastic tests. Taylor [9] conducted a three-dimensional photoelastic study of stresses around reinforced branch pipe intersections. Taniguchi and Kono [10] described the results of an experimental analysis of the nozzle to vessel attachment under external loadings by means of the

three-dimensional photoelastic method.

2.1.2 Analytical Analysis

The complicated geometrical shape of the intersecting line between normally intersecting cylinders creates a difficulty in solving the problem analytically. However, the problem can be greatly simplified if the diameter ratio between the branch shell and the main shell is small. The main shell can be treated as a shallow shell, so Donnell's equation is applicable. The end section of the branch pipe can be looked upon as flat. Therefore standard solutions for cylindrical shells such as those presented by Flugge [11] can be used directly.

Reidelback [12] made the above assumptions and derived a simplified differential equation to examine the influence of internal pressure on the elastic behavior of the intersection region. In his work, formulas are given for the case of both cylinders of equal diameter even though the procedure is valid only for very small diameter ratios.

Later, Eringen and Suhubi [13] used Donnell's equation for both shells to attack the same problem, and established a set of eight boundary conditions along the intersection curve. These conditions are used to determine the unknown constants of the analytical solution. The diameter ratio of the intersecting cylinders was limited to less than one-third. Unfortunately, no numerical example was presented in that article.

Bijlarrd, Dohrmann and Wang [14] presented results for the case when the intersecting cylinders were of equal diameter. Thick shells were considered and shear deformations were also taken into account. Flugge's equations were applied to both cylinders in the

development of the solution process. No numerical results were presented in that study either.

For an arbitrary diameter ratio of normally intersecting shells, Pan and Beckett [15] formulated their resulting equations on the basis of a general elastic thin shell theory. Donnell's and Flugge's equations were used for main and branch cylinders, respectively. The numerical example for the diameter ratio 1:2 was selected to compare with experimental results. As pointed out by Lekkerkerker [2], the equations border on being ill-conditioned if a numerical procedure such as collocation, with points at equal intervals, is selected for solving the equations that enforce continuity between the two shells along the intersection curve.

Hansberry and Jones [16] also developed a collocation method to describe the elastic behavior of two normally intersecting cylindrical shells with small diameter ratios that are less than 0.2. Their numerical results were compared with the experimental tests of Cranch and Dally [17].

2.1.3 Finite Element Method

In the early applications of the finite element method to intersecting cylinders, the curved shell surfaces were simply replaced by flat plate bending and membrane elements. Because of discretization errors, a large number of such flat elements was needed to converge to reasonable answers.

Prince and Rashid [18] used triangular plate elements to solve the case of very thin normally intersecting cylinders with the diameter ratio of 1:2. Their results were compared with experimental data for a nozzle-to-cylinder intersection.

Greste [19] used both two-dimensional plate bending and plane type elements to solve the tubular K joint problem.

Hellen and Money [20] demonstrated the general capabilities of the stress analysis program BERSAFE by using a double layer of isoparametric elements through the thickness of the shells.

Bakhrebah and Schnobrich [21] modeled the normally intersecting cylinder problem by using three-dimensional isoparametric elements along the intersection curve, and two-dimensional curved shell elements in the regions away from the intersection. Because the simple isoparametric elements formulated by the displacement method are inherently too stiff, incompatible modes [48] and reduced integration [47] techniques were investigated as a possible means for making the element and therefore the structure more flexible. The results calculated by Bakhrebah show good agreement with the experimental results obtained by Corum.

The techniques of nonlinear analysis have been applied to structures for many years. The application of employing the finite element method to intersecting shells, however, has only recently begun. To update the structural stiffness of the system at each step of the nonlinear analysis is a straightforward but costly and cumbersome procedure. Some literature concerning this topic has been published, with several different approaches being applied.

Mahmoud Khojasteh-Bakht and Popov [22] provided a general discussion of the use of finite elements in the analysis of elastic-plastic problems. The tangent stiffness method was employed to solve rotational shells subjected to axisymmetric loading.

Gupta, Mohraz and Schnobrich [23] used three-dimensional isoparametric elements to solve a thick circular plate with circular openings. Elastic-plastic behavior of the material was included by incorporating the Von Mises yield criterion in an incremental format. The initial stress method was used to economize the evaluation of the unbalanced nodal forces and plastic deformation at each iteration.

Larser and Popov [24] used three-dimensional isoparametric elements for the elastic-plastic analysis of thick-walled pressure vessels with sharp discontinuities in geometry. A modified incremental method, termed the "one-step iteration" or "out-of-balance force" method, was used to work out some numerical examples.

It is clear from the above reviews of the previous work that a reliable general analytical method for the nonlinear analysis of cylinder-to-cylinder intersections is not available. To fill the need for an engineering solution of the intersecting cylinders problem, the finite element method with its nonlinear feature capable of representing elastic-plastic behavior of structures is highly desirable. Before simulating and then discretizing the intersecting cylinders for finite element models, some basic knowledge of the general behavior of the structure should be known.

2.2 Important Geometric Parameters of Intersecting Cylinders

The branch pipe connection is characterized by the intersection angle of the two cylinders, reinforcements around the intersection, and three geometric ratios, i.e., the diameter ratio d/D, the main vessel thickness ratio T/D, and the membrane hoop stress ratio s/S = dT/Dt.

The "T" shape connection without any fillet reinforcing is the problem of central interest in this study. Its general behavior is discussed below based on the three geometric parameters.

The range of the diameter ratio is obviously $0 < d/D \leq 1$. From the parametric study carried out by Ellyin and Turkkan [25], it was concluded that the unreinforced nozzle-vessel attachment provided less strength when the diameter ratio was bounded between $0.5 < d/D < 0.6$. The same conclusion was also reached by Schroeder [26]. For a small d/D ratio, $d/D \leq 0.2$, the weakening caused by the cutout in the main shell is relatively small, and high strength is anticipated. This has been demonstrated with both analytical and experimental results.

The deformation pattern of the intersecting cylinders when subjected to a constant internal pressure is based on the combinations of thicknesses and radii of the branch pipe and the main shell. If the thickness ratio of the structure is relatively small, the nominal hoop stress in the cylinders is high but the distance from the intersection for which the disturbance has effectively damped out is small, and vice versa for the large thickness ratio. Therefore, in practical design, it is essential to optimize the T/D ratio if the intent is to use the material effectively. The behavior of thin shells and that of thick shells is quite different. Accordingly, the analysis approaches are not the same. For thin shells, $T/D \leq 1/20$, both the bending stresses and the stresses normal to the surface can be ignored, and only the membrane stresses due to strains in the middle surface of the shell need be considered. This is true except in the regions of disturbance such as penetrations, stiffness changes, and supports. For thick shells, the shear effect

in the thickness direction is not negligible. This means the distortion across the thickness invalidates the Kirchoff hypothesis. If the finite element method is used to analyze the structure, the selection of element models must be able to represent the real behavior of the shell. In industrial applications, a T/D ratio in the range of 1/10 - 1/50 is comparatively common.

2.3 Stress Concentration of Intersecting Cylinders

The branch pipe connection consists of two individual components, i.e., the branch pipe and the main cylinder. The contact points of these two cylindrical shells form an intersection curve [16] which, for the general case with an intersection angle α between the two axes, can be expressed as (Fig. 1)

$$X = r \cos \phi$$
$$Y = r \sin \phi - \delta \sin \alpha$$
$$Z = R\sqrt{1 - S^2 \cos^2 \phi}$$

(2.1)

with $S = r/R$ and $\delta = \dfrac{R}{\cos \alpha} (1 - \sqrt{1 - S^2 \cos^2 \phi}) - r \sin \phi \tan \alpha$

where r and R are the radii of the branch pipe and the main shell, respectively. A set of edge forces is introduced at the juncture of the two shells to enforce the continuity of displacements across the intersection line.

The standard solution of the Donell, Flugge or other form of the cylindrical shell equations for the branch pipe when subjected to edge loads can be obtained and is well known. From such solutions, it is evident that the effect of an edge disturbance on a cylindrical pressure

vessel is negligible when

$$X > 2.45 \sqrt{RT} \qquad\qquad (2.2)$$

where X is the distance measured from the forced edge. One exception deserves to be mentioned here. When the edge of the cylinder is subjected to a set of self-equilibrating axial forces and the far end is left free, the edge disturbance increases, with the distance away from the disturbed edge rather than dying out. This causes the collapse of the cylinder into an oval shape. This phenomenon was first described by Vlassov [27] in his experimental and analytical investigations. Bakhrebah also experienced this in his finite element analysis. To avoid this difficulty, the constrained boundary conditions, such as those for a diaphragm closure, are usually adopted instead of free end conditions.

The main shell is weakened by the opening which causes the discontinuity in the geometry and in the displacement fields. The existence of a stress concentration around the hole can be visualized by comparing the vessel with an infinite flat plate having a circular opening. This plane stress problem was investigated by Timoshenko [28]. It has been pointed out that the maximum stress is three times larger than the stress found in a solid plate. The stress distribution in the cylinder must also be influenced by the curvature. The stress concentration varies with the size and shape of the hole and may be three to four times as large as the stresses would be in a solid shell (Taylor [9]).

On the basis of the above data, it is logical to conclude that there is a stress concentration in the vicinity of the connection of a cylinder-to-cylinder intersection. Furthermore, experimental data [29]

have shown that there are two stress peaks along the intersection line when the structure is under internal pressure:

(1) High hoop stress in the vicinity of section AB due to the removal of material for the hole in the main cylinder (Fig. 2).

(2) High bending stress in the vicinity of point C, where the internal pressure normal to the vessel can only be balanced by the bending action and the component from the axial force in the branch pipe. For large diameter ratios, the bending stress increases while the component from the axial force decreases.

Test results show [30] that the bending stress at point C is seldom as high as the hoop stress at section AB. Thus the hoop stress in section AB governs the design at least of the intersection. To determine the stress concentration factor at section AB, an approximate analysis proposed by Lind [33], called the area method, is available for pressurized normal branch pipe connections without fillets around the junction. The area method avoids rigorous mathematic derivations. Instead, the whole concept is based on an estimate of the effective lengths (Fig. 3) of the branch pipe and main shell. The rate of decay of stress in the main shell is assumed to be a linear variation. The length over the cylinder from the maximum stress to the membrane stress is approximated as $0.8 \sqrt{RT}$. The area of the triangular stress distribution is equivalent to the maximum stress uniformly distributed over an effective length $0.4 \sqrt{RT}$. From the effective lengths of the branch pipe and the main cylinder, the corresponding effective areas G' and G (effective length x

diameter, Fig. 3) can be measured and the average stress concentration factor is computed as

$$f_a = (G/G')/(D/2T) \tag{2.3}$$

When the bending stress is taken into account, a correction factor f_b is introduced as indicated in Eq. (2.4)

$$f_b = 1 + (T/D)/\sqrt{s/S} \tag{2.4}$$

The actual stress concentration factor f_c thus is

$$f_c = f_a \cdot f_b \tag{2.5}$$

From a comparison with the experimental data, the author quotes a mean error of f_c as less than 3 percent based on his statistical evaluation of the data. Therefore, it is reasonable to presume that the high concentrated stress is distributed over a distance about $0.8 \sim 2.45 \sqrt{RT}$ from the junction. Out of this region, membrane behavior dominates. This approximation provides a preliminary estimate for modeling the structure when the finite element method is to be employed to solve the problem.

2.4 Behavior Beyond the Elastic Limit

2.4.1 Failure Mechanism of Intersecting Cylinders

The failure mechanism of intersecting cylinders is essentially based on loading conditions, material properties, and surrounding temperatures. If the structure is subjected to a monotonically increasing internal pressure, the serviceability may end as a result of severe overstressing in some regions. In other words, the stress reaches the

strength capabilities of the material in these regions. But on the other hand, if the pressure is cyclic, a shakedown failure caused by high strain fatigue may be the controlling factor [31]. When brittle materials are employed, the high stress concentration around the intersection region remains right up to the breaking point since the material has little ductility to deform and hence redistribute more uniformly the high local stresses. Therefore, points of stress concentration along the intersection curve have a greater importance and are regions of central interest if brittle fracture is a consideration. For ductile materials, a large deformation may be developed before a final plastic rupture occurs. The environmental conditions also affect structural behavior. For instance, the toughness of intersecting cylinders made from brittle materials [32] can be improved at elevated temperatures even if the structure contains notches or flaws.

Intersecting cylinders provide low serviceabilities if they undergo little deformation prior to the failure. To prevent or minimize the brittle fracture possibilities of ductile materials, it is necessary to avoid high stress fields, low temperature environments and flaws occurring simultaneously. In most of the engineering applications such as boiler or nuclear reactors, both the temperature and the internal pressure are very high. Therefore, rupture is most probably accompanied by some plastic deformations if a ductile material is used. Actually, from a survey of the failures of pressure vessels over the past decade, Nichols [34] pointed out that the most important phenomenon to be considered as a potential source of trouble was the plastic rupture of the welds, or the weld-affected areas near the branch attachments.

In this study, it is of particular interest to investigate the progression of plastification after yield starts but before the intersecting cylinders have fractured. To determine the bounds of this range, limit analysis techniques can be employed to approximate the initial yield load as well as the collapse load.

2.4.2 Limit Analysis

In limit analysis, the stress-strain relation is normally simplified to rigid-perfectly plastic, concentrating thereby the deformations in localized regions. A lower bound solution is obtained by the determination of a statically admissible system, defined as any system which satisfies the equilibrium conditions, and has stresses at every point at or below yield. An upper bound solution is found by the consideration of a kinematically admissible system. This system is defined as a compatible pattern of displacement for which the rate of external work is equal to or exceeds the rate of internal dissipation. The upper bound gives the maximum collapse load.

The limit analysis method was essentially developed for the design of steel frames. Its application to shells was first published by Drucker [35] in a study of symmetrically loaded cylindrical shells without axial forces. Because of the lack of rotational symmetry, unlike the nozzle to spherical shell connections, the limit analysis of a branch-to-cylindrical vessel is much more difficult. Attempts at limit analysis of this configuration have only been made recently. Cloud and Rodabaugh [36] gave an upper bound solution for internal pressure of a normal branch pipe connection with the restriction of a small diameter

ratio, less than 0.5. Schroeder and Ramgarajan [27] also obtained an approximate upper bound solution for diameter ratio between 0.4 to 1.0. Ellyin and Turkkan [26] have given a lower bound solution for internal pressure by using the limit pressure as the objective function and maximizing the objective function over the admissible stress field. The solutions obtained were over a wide range of parameters and were compared with experimental data.

To solve intersecting shells by limit analysis, the general geometric relations are first established. No simplifying assumptions should be made along the intersection curve if the solution is to be for the general case. Then, the partial differential equations of equilibrium of stress resultants are derived. A stress field which satisfies the equilibrium equations, all the boundary conditions and the stress continuity condition at the intersection are constructed by following the work of Hodge [37]. After the stress fields for the branch and main vessel have been chosen, a yield criterion is imposed and, according to the lower bound or upper bound theorem, a set of inequality conditions are obtained. The extreme of the solutions of these inequality conditions gives the lower or upper bound solution for the intersecting cylinders.

From a parametric study, it is found that the bound is affected by the geometric variables. A relatively small increase in the nozzle thickness considerably increases the limit pressure of the structure. This leads to the reinforcement around the junction of cylinders in practical design. However, limit analysis gives no intermediate results, only the initial yield load and the collapse load of the branch pipe connections. To fill in this gap, the finite element approach with elastic-plastic analysis is desirable.

CHAPTER 3

THE FINITE ELEMENT APPROACH

3.1 General

The finite element method can be viewed as basically a variational approach. When considered in this light, the procedures can be generalized, thereby extending the application of the finite element method to many engineering fields, not just structural. Using variational principles, the governing equations of a continuum can be obtained through the derivation of a stationary solution. For most cases, these equations are too complex to be amendable to closed form solutions directly. A usual technique is to use the Rayleigh-Ritz method to construct approximate solutions by reducing or restricting the unknowns to a small or finite number.

The energy procedures used in structural mechanics can be classified essentially as the minimum potential energy method and the minimum complementary energy method. The former, usually referred to as the stiffness or displacement method, associates with assumed displacement parameters. The latter, termed the flexibility or force method, deals with a parametric equilibrium stress field. In addition to these two methods, a mixed procedure, utilizing the Hellinger-Reissner principle [38], has been developed by taking both displacements and stresses as primary variables. However, of these methods as well as other hybrid schemes the displacement method remains the most generally used procedure in structural mechanics. It is employed in the present study.

The finite element idealization simulates a real structure as an assemblage of a finite number of elements. This introduces a discretization error. This error can involve both the geometry and the displacement field. The upper-bounded monotonic convergence is not guaranteed unless several sufficiency conditions are satisfied. The first is the completeness in energy that requires both rigid body modes and constant strain states to be included within the displacement field. The second is that the continuity of displacement must be maintained across any element interface. However, the conditions given above may be relaxed if the so-called "patch test" proposed by Irons [39] is satisfied. This test provides a necessary condition for convergence while its sufficiency is unproved. Also nothing can be said about the direction from which convergence is obtained.

3.2 Displacement Method

The matrix formulation of structural problems arose general attention in the early 1950's with a series of papers published by Argyris [40], Turner [41], and a number of other investigators. Much progress has been made since then by introducing new types of elements and more sophisticated computer techniques. Successful developments cover various forms of structural behavior such as plasticity, dynamics and large deflection problems.

There are two basic steps in the development of the displacement method. One is the element formulation and the other is the structural calculation. At the element level, the displacements, u, over the element are defined in terms of the displacements at selected points called

nodal points. These points are located within the element or on its boundary. The displacement definition is accomplished by means of interpolation functions, N:

$$u = N \, \underline{u} \qquad (3.1)$$

where $\underline{u}$ contains all the nodal displacements of the element. The strains, $\underline{\varepsilon}$, at any point in the element are obtained by taking appropriate derivatives of displacement field with respect to the selected element coordinate system. The strain-displacement relations can be expressed as

$$\underline{\varepsilon} = B \, \underline{u} \qquad (3.2)$$

where the coefficients of matrix B are functions of the nodal coordinates.

The condition of equilibrium is obtained by applying the principle of minimum potential energy

$$\delta(W_i + W_e) = 0 \qquad (3.3)$$

where W_i can be expressed as the integral of strain energy over the volume of element under deformation

$$W_i = \int_V \frac{1}{2} \, D_{ijk\ell} \, \varepsilon_{ij} \, \varepsilon_{k\ell} \, dV$$

$$= \int_V \frac{1}{2} \, \underline{u}^T \, B^T \, DB \, \underline{u} \, dV \qquad (3.4)$$

The external work done by the surface traction T_i and the body force f_i is given as

$$W_e = -\int_V f_i \, u_i \, dV - \int_S T_i \, u_i \, ds \qquad (3.5)$$

Substituting these into Eq. (3.3) and taking the first variation, the following equation is obtained

$$\delta \underline{u}^T \, K \, \underline{u} - \delta \underline{u}^T \, \underline{P} = 0 \tag{3.6}$$

where

$$K = \int_V B^T \, DB \, dV \tag{3.7}$$

$$\underline{P} = \int_V N^T \, \underline{f} \, dV + \int_S N^T \, \underline{T} \, ds \tag{3.8}$$

Since the virtual displacements $\delta \underline{u}$ are arbitrary, Eq. (3.6) can be simplified as

$$K \, \underline{u} = \underline{P} \tag{3.9}$$

K and $\underline{P}$ are the stiffness matrix and the generalized load vector of the element, respectively.

At the structural level, the total structural stiffness matrix and the structural load vector are set up following the superposition technique to assemble all the elements of structure together properly. After incorporating the boundary conditions, the nodal displacements can be solved. The strains and the stresses can therefore be evaluated wherever desired.

The structural stiffness matrix is characterized by being symmetric, banded, sparsely populated and positive semi-definite. Only the upper or the lower triangular form obtained by decomposition is considered in computation with only a half band of it being stored.

3.3 Structural Modeling

In a region with a sharp geometric discontinuity or a high stress gradient, a fine mesh is needed to achieve accuracy in results. A coarse mesh may cause the violation of local equilibrium even at

integration points. These are the points that are used as control points to predict the occurrence of the plastic actions in the structure when nonlinear analysis is being used. This drift from the true response can be kept to a minimum if the structure is modeled properly.

Hand, et al. [42] used a layered concept to investigate the progression of cracking that develops in a concrete slab or shell under external loads. The thickness of each element is divided into several layers. Each layer, in turn, may have different material properties. The nodal displacements are converted to middle surface strains and curvatures, then to layer strains by employing the Kirchoff assumption that implies normals to the middle surface remain straight and normal after deformation. From the stress calculation, the excess stresses in each layer are accumulated and converted back as unbalanced nodal forces for the next iteration. This procedure worked well for the plate and smooth shallow shells that were studied. A layered concept which allows the plasticity to propagate through the thickness as well as along the surface will be employed.

The intersecting shell is the problem of particular interest in the present study. From previous studies, it is known that the stresses in intersecting shells decay sharply to reach the membrane stress levels away from the intersection region. Therefore, a layered system need to be considered only in the vicinity of the intersection. The desirability of restricting the layering to as small an area as possible is to economize the computational effort. Because of the complicated geometrical shape of the intersection curve and the displacement variation through the thickness in this region, it is undesirable to impose the Kirchoff's assumption on

displacement field as Hand did. The three-dimensional isoparametric element family is therefore used to divide the thickness of the structure into several layers in this intersection region.

To avoid an abrupt change of stiffness in the structure away from this region, a method of grading the mesh from a fine to a coarse mesh is obtained by connecting every two layers of the previous grid to a single layer in the adjacent grid. The same procedures are repeated until only one layer represents the entire thickness. Then the shell transitional elements are used to connect to the two-dimensional curved shell elements which are used throughout the remainder of the structure. Although the modeling method is developed for interesecting shell analysis, the general nature of the procedures used is applicable to other kinds of structures as well.

3.4 Element Stiffness Matrix

3.4.1 The Isoparametric Family

Three-dimensional solid elements are capable of correctly representing the behavior of a beam, plate, or shell including any of the varied aspects of structural components because they enable bodies with curved boundaries to be treated with a limited number of elements. A general isoparametric element suggested by Irons [43] is adopted in the present study. With that formulation it is possible to add any number of intermediate nodes to the individual edges of an eight-node brick element by employing the so-called "departure concept". The displacement variables at intermediate nodes are treated as the difference or departure from the linear displacement variation

between two corner nodes.

One way of expressing the displacements at the edge of an element would be to use interpolation functions in the form of a quadratic variation on the edge AB (Fig. 4). This can be expressed as

$$U^{AB} = N_A U_A + N_B U_B + N_C U_C \qquad (3.10)$$

where

U^{AB} = quadratic response along the edge AB

U_A, U_B, U_C = nodal values at nodes A, B and C, respectively

N_A, N_B, N_C = quadratic shape functions corresponding to nodes

A, B and C, respectively

On the other hand, the displacements of the intermediate nodes U_C can be written as

$$U_C = \overline{U}_C + \frac{1}{2}(U_A + U_B) \qquad (3.11)$$

where $\overline{U}_C$ is the departure displacement of node C as shown in Fig. 4.

Substitution of Eq. (3.11) into Eq. (3.10) gives an alternate way of expressing the displacements as

$$U^{AB} = \overline{N}_A U_A + \overline{N}_B U_B + N_C \overline{U}_C \qquad (3.12)$$

where

$$\overline{N}_A = N_A + \frac{1}{2} N_C = \frac{1}{2}(1 - \xi)$$

$$\overline{N}_B = N_B + \frac{1}{2} N_C = \frac{1}{2}(1 + \xi)$$

$$N_C = (1 - \xi^2)$$

$\overline{N}_A$ and $\overline{N}_B$ are the linear shape functions of the corner nodes A and B ($\xi = \pm 1$). With or without the last term of Eq. (3.12), the variations along the edge AB become quadratic or linear. This means whenever an additional intermediate node is introduced to any edge of an 8-node element, only the last term needs to be added without changing the rest of the equation. In a manner similar to Eq. (3.12), more intermediate nodes can be incorporated to the edge AB in order to define a higher degree of response.

The isoparametric displacement field within an element is given as

$$\begin{Bmatrix} u \\ v \\ w \end{Bmatrix} = \sum N_i \begin{Bmatrix} u_i \\ v_i \\ w_i \end{Bmatrix} \tag{3.13}$$

For a general curvilinear element the geometric transformation relationship between the global cartesian coordinates and the local isoparametric coordinates is established by Eq. (3.14) as

$$\begin{Bmatrix} x \\ y \\ z \end{Bmatrix} = \sum N_i \begin{Bmatrix} x_i \\ y_i \\ z_i \end{Bmatrix} \tag{3.14}$$

The strain-displacement relation is defined by proper differentiation of the displacement field as

$$\{\varepsilon\} = \begin{Bmatrix} \varepsilon_x \\ \varepsilon_y \\ \varepsilon_z \\ \gamma_{xy} \\ \gamma_{yz} \\ \gamma_{zx} \end{Bmatrix} = \sum \begin{bmatrix} N_{i,x} & 0 & 0 \\ 0 & N_{i,y} & 0 \\ 0 & 0 & N_{i,z} \\ N_{i,y} & N_{i,x} & 0 \\ 0 & N_{i,z} & N_{i,y} \\ N_{i,z} & 0 & N_{i,x} \end{bmatrix} \begin{Bmatrix} u_i \\ v_i \\ w_i \end{Bmatrix} = [B]\{U_i\} \tag{3.15}$$

Substituting into Eq. (3.7), the element stiffness is obtained

$$[K] = \int_{vol} [B]^T [D][B] \, dV \qquad (3.16)$$

where [D] is the material property matrix defined as the stress-strain relationship of a homogeneous linearly elastic material. This matrix is given in Appendix A. The volume element dV has to be transformed to a curvilinear coordinate system for the integration process

$$dV = dx \, dy \, dz = |J| \, d\xi \, d\eta \, d\zeta \qquad (3.17)$$

where $|J|$ is the determinant of the Jacobian matrix. Equation (3.16) is now of the form

$$[K] = \int_{-1}^{1} \int_{-1}^{1} \int_{-1}^{1} [B]^T [D][B] \, |J| \, d\xi \, d\eta \, d\zeta \qquad (3.18)$$

Both [B] and [D] contain many null factors. A lot of intermediate calculations can be eliminated if the calculation of the element stiffness matrix is broken into parts and only the non-zero terms are executed. A more detailed discussion of this is present in Appendix A.

There are several points that bear mentioning here.

1. The requirements of continuity and those for the constant strain states are satisfied in the isoparametric element family, thus insuring convergence.

2. The elements, however, are far too stiff against flexure, especially the low order elements. For instance, a three-dimensional 8-node brick type isoparametric element (Fig. 5) develops the constraints on the transverse displacement mode because of the appearance of parasitic shear strain

32

energy. Therefore, softening procedures such as the use
of nonconforming modes or a reduced integration technique
are usually utilized to overcome this deficiency.

3. The Kirchoff's hypothesis, i.e., the normal to the mid-
surface remains straight and normal after deformation,
is adequate for most shell problems. Thus, the unnecessary
nodes through the thickness of an element can be eliminated
to minimize computational efforts. In addition, since the
concept of a layered system is employed, the high order
displacement variation along the shell thickness direction
can be approximated by several elements having only two
nodes through the element thickness.

3.4.2 Three-Dimensional Transitional Element

It is desired to connect both elements A and B to only a single
element in the next region (Fig. 6). Obviously, the continuity across the
element interface will be violated if a quadratic displacement variation
is allowed in element C while in elements A and B the displacement
variation on the corresponding face is only linear. Therefore, it is
reasonable to impose a linear displacement variation on the interface
between these three elements. With this, the constraint equation of the
mid-nodes can be established as

$$\{u\}_{mid} = \frac{1}{2} (\{u\}_{top} + \{u\}_{bot}) = [C] \begin{Bmatrix} u_{top} \\ u_{bot} \end{Bmatrix} \qquad (3.19)$$

where [C] is a transformation matrix and is described in Appendix A.

33

Introducing this relationship into the formulation of the [B] matrix, we get

$$[B]\begin{Bmatrix} u_{top} \\ (bot) \\ u_{mid} \\ \overline{U} \end{Bmatrix} = [B][A]\begin{Bmatrix} u_{top} \\ u_{bot} \\ \overline{U} \end{Bmatrix} = [B']\begin{Bmatrix} u_{top} \\ u_{bot} \\ \overline{U} \end{Bmatrix} \quad (3.20)$$

with

$$[A] = \begin{bmatrix} 1 & 0 & 0 \\ 0 & C & 0 \\ 0 & 0 & I \end{bmatrix} \quad (3.21)$$

In this, [I] is the unit diagonal submatrix and $\overline{U}$ is the nodal displacement vector excluding those on the interface of T3D element.

The element stiffness matrix, independent of nodes 4, 5, and 6 (Fig. 6), for elements A and B can be obtained through the substitution of [B'] for [B] in Eq. (3.18). With this transition element it is now possible to connect the layered region to any general three-dimensional element with 3 nodes on both the top and the bottom edges of the interface.

3.4.3 Ahmad's Shell Element

Ahmad's shell element [44] is extracted from a 16-node three-dimensional isoparametric element. Conversion to the shell element precludes the possible ill conditioning that occurs when the shell thickness is very small compared to the other dimensions of the element. Furthermore, it reduces the number of unknowns. In this element, the constraint of straight normals is imposed and the strain energy corresponding to normal stresses perpendicular to the middle surface is ignored.

For a typical thick shell element (Fig. 7), the geometric shape can be defined as Eq. (3.22) if there are no intermediate nodes in the element thickness direction.

$$
\begin{Bmatrix} x \\ y \\ z \end{Bmatrix} = \sum N_i \frac{(1+\zeta)}{2} \begin{Bmatrix} x_i \\ y_i \\ z_i \end{Bmatrix}_{top} + \sum N_i \frac{(1-\zeta)}{2} \begin{Bmatrix} x_i \\ y_i \\ z_i \end{Bmatrix}_{bottom} \tag{3.22}
$$

where $N_i(\xi, \eta)$ are the shape functions for a two-dimensional quadrilateral element as shown in Fig. 8. For convenience, Eq. (3.22) can also be rewritten in a form specified by a nodal vector that connects the pairs of nodes i_{top} and i_{bottom} and the midsurface coordinates

$$
\begin{Bmatrix} x \\ y \\ z \end{Bmatrix} = \sum N_i \begin{Bmatrix} x_i \\ y_i \\ z_i \end{Bmatrix}_{mid} + \sum N_i \frac{\zeta}{2} \overline{V}_{3i} \tag{3.23}
$$

with

$$
\overline{V}_{3i} = \begin{Bmatrix} x_i \\ y_i \\ z_i \end{Bmatrix}_{top} - \begin{Bmatrix} x_i \\ y_i \\ z_i \end{Bmatrix}_{bottom} \tag{3.24}
$$

Similarly, the displacement field at any point in the element can be expressed as

$$
\begin{Bmatrix} u \\ v \\ w \end{Bmatrix} = \sum N_i \begin{Bmatrix} u_i \\ v_i \\ w_i \end{Bmatrix}_{mid} + \sum N_i \frac{\zeta}{2} \begin{Bmatrix} \Delta u_i \\ \Delta v_i \\ \Delta w_i \end{Bmatrix} \tag{3.25}
$$

where Δu_i, Δv_i and Δw_i are relative displacements or displacement differences of i_{top} and i_{bottom}. Δw_i is ignored as is the corresponding strain energy in the thickness direction. Equation (3.25) can therefore be rewritten as (Fig. 9)

$$\begin{Bmatrix} u \\ v \\ w \end{Bmatrix} = \sum N_i \begin{Bmatrix} u_i \\ v_i \\ w_i \end{Bmatrix}_{mid} + \sum N_i \, \zeta \, \frac{t_i}{2} \, [\overline{V}_{1i}, \, -\overline{V}_{2i}] \begin{Bmatrix} \alpha_i \\ \beta_i \end{Bmatrix} \tag{3.26}$$

or

$$\begin{Bmatrix} u \\ v \\ w \end{Bmatrix} = \sum [N^*]_i \{\delta_i\} \tag{3.27}$$

with

$$\{\delta_i\} = \begin{Bmatrix} u_i \\ v_i \\ w_i \\ \alpha_i \\ \beta_i \end{Bmatrix}_{mid}$$

$[N^*]_i$, expressed explicitly in Appendix B. u_i, v_i and w_i are midsurface nodal displacements along the three global coordinate axes while α_i and β_i are rotations about $\overline{V}_{2i}$ and $\overline{V}_{1i}$, respectively. In this,

$$\overline{V}_{1i} = \hat{i} \times \overline{V}_{3i}$$
$$\overline{V}_{2i} = \overline{V}_{3i} \times \overline{V}_{1i} \tag{3.28}$$

where $\hat{i}$ is a unit vector along the global x axis. By this, three local Cartesian coordinate axes x', y' and z' are defined at the midsurface node i.

The strain components of interest at any point in the element are established based on its local coordinate system.

$$\{\varepsilon'\} = \begin{Bmatrix} \varepsilon'_x \\ \varepsilon'_y \\ \gamma'_{xy} \\ \gamma'_{yz} \\ \gamma'_{zx} \end{Bmatrix} = \begin{Bmatrix} u'_{,x'} \\ v'_{,y'} \\ u'_{,y'} + v'_{,x'} \\ v'_{,z'} + w'_{,y'} \\ w'_{,x'} + u'_{,z'} \end{Bmatrix} = [B'] \begin{Bmatrix} \{\delta_1\} \\ \cdot \\ \cdot \\ \{\delta_i\} \\ \cdot \\ \cdot \end{Bmatrix} \tag{3.29}$$

After the $[D']$ matrix of an anisotropic material has been constructed (Appendix B) the stiffness matrix can be found in a systematic manner following some coordinate transformations.

$$[K] = \int_{-1}^{1} \int_{-1}^{1} \int_{-1}^{1} [B']^T [D'][B'] |J| \, d\xi \, d\eta \, d\zeta \tag{3.30}$$

A more detailed description of the formulation of the $[B']$ matrix is given in Appendix B.

With the Ahmad element, there is the inherent weakness of being far too stiff against bending. This weakness stems from an excessive extraneous shear strain energy which, in turn, causes much slower convergence than desired. As pointed out by Pawsey [45], this weakness can be diminished by the use of the reduced integration method. When reduced integration is used, the stiffness matrix may become singular as zero strain energy may occur at integration points. This is for the individual elements. But when assembled into a structure, the singularity is suppressed upon joining the element to others.

3.4.4 Shell Transitional Element

In selecting the structural modeling to be used, it becomes desirable to connect together two dissimilar elements, the three-dimensional solid element and the two-dimensional curved shell element. The transition element provides this service. It converts the five shell degrees-of-freedom at the edge where it is intended to connect to a three-dimensional element back to six degrees-of-freedom, three each at the top and the bottom face of the element.

Since the departure concept is employed with the three-dimensional element, the same modification has to be applied to the transition element at each node that is intended to connect to a three-dimensional element node for which the departure is used. The other nodes remain the same as in the Ahmad shell element. After the new shape functions for these nodes have been defined, as described in Appendix B, a new shell element stiffness matrix can be generated by standard procedures as in the Ahmad element. Then, the stiffness matrix of a transition element is obtained from Eq. (3.31).

$$[K_T] = [C]^T[K_S][C] \tag{3.31}$$

where [C] is defined as

$$\{U_S\} = [C]\{u_{3D}\} \tag{3.32}$$

The nodal forces that correspond to the displacement $\{u_T\}$ in transition elements are obtained by

$$\{P_T\} = [C]^T\{P_S\} \tag{3.33}$$

The derivation of matrix [C] is also described in Appendix B.

3.5 Generalized Loads

In the finite element system, loads are prescribed only at the nodal points and in the directions corresponding to displacement components. When distributed loads are applied to the structure, the equivalent generalized nodal loads as outlined in Section 3.2 are used because of their computational efficiency. The distributed pressure load is of particular interest and is described here.

3.5.1 Three-Dimensional Element

The pressure load Q is applied to either the top or the bottom face. Let $\hat{n}$ be the unit vector normal to the surface at any point p. The equivalent nodal loads can be established on the basis of the equivalence of the work done during a virtual displacement consistent with that for the distributed load Q.

$$\delta W = \{\delta u_i\}^T \{P_i\} = \int_S \delta\{U\}^T Q \, \hat{n} \, dS$$

$$= \{\delta u_i\} \int_S [N]^T Q \, \hat{n} \, dS \qquad (3.34)$$

or

$$\{P_i\} = Q \int_S [N]^T \hat{n} \, dS$$

3.5.2 Ahmad's Element

The same procedures are followed for the shell element. The generalized load vector, at node i, of a pressure load Q on the surface $\zeta = 1$ in Ahmad element can be constructed as

$$\left\{\begin{array}{c} P_x \\ P_y \\ P_z \\ M_\alpha \\ M_\beta \end{array}\right\}_i = \int_S [N^*]_i^T \, Q \, \hat{n} \, dS \tag{3.35}$$

3.6 Reduced Integration Technique

Obtaining the stiffness matrix of an element involves an integration over the volume of the element as Eq. (3.18) indicates. For most cases, the form of these integrals is far too complex to be carried out explicitly. To circumvent this, these integrations are frequently done numerically. The quadrature rule, as the sume of a series of products of weighting coefficients times the value of the integrand evaluated at a number of points is used. Obviously, the fewer the number of points involved, the less the amount of computation required. From numerical experimentation, it has been shown that less accurate numerical integration rules can produce better displacement and stress values. This happens because of introducing compensating errors. The reduced integration technique was first employed by Doherty, et al. [46] on plane quadrilateral elements and later by Pawsey [44] on curved elements. Zienkiewicz, Taylor and Tuo [47] used a general reduction in Gaussian integration order rather than applying the reduction only on the shearing strain energy components. They demonstrate much better accuracy than in Ahmad's first work. Choi and Schnobrich [48] compared the results obtained by including nonconforming modes with those by the reduced integration technique. Dovey [49] investigated the applicability

of three-dimensional elements for general shell problems by employing reduced integration procedures.

Theoretically, when the limiting subdivision of a structure is approached, each element approaches a state of constant energy. The total energy is then obtained by summing these constant energies over all the element volumes. Therefore, to obtain a minimal degree of accuracy, the quadrature rule must be able to evaluate the element volume correctly. For three-dimensional isoparametric elements, a second order quadrature rule meets this requirement and converges rapidly. The improvement of element performance, when using a 2 by 2 integration rule, is attributed primarily to the elimination of the extraneous shear strain energy at the ordinates of the two Gaussian integration points. That makes the element far from being too stiff.

In the finite element idealization, a geometric regularity condition is imposed on the element in a practical mesh subdivision process. Even for quite irregular configurations, numerical examples show the volume error induced is very small compared with the other approximations involved. Thus, any order of quadrature rule actually yields the correct volume as the element limit is reached. This insures the convergence. A reversed argument was therefore proposed by Dovey that the convergence might be assured if a positive semidefinite stiffness matrix of appropriate rank was obtained. In other words, any reduced integration scheme considered should be able to insure convergence as long as it results in a stiffness matrix that is positive definite after the rigid body modes have been removed. No rigorous analysis was provided but rather justification was based on numerical examples.

However, a reduced integration method tends to reduce the value of stiffness of an element to below the value evaluated exactly. This softening allows the use of a coarser mesh and economizes the cost. The reduced integration technique is now widely used in research work even though the merit of the monotonic convergence property is lost. In the present study, a second order integration is utilized for all the elements.

3.7 Equation Solver

After the structural stiffness matrix has been generated, it is desirable to solve for the nodal displacements. There are several numerical schemes available for this purpose. The Gaussian elimination method is often used for large systems due to its efficiency, and it is adopted in the present study. In the method, the whole process is divided into three separate steps, i.e., the decomposition, the forward substitution, and the backward substitution.

In the decomposition, the structural stiffness matrix is split into upper and lower triangular matrices as

$$[K] = [G^L][G^U] \tag{3.36}$$

where $[G^U]$ is nearly the transpose of $[G^L]$ except for the fact that $[G^U]$ has been normalized to make all diagonal terms equal to unity. Because of a large amount of zero factors scattered inside the banded structural stiffness matrix, the efficiency can be improved by bookkeeping the first nonzero entry in each row to avoid unnecessary computer operations. Because of the symmetry of the structural stiffness matrix, only the lower triangle is developed and stored in blocks on the secondary devices

of the computer system. Each block, with the same size of nodal degree-of-freedom, is brought back to the main core in turn and broken into submatrices for execution. Inversions of the diagonal submatrices are necessary and the singularity caused by any mistake is detected.

The forward substitution computes the intermediate results $\{x\}$.

$$[G^L]\{x\} = \{P\} \tag{3.37}$$

The backward substitution gives the nodal displacement by operating

$$[G^U]\{U\} = \{x\} \tag{3.38}$$

Only the forward and the backward substitutions need to be carried out when the solutions of different load vectors are required. This feature provides the feasibility for nonlinear analysis when the iteration method is employed.

CHAPTER 4

PLASTIC ANALYSIS

4.1 General

Many engineering applications require yielding as an essential phenomenon of a structural material. Beyond the yield point, the load-displacement relation is no longer proportional.

Plastic deformation is the movement of one layer of atoms with respect to another inside the material. This slipping is often associated with the presence of shearing forces. From a series of tests with ductile materials conducted by Bridgman [50], it has been concluded that yielding does not occur under hydrostatic stress even though those stresses may be very high. For the hydrostatic state, no shear stress occurs in any direction. With this experimental observation, the mathematical models for plasticity can be considerably simplified.

Plastic deformations are irrecoverable. Also, the strain, unlike that considered in elasticity, is not uniquely determined by the final stress but depends instead on the loading path. Incremental theory [51] is thus necessary to relate strain increments to stresses. Deformation theory, which determines the total strain components in terms of the state of stress, will not be considered here.

Lack of strain recovery is caused by "locked in" residual microstresses which result in a Bauschinger effect upon unloading. For an isotropic hardening material, however, the Bauschinger effect is ignored.

4.2 Yield Criteria and Incremental Theory

For a simple member with uniaxial load, yielding is easy to determine. But for most structures, yielding may be caused by a combination of stress components σ_{ij}. On the basis of experimental work and theoretical modifications, numerous yield criteria have been proposed to describe the behavior of material after yielding has occurred.

In general, the yield criterion depends upon the state of stress at the point under consideration. Therefore, the condition that a material has been loaded to the initial yield can be expressed as

$$F(\sigma_{ij}) = K \qquad (4.1)$$

where F = the loading function, and

K = the hardening parameter which describes the strain history.

This equation represents a yield surface in six-dimensional stress space. Some materials, such as metals or crystalline rocks, yield no plastic volume change during plastification. The hydrostatic or spherical stress state, as experiments show, does not cause any plastic deformation. Hence, it is usual to substract the hydrostatic component from actual stresses and use only the remaining stress deviator in the yield function. Equation (4.1) can thus be written in a general form as

$$F(J_2, J_3) = K \qquad (4.2)$$

where J_2 and J_3 are the invariants of the stress deviators.

The Von Mises [51] and the Tresca [51] yield criteria are the most widely used for ductile material. However, there are several

drawbacks with the Tresca criterion. First of all, the principal stresses have to be known. Otherwise, the Tresca yield function becomes quite complicated compared to the Von Mises criterion. Secondly, with Tresca, the intermediate principal stress has no effect on yielding while in the Von Mises criterion all three principal stresses are taken into account. From experimental data plots, it has been found that the Von Mises criterion generally provides closer correlation. Thirdly, in order to find the maximum shear stress at one point, it is necessary to make comparisons continuously in order to find the order of principal stresses. This makes the use of the Tresca procedure less desirable. In the present study therefore, the Von Mises criterion is used to investigate the plasticity of the shell material.

For the Von Mises criterion, Eq. (4.2) can be expressed in a simple form as

$$J_2 = \frac{1}{3} \sigma_o^2 \qquad (4.3)$$

where σ_o is the initial yield stress in simple tension. A more detailed derivation of Eq. (4.3) is shown in Appendix C.

The yield surface of a Von Mises criterion in the stress space can be interpreted geometrically as a circular cylinder with its axis equally inclined to the stress axes. For an isotropic hardening material, the yield cylinder expands without changing its shape as the loading is increased. This can be expressed as in Eq. (4.4).

$$dF = \frac{\partial F}{\partial \sigma_{ij}} d\sigma_{ij} \geq 0 \qquad (4.4)$$

If dF equals zero, the equation indicates a neutral loading case.

This means the stress state is moving on the yield surface. The condition, $dF > 0$, means the controlling stress state, in other words the yield surface, is expanding.

For subsequent yield surfaces, after the initial yield has occurred, it is operationally desirable to correlate the state of stress with the history of deformation by a single curve as in the result of a simple tensile test. The effective stress and the effective plastic strain increments are thus introduced. Their definition is as expressed in Eq. (4.5) and Eq. (4.6), respectively.

$$\bar{\sigma} = \sqrt{\frac{3}{2}} \, (S_{ij} \, S_{ij})^{\frac{1}{2}} \tag{4.5}$$

$$d\bar{\varepsilon}^P = \sqrt{\frac{2}{3}} \, (d\varepsilon_{ij}^P \, d\varepsilon_{ij}^P)^{\frac{1}{2}} \tag{4.6}$$

where S_{ij} is the stress deviator tensor. Differentiating both sides of Eq. (4.5), we obtain

$$d\bar{\sigma} = \{\frac{\partial \bar{\sigma}}{\partial \sigma}\}^{\mathsf{T}} \, \{d\sigma\} \tag{4.7}$$

To obtain general stress-strain relations after yielding has started, the Prandtl-Reuss assumption [51] is employed. This theory states that plastic strain increments $\{d\varepsilon^P\}$ are proportional to the instantaneous stress deviation, i.e.,

$$\{d\varepsilon^P\} = S_{ij} \, d\lambda = \{\frac{\partial \bar{\sigma}}{\partial \sigma}\} \, d\bar{\varepsilon}^P \tag{4.8}$$

The stress increments $\{d\varepsilon\}$ are now related to the elastic strain increments $\{d\varepsilon_e\}$ through Hooke's law

$$\{d\sigma\} = [D]\{d\varepsilon_e\} = [D](\{d\varepsilon\} - \{d\varepsilon^P\}) \tag{4.9}$$

Substituting Eq. (4.8) into Eq. (4.9) and premultiplying both sides of Eq. (4.9) by $\{\frac{\partial \bar{\sigma}}{\partial \sigma}\}^T$ as Zienkiewicz [52] did, we get

$$d\bar{\sigma} = \{\frac{\partial \bar{\sigma}}{\partial \sigma}\}^T [D] (\{d\varepsilon\} - \{\frac{\partial \bar{\sigma}}{\partial \sigma}\} \, d\bar{\varepsilon}^P) \tag{4.10}$$

or

$$d\bar{\varepsilon}^P = \frac{\{\frac{\partial \bar{\sigma}}{\partial \sigma}\}^T [D]}{H + \{\frac{\partial \bar{\sigma}}{\partial \sigma}\}^T [D] \{\frac{\partial \bar{\sigma}}{\partial \sigma}\}} \{d\varepsilon\} = [W]\{d\varepsilon\} \tag{4.11}$$

where $H = \frac{d\bar{\sigma}}{d\bar{\varepsilon}^P}$ and can be obtained for a given stress-strain curve. With the substitution of Eqs. (4.8) and (4.11) into Eq. (4.9), it can be rewritten as

$$\{d\sigma\} = ([D] - [D]\{\frac{\partial \bar{\sigma}}{\partial \sigma}\}[W]) \, \{d\varepsilon\} = [D_{ep}]\{d\varepsilon\} \tag{4.12}$$

$[D_{ep}]$ varies with the state of stress and/or the deformations. Therefore, the structural stiffness corresponding to the current material properties becomes a function of the existing displacements, i.e.,

$$[K(U)]\{\Delta U\} = \{\Delta P\} \tag{4.13}$$

This means the load-displacement relations are nonlinear. When loads are applied, the calculated load-displacement relation departs from the proper curve and corrective procedures have to be employed in order to bring the solutions back to satisfying the equilibrium equations.

4.3 Solution Method

The problem defined by Eq. (4.13) can also be considered as a system of n simultaneous independent nonlinear equations of the form [53],

$$\{f_i(U)\}_{i=1,n} = 0 \tag{4.14}$$

where

$$U = \left\{ \begin{array}{c} u_1 \\ u_2 \\ \vdots \\ u_n \end{array} \right\}$$

$\{u_i\}$ are components in a n-dimensional space or nodal parameters in the finite element method. The norm of the vector in Eq. (4.14) is

$$F(U) = \| f_i(U) \|^2 = \sum_{i=1}^{n} f_i^2(U) \geq 0 \tag{4.15}$$

Equation (4.15) becomes zero only if each $f_i(U) = 0$, and this can happen only if U satisfies Eq. (4.14). Hence, the problem of finding a nonlinear solution is equivalent to the problem of searching for the minimum of Eq. (4.15). By employing a truncated Taylor's series expansion, Eq. (4.15) can be expressed as a quadratic approximation in terms of ΔU.

$$F(U) = F(U_o) + \nabla^T F(U_o) \, \Delta U + \frac{1}{2} \Delta^T \, \nabla^2 F(U_o) \, \Delta U \tag{4.16}$$

Differentiating F(U) with respect to each of the components of ΔU and equating the resulting expression to zero, we get

$$\Delta U = [\nabla^2 F(U_o)]^{-1} \, [\nabla^T F(U_o)] \tag{4.17a}$$

where $[\nabla^2 F(U_o)]^{-1}$ is the inverse of the Hessian matrix defined as the matrix of the second partial derivatives of F(U) with respect to U evaluated at U_o. The inverse of the matrix should be positive definite for all $\Delta U \neq 0$. The application of Eq. (4.17a) in the finite element

method reverts to an equation of the form

$$\Delta U = [K_c + K']^{-1} \{\Delta Q\} \qquad (4.17b)$$

where $[K']$ is the stiffness caused by nonlinearity and $\{\Delta Q\}$ are the incremental nodal forces. $[K_c]$ is the initial elastic stiffness.

The solution process indicated by Eq. (4.17) is the Newton-Raphson method (64). However, there is a serious drawback to this method. The inversion of $[K]$ at each iteration makes the procedure very inefficient for large systems. In the modified Newton-Raphson method [54], the continual requirement for carrying out the inversion is avoided by using the same stiffness throughout; i.e.,

$$\Delta U = [K_c]^{-1} \{\Delta Q\} \qquad (4.18)$$

The new U is updated

$$U_1 = U_o + \Delta U \qquad (4.19)$$

or

$$U_1 = U_o + \lambda_o \dot{N} \qquad (4.20)$$

where

$$\lambda_o = \|\Delta U_o\| , \qquad \text{and}$$

$$N = \frac{\Delta U_o}{\|\Delta U_o\|}$$

Equation (4.20) defines a straight line through U_o with a step length of λ_o and approaches the minimum of n-dimensional space in the direction of the vector N. The rate of convergence is thus

$$r = \left\| \frac{\lambda_n}{\lambda_{n-1}} \right\| < 1 \qquad (4.21)$$

The solution is obtained when $\left\| \frac{\lambda_n}{\lambda_o} \right\|$ is less than a given small number.

Obviously, a lot of numerical procedures have been developed and used to solve general nonlinear problems. Because no one method appears to be far superior to all the others, the selection of a particular technique rests on the characteristics of the problem.

For a stress concentration problem, it is presumed that the plastification starts from the regions of high stress gradients and stays in these areas up to a certain load level. Because the plastic zones are not widely spread and represent only a fraction of the whole structure, a mildly nonlinear load-displacement relation is anticipated. To solve this type of problem, a significant amount of computational effort can be saved if the same stiffness is used in the iterative method to obtain the solution corresponding to an applied increment of load. The structural stiffness is updated only on request to speed up the rate of convergence. The incremental-iterative method [55], based on a modified Newton-Raphson procedure is thus adopted in this study. This method is usually presented in an intuitive, graphic concept as shown in Fig. 10.

To avoid the accumulation of round-off errors, the residual nodal forces from the previous load step are added to the next load increment.

4.4 Outline of Numerical Procedures

Since the regions with highly concentrated stresses are modeled with layered 3-D isoparametric elements, it seems wasteful to examine the state of plastification of all the other types of elements if those elements are known to remain elastic. Therefore, the plastic analysis is concentrated only on 3-D elements.

The following steps are carried out for each applied load increment.

(1) Find the incremental nodal displacements corresponding to the applied load increment by solving

$$[K]\{\Delta U\}_n = \{\Delta P\}_n$$

(2) Convert the incremental displacements to strain increments $\{\Delta\epsilon\}_n$ and then use the elastic material properties to calculate a temporary stress increment, $\{\Delta\sigma'\}_n$, at each integration point of the 3-D elements.

(3) Add $\{\Delta\sigma'\}_n$ to $\{\sigma\}_{n-1}$ and compute the temporary effective stress $\overline{\sigma}'_n$.

Three different situations may occur at this stage

(4A) If $\overline{\sigma}'_n < \sigma_o$, yielding has not yet happened and the temporary stresses are the actual stresses. Go to step 10.

(4B) If $\overline{\sigma}_{n-1} \geq \sigma_o$, yielding is already occurring, thus the plastic deformation that results from the load increment has to be evaluated. Find [W] as defined in Eq. (4.11) and go to step 5.

(4C) If $\overline{\sigma}_{n-1} < \sigma_o$ but $\overline{\sigma}'_n > \sigma_o$ (see Fig. 11) Yielding begins during the increment when the stress vector tries to penetrate the yield surface. The initial yield is now exceeded. Therefore, find the intermediate stress value by multiplying [W] by a linear interpolation factor β [56] which is defined as

$$\beta = 1 - \alpha = 1 - \frac{\sigma_o - \bar{\sigma}_{n-1}}{\sigma'_n - \bar{\sigma}_{n-1}}$$

Then, proceed to step 5.

(5) Evaluate the effective plastic strain increment $\Delta\bar{\varepsilon}_n^P$ and the plastic strain increment of each component $\{\Delta\varepsilon^P\}_n$ by employing Eq. (4.11) and Eq. (4.8), respectively.

(6) Find the actual stress increment $\{\Delta\sigma\}_n$ by substituting $\{\Delta\varepsilon^P\}_n$ into Eq. (4.9), then add to the previous state of stress.

$$\{\sigma\}_n = \{\sigma\}_{n-1} + \{\Delta\sigma\}_n$$

(7) Compute the effective stress increment $\Delta\bar{\sigma}_n$, then update the accumulated effective stress.

$$\bar{\sigma}_n = \bar{\sigma}_{n-1} + \Delta\bar{\sigma}_n$$

(8) Evaluate the unbalanced nodal forces.

(9) Update $[D_{ep}]$ and use it to generate the new element stiffness if a new structural stiffness matrix is required.

(10) Repeat steps 2 to 9 until all 3-D elements have been examined.

(11) If convergence is attained, add the residual nodal forces to the next load increment. Otherwise, use the current force unbalance of step 8 for another iteration starting from step 1.

4.5 Updating Structural Stiffness Matrix

When a slow rate of convergence indicates the necessity of updating the structural stiffness, usually new element stiffness matrices corresponding to the current material properties are generated for all elements, then reassembled. For a stress concentration problem, it is presumed that those elements away from the regions of rapid variations in displacements are still in their elastic range even up to the load causing severe distress in the intersection region of the structure. Thus, it is more efficient to use the difference between the old and the present element stiffness matrices when creating the new system rather than reevaluating and reassembling all the element matrices.

For elements that have yielded, the constitutive law gives

$$\{\Delta\sigma\} = [D_{ep}]\{\Delta\varepsilon\} \tag{4.22}$$

Therefore, the new element stiffness matrix is

$$[K] = \int_{vol} [B]^T [D_{ep}][B] \, dV \tag{4.23}$$

Equation (4.23) is evaluated at integration points. For those points that have no plastic deformation, the $[D_{ep}]$ is replaced by elastic material property matrix $[D]$ as described in Chapter 3.

The difference or change in the element stiffness matrix is calculated as

$$[\Delta K] = [K]_{new} - [K]_{old} \tag{4.24}$$

The positions of $[\Delta K]$ in the total structural stiffness matrix is determined so that $[\Delta K]$ can be added to the old structural stiffness matrix in accordance with their contributions to the nodes of the

structure. To save storage space, only the lower half of the 3-D element matrix is stored in the system.

4.6 Evaluation of Excess Nodal Forces [57]

An iterative approach is commonly employed when solving nonlinear problems. When the state of equilibrium is not achieved, residual stresses exist and have to be converted to unbalanced nodal forces. To do this, the residual stresses at any point are first evaluated as (Fig. 12)

$$\{\Delta\sigma_{ex}\} = \{\Delta\sigma\}_B - \{\Delta\sigma\}_C \tag{4.25}$$

where $\{\Delta\sigma\}_B$ is calculated temporary stress,

$\{\Delta\sigma\}_C$ is actual stress including nonlinearity

The residual nodal forces are determined by converting the excess nodal stresses to a system loads at the nodes which does the same work as the excess stresses would do during a virtual displacement

$$\{\Delta R_C\} = \sum \int_{vol} [B]^T \{\Delta\sigma_{ex}\} \, dV \tag{4.26}$$

Substituting Eq. (4.25) into Eq. 4.26, we get

$$\{\Delta R_C\} = \sum \int_{vol} [B]^T \{\Delta\sigma\}_B \, dV - \sum \int_{vol} [B]^T \{\Delta\sigma\}_C \, dV \tag{4.27}$$

The substitution of Eq.(4.8) into Eq. (4.27) yields

$$\{\Delta R_C\} = \sum \int_{vol} [B]^T \{\Delta\sigma\}_B \, dV - \sum \int_{vol} \int_A^B [B]^T [D](\{d\epsilon\} - \{d\epsilon^P\} \, dV \tag{4.28}$$

If the initial stiffness is used, the applied load increment $\{\Delta P\}$ can be

expressed as

$$\{\Delta P\} = \sum \int_{vol} [B]^T \{\Delta\sigma\}_B \ dV = \sum \int_{vol} \int_A^B [B]^T [D] \{d\epsilon\} \ dV \qquad (4.29)$$

Therefore

$$\{\Delta R_c\} = \sum \int_{vol} \int_A^B [B]^T [D] \{d\epsilon^P\} \ dV \qquad (4.30)$$

From Eq. (4.30), it is seen that only those elements which have yielded produce excess nodal forces and need to be included when integrating to find the residual forces. This saves a lot of computer operations when solving stress concentration problems in which the plastified area is small compared with the whole structure.

If the structural stiffness matrix is updated (Fig. 13) at point E, $[D]$ in Eq. (4.29) is replaced by a new material property $[D_{ep}]$ and yields

$$\{\Delta P\} = \sum \int_{vol} \int_A^B [B]^T [D_{ep}] \{d\epsilon\} \ dV \qquad (4.31)$$

where

$$[D_{ep}] = [D] - [D_p] \qquad \text{with } [D_p] = [D]\{\frac{\partial\bar{\sigma}}{\partial\sigma}\} \ [W]$$

or

$$[D] = [D_{ep}] + [D_p] \qquad (4.32)$$

Substituting Eq. (4.32) into (4.28), we get

$$\{\Delta R_c\} = \{\Delta P\} - \sum \int_{vol} \int_A^B [B]^T [D_{ep}] \{d\epsilon\} \ dV - \sum \int_{vol} \int_A^B [B]^T [D_p] \{d\epsilon\} \ dV$$

$$+ \sum \int_{vol} \int_A^B [B]^T [D] \{d\epsilon^P\} \ dV \qquad (4.33)$$

or

$$\{\Delta R_c\} = \sum \int_{vol} \int_A^B [B]^T [D] \{d\varepsilon^P\} \ dV - \sum \int_{vol} \int_A^B [B]^T [D_p] \{d\varepsilon\} \ dV \qquad (4.34)$$

The first term in Eq. (4.34) is exactly the same as Eq. (4.30). $[D_p]$, in the second term, is zero if the material at the integration point is still in the elastic range when the structural stiffness is updated. Thus, again, only the plastified elements need to be operated upon. Obviously, $[D_p]$ varies from point to point. To save storage, only $\{\frac{\partial \bar{\sigma}}{\partial \sigma}\}$ is kept in the file used to generate $[D_p]$.

CHAPTER 5

ELASTIC-PLASTIC SOLUTION OF NORMALLY
INTERSECTING CYLINDERS

5.1 General

The objective of the present study is to develop a finite
element method to solve intersecting cylinder problems including in that
solution any elastic-plastic behavior that might develop. Before the
selected problem was investigated several numerical examples were solved
to demonstrate the reliability and the effectiveness of the computational
procedures. Two aspects of the solution process had to be evaluated.

(1) Elastic solution

The applicability of reduced integration techniques to
shell structures was first tested. The behavior of the
elements and the adequacy of the proposed discretization
models were observed. The improvement of the accuracy
and the efficiency of the procedures suggested the use
of double precision and the secondary storage devices in
the computer work. Before a nonlinear solution was sought
an elastic solution was first run. The regions of stress
concentration are first detected from these elastic
results. Layered, three-dimensional elements in a finer
mesh are then applied to the areas with high stress
gradients.

(2) Elastic-plastic solutions

The incremental loadings are applied to the structure
to evaluate the corresponding yielding zones. From the

results, the progression of yield zones is seen. With the availability of the restart feature in the computer program, the structure is loaded step by step until failure.

Finally, a cylinder-to-cylinder shell intersection was modeled, subjected to internal pressure, and solved by the computer program. The elastic solution is compared with experimental data and Bakhrebah's finite element results. The plastic solution is then presented and discussed.

5.2 Elastic Solutions

5.2.1 Hyperbolic Paraboloid Shell

The applicability of the reduced integration technique to a general shell element is demonstrated by solving a hyperbolic paraboloid shell with clamped edges. This structure is subjected to a uniform normal load. The geometrical shape of the midsurface of the shell is described by

$$z = (f/ab) \, xy$$

where f is the rise, and a and b are the shell spans as defined in Fig. 14.

The shell is antisymmetric about the X and the Y axes. Therefore, only one quarter need to be considered. A 4 x 4 grid was used with four different combinations of mesh types and orders of integration rules.

(1) Regular mesh with 3 x 3 integration points

(2) Regular mesh with 2 x 2 integration points

      (3)   Irregular mesh with 3 x 3 integration points

      (4)   Irregular mesh with 2 x 2 integration points

The vertical displacement, W, across midspan (Y = 0), and the stress resultants N_{xy}, M_y at integration points near the X axis, are shown in Figs. 15, 16, and 17, respectively. From a comparison with the results obtained by Pecknold and Schnobrich [58], Choi and Schnobrich [48], and others, several points bear mentioning:

      (1)   All four of the cases investigated converged to give near identical solutions for W and N_{xy}.

      (2)   The deviations of M_y for the four cases considered get larger near the clamped edge. Actually, M_y in both third order integration schemes "oscillated" about the results obtained by other researchers while the second *order integration procedures* gave smooth solutions.

      (3)   The third order integration rule provided slightly higher results in the regions close to the center line but smaller values near the clamped edge in comparison with the results obtained from second order integration. For the second integration rule, a nonmonotonic convergence is anticipated.

For the problem studied it was found that the second order integration scheme produced better results than did the higher order integration. This was true not only for displacements but more importantly for stress resultants. This is very important in plastic analysis when the integration points are used as the control points to predict the onset of plasticity in the elements.

5.2.2 Pinched Cylinder

The effectiveness of Ahmad's element when used with a reduced integration scheme is further observed in the solution to a pinched cylinder problem. This problem has a stress concentration due to the application of point forces. A solution to the pinched cylinder has been published by Timoshenko. This problem has become a base against which many researchers have compared their solutions. The pinched cylinder with various thickness to diameter ratios has been investigated by Cantin [59] using an element of 24 degrees-of-freedom. Ashwell and Sabir [60] also solved the problem by employing the rectangular cylindrical shell element with 20 degrees-of-freedom. The dimensions of the example used in this study (Fig. 18) were taken from the report by Lindberg, et al. [61]. This shell was also investigated by Razzaque [62]. The exact solution shown for comparison was obtained by Lindberg using numerical integration of Timoshenko's equations.

Because of symmetry, only one octant was analyzed and that with 4 x 2 grids, 4 elements in the hoop direction and 2 elements in the longitudinal direction. The two ends of the cylinder are supported by a diaphragm, i.e., u = w = 0. Equal and opposite concentrate loads are applied on opposite ends of the diameter at the center points of the cylinder.

In comparison with the results provided by other researchers, it is seen (Figs. 19-22) that adequate agreement, in many cases superior to some of the other reported results, was obtained by using a relatively small number of elements. The effectiveness of the element and the

efficiency of the reduced integration technique make nonlinear analysis
of stress concentration problems, such as the intersecting cylinder
case feasible.

5.3 Elastic-plastic Solutions

5.3.1 Simply Supported Beam and Cantilevered Beam

As a demonstration of the adequacy of the proposed finite
element models in plastic analysis, two elementary but representative
sample structures were solved. A simply supported beam and a cantilevered
beam have been tested with the same structural modeling, but different
boundary conditions. The structures are subjected to increasing uniform
loads. An elastic-ideally plastic material behavior is assumed in both
cases.

A two-layered system with 3-D quadrilateral elements was first
employed in the region of high bending stresses, i.e., the fixed end of
the propped cantilevered beam and the midspan of the simple beam.
Transitional elements and shell elements were used in the remaining
portions of the structures. A second order integration rule was used
for all elements. The results are compared with the theoretical solutions
provided by Prager and Hodge [63] in Figs. 23a and 24a. In these figures,
W_o is the center or the tip deflection. W_o^* is the center or the tip
deflection at the maximum load for which the structure remains entirely
elastic, and ρ represents the nondimensional load parameter, given by

$$\rho = \frac{P}{P_o} \left(\frac{L}{t}\right)^2$$

where P is applied load and $P_o = 4b\sigma_{yield}$.   L and t are defined as

shown in Figs. 23 and 24. The progression of the elastic-plastic boundary, through the cross section, is quite shallow in both cases. A refined mesh with four layers in the region of high bending stress was then adopted. The results are also shown in Figs. 23a and 24a. It was found that good agreement with Hodge's work was achieved. The progression of the plastic zones for the two beams are shown in Fig. 23b and Fig. 24b, respectively. The flat or shallow elastic-plastic boundary propagation does not exist for most of the intersecting structures of interest in the present study. This fact is taken into account when the modeling is selected for the intersecting cylinders.

5.3.2 The Thick-walled Pressure Vessel

To explore the general elastic-plastic behavior of cylinders under increasing internal pressure, an infinitely long thick hollow cylinder with internal and external radii of 1^{unit} and 2^{unit}, respectively, has been analyzed. This problem was originally investigated by Hodge [64] using a finite difference solution with the case of elastic-plastic materials. Later, both Gupta (23) and Salem (55) used finite element methods to obtain comparison solutions.

A quarter of a unit-length of the pressure vessel was meshed by 8 three-dimensional quadrilateral elements placed in four layers through the thickness. Symmetric boundary conditions were applied to all the faces except the internal and the external surfaces of the cylinder. Second order reduced integration was again used to predict the nonlinearity of material and to evaluate stresses. The results

again showed a very good agreement with those obtained by the other researchers (Figs. 25, 26 and 27).

In comparison with the elastic solution at p = 12.5 psi, it is concluded that stress relief occurs in the hoop stress and in the axial stress, while the normal stress, σ_r, is almost unaffected by the progression of the yield zone. This phenomenon was also indicated by Prager [63]. If the pressurized vessel is unloaded elastically after the cylinder has been stressed into the plastic range, the elastic hoop stress subtracts from the actual plastic hoop stress to give a compressive residual stress at the inside wall. This compressive stress is found very useful in alleviating high stress concentration and in industrial applications of increasing the fatigue life of highly pressurized pipe components. From the results at other loading levels, it is found that the plastic zone expands in accordance with the peak of the hoop stress and penetrates through the cylindrical wall as the load is increased. When the structure is pressurized to 12.5 psi, the plasticity propagates to a radius of 1.4 times the internal radius as shown in Fig. 26b.

5.4 Normally Intersecting Cylinders

5.4.1 Introduction

The set of intersecting cylinders used in the experiments conducted at Oak Ridge National Laboratory by Corum [7] was selected as the best problem to be analyzed here because of the availability of the test data. The problem has also been investigated by Prince and Rashid [18] and by Bakhrebah and Schnobrich, each in the elastic range.

The geometric parameters and the material properties of the problem are

Nozzle-to-cylinder diameter ratio, d/D = 0.5

Cylinder thickness-diameter ratio, T/D = 100

Nozzle thickness-diameter ratio, t/d = 100

Nominal hoop stress ratio, s/S = 1

Outside radius of the cylinder, R = 5 in.

Cylinder thickness, T = 0.1 in.

Modulus of elasticity, E = 30,000,000 psi

Poisson's ratio, ν = 0.3

Because a mild steel material is being simulated, the initial yield stress is assumed to be 34 ksi and a very shallow hardening modulus, EH = 700 ksi is used. The geometrical shape of the intersection curve can be defined through Eq. (2.1) by setting $\alpha = 0°$ to get

$$x = r \cos \phi$$
$$y = r \sin \phi$$
$$z = \sqrt{R^2 - r^2 \cos^2 \phi}$$

Substitution of the internal or external radii of the nozzle and the cylinder into the above equations produces the internal or external intersection curve. The connection of the outer and the inner intersection curves determines the intersection surface between the nozzle and the cylinder.

The structure is subjected to increasing internal pressure. From the results of a limit analysis, the lower bound [25] and upper bound [26] solutions for the pressure loads to initiate yielding and

to produce a mechanism are about 0.1 ksi and 0.37 ksi, respectively. It must be noted that the upper bound 0.37 ksi is for perfect-plastic materials without considering the possibility of a local failure even though a very large plastic strain may have occurred at some point before the computed failure of the structure. In practical applications, this load level may be unattainable because the large deformations may cause the structure to fail physically before the bound is reached. Besides, the load-displacement curve becomes quite shallow when the applied load approaches this limit. This creates numerical problems with displacement results of poor accuracy in the nonlinear analysis. Therefore, the plastic deformation or the effective plastic strain at some critical point is used as token to control the increase of the internal pressure in this study. The internal pressure loads acting on the end caps of the vessel and the nozzle are converted to axial forces and applied to the walls of vessels.

5.4.2 Discretization Model of the Intersecting Cylinders

The structure is symmetric about the XZ and the YZ planes (Fig. 28). Thus only one-quarter of the structure need be considered. According to the parametric study in Chapter 2, it is presumed that the stress concentration occurs within the range of $2.45\sqrt{RT}$ from the junction. The nozzle and the cylinder are thus modeled with layered 3-D elements within that distance from the intersection. To represent the geometry of the curved intersection surface, quadrilateral isoparametric elements, without midside nodes in the thickness direction, are employed. The size of elements is increased with the distance away

from the junction. The thickness of the vessels is divided into two layers as a result of consideration of the following:

(1) The thicknesses of the vessels are very thin compared with the diameters. Thus, to keep the depth of the 3-D elements in a proper proportion with the other two dimensions, a close grid refinement through the thickness of the cylinder is not desirable.

(2) The half bandwidth of the total structural stiffness matrix increases greatly with the number of layers. The computer time is proportional to the total degrees of freedom and the square of the bandwidth.

On the boundary of this region, 3-D transitional elements are used to connect the layered elements with a single element. Shell transitional elements are then used to bridge between the 3-D element and the shell elements which are used throughout the remainder of the structure to reproduce the membrane behavior of the shell structures.

End caps are used at the ends of the pipes, and the boundary conditions of the structure are:

At the end cap or diaphragm of the cylinder, $X = Z = \beta = 0$

At the end cap or diaphragm of the nozzle, $X = Y = \beta = 0$

On the symmetry plane YZ, $X = \beta = 0$

On the symmetry plane XZ, $Y = \alpha = 0$

The mesh employed in this analysis (Fig. 28) contains 507 nodes and 110 elements. The structure has about 2000 degrees-of-freedom while the half bandwidth spans about 180 degrees-of-freedom. The input data

was generated by a computer program. The intersecting curve function was used to generate the coordinates of the 3-D elements.

The structure was loaded in a step-by-step manner. At the end of each load step, the generated data was stored on a tape for restart at a later time. The structural stiffness matrix was updated and resolved twice during the entire solution process. Each element took about 11 seconds of IBM 360/75 computer time to generate. In the nonlinear range, each iteration took about 1 minute. The structure was loaded by eight loading increments.

The reduced integration technique was also employed during the whole process. The second order integration rule was used for all the elements to evaluate their stiffness, the stresses and to predict the nonlinearity of the structure.

5.4.3   Elastic Solution

The elastic solution was obtained at the 50 psi level of internal pressure load. The results are presented and compared with the experimental values and with the finite element solutions provided by Bakhrebah. These comparisons are shown in Figs. 29 through 40. Good agreement is observed in general even though minor deviations appeared in the axial stress of the nozzle near the 0° line and the 270° line (Fig. 28). The axial stresses of the inside surface in this study converges to the limiting value for that face, that is, to the internal pressure. This is expected in a proper analysis because of the satisfaction of the equilibrium condition with the given internal pressure on the inner surface.

From the elastic solution, several observations can be made:

(1) The maximum stresses occur at the junction between the nozzle and the cylinder. The high stresses dissipate over a range less than $1.5\sqrt{RT}$ from intersection, that means about 1 in. in the cylinder and 0.5 in. in the nozzle for this problem. This suggests the approximation $2.45\sqrt{RT}$ is on the conservative side. Away from this region, both the hoop stress and the axial stress approach the membrane solution values and stay at a constant relation with internal pressure P as

$$\sigma_\theta = \frac{PR}{T} = 2.5 \text{ ksi}$$

$$\sigma_y = \frac{PR}{2T} = 1.25 \text{ ksi}$$

(2) The hoop stresses in the nozzle and the cylinder near the $0°$ line are in tension across the thickness while the axial stresses occur as tension on the outside fiber and compression on the inside fiber, the result of bending moments. This makes the inner walls highly distorted and provides the great potential for yielding to initiate here when the internal pressure is increased.

(3) The hoop stress on the cylinder near the $270°$ line results in hoop bending to balance the moment produced by the internal pressure. Since the hoop stress in this region is relatively small and has the same sign as the longitudinal stress both on the inner and outer fiber, the material is thus less deformed and then highly resists the occurrence.

of plastification.

5.4.4 Plastic Solution

The initial yield load obtained from this study is about 0.11 ksi. This value compares closely with the result of 0.102 ksi from the limit analysis of Ellyin [25]. The load-displacement relations for points A, B and C are presented in Fig. 41. The stress distributions on the 0° line of the structure at load level P = 0.18 ksi are presented in Figs. 42 through 49. The plastic stress distributions are compared with stress values that an elastic analysis would compute at the same load level. This helps in understanding the stress development as the structure yields and visualizing the residual stresses that develop upon unloading.

Figures 51 through 54 show the progression of the plastified regions in the structure at the sections containing the integration points. The plastic action occurs as the internal pressure load increases from 0.1 ksi to 0.2 ksi. The boundaries of the plastified regions were drawn by enveloping the plastified integration points in the elements at the various different load levels. The progression of the yield zones along the inner and the outer surfaces of the structure in the vicinity of the intersection area are shown in Figs. 55 and 56, respectively.

From the numerical results obtained, some conclusions have been reached:

>   (1) Stress relief occurs in the hoop stress in the plastified regions while the axial stresses are almost unaffected by the progression of plastic action. The stresses converge to the membrane solution and have a constant distribution

across the thickness of the vessels when the distance
away from the intersection increases.

(2) The initial yield occurs at the inside surface of the
nozzle, where the two cylindrical walls intersect
perpendicularly. This implies that the bending action
resulting from the discontinuity of this region requires
special consideration in the structural design.

(3) In the regions around the intersection, the figures show
that at each section the plastification always starts
from the inside layers, then gradually penetrates the
walls of the cylinders from the inside spreading out to
the outside.

(4) As the internal pressure is increased, the plastified
regions progress along the intersection curve and spread
out following the distribution of high stresses.

(5) The elastic-plastic boundaries in the regions of the
junction are parallel to the longitudinal direction and
layered through the thickness, while away from these
regions the boundaries enveloping the plastified
integration points become steep. This implies then
that membrane axial and hoop stresses control the further
progression of plastic action. Outside the immediate
vicinity of the intersection the normal stress, σ_r, is
relatively small because of the small thickness-to-
diameter ratio. Thus the normal stress does not play
a significant role.

The largest deformation, about 0.01 in., occurred at point C
in the X direction while the axial displacement of the main vessel (point B)
is comparatively small and almost unaffected by the plastification of the
intersection. The effective plastic strain at the inner surface point
which first goes plastic increases about 3 times larger than initial yield
strain when the pressure load is 0.2 ksi. Since the remaining portions out
of the intersection are still in the elastic range, an increase in the
thickness, or a fillet reinforcement around the junction, may be adequate
to prevent the development of large plastic strains.

CHAPTER 6

CONCLUSIONS AND RECOMMENDATIONS

6.1 Conclusions

A nonlinear finite element method has been presented for analyzing intersecting cylinders. From the sample problems investigated with various element models in this study, it is found that good results are achievable through the use of the reduced integration technique. When performing the plastic analysis, the reduced integration points serve as the control points to predict the nonlinearity of the material behavior. Definition of the progression of plastic action through the region in the vicinity of the intersection is obtainable with the incorporation of layered three-dimensional elements. Such elements are used in the regions of high stress gradients while transitional elements and two-dimensional curved shell elements are used in the remaining regions to economize the computational efforts.

The adequacy of the discretized model of the intersecting cylinders is confirmed by comparing the elastic solution of a normal cylinder-to-cylinder intersection with experimental data. From the nonlinear solution of this structure it is found that yield gradually penetrates the walls of the cylinders from the inside face to the outside face. This plastification starts from the region where the two cylindrical walls intersect perpendicularly, then spreads out along the intersection line when the load is increased. Around the intersection line, bending is the major cause of yielding while away from this region membrane stresses govern the progression of yielding.

Although the selected intersecting cylinders fall in the category of thin shell structures, the procedures can be applied to general cases with different loading patterns.

6.2 Recommendations for Further Studies

6.2.1 Intersecting Cylinders

From the numerical results of the normally intersecting cylinders solved in this study, it is observed that the plastified region is limited to a small area around the intersection up to when another failure mechanism forms in the structure. To prevent the occurrence of large plastic strains in this area or to keep the structure in a low stress field, the use of reinforcement or a fillet at the junction is of particular interest in practical design. The discretization method used in this study can be utilized to investigate the effect of reinforcement and the amount it increases the strength of the structure. Research can also be expanded to include the external load and the moment caused by axial loads at the end of the branch pipe.

The "K" joint is another type of connection which may occur in networks of pipes or offshore oil-drilling towers, etc. The complicated geometrical shape of intersection curve needs special considerations in modeling the structure. The work done by Greste [18] may give some general ideas for the start.

6.2.2 Fatigue Failure of Shell Intersections

Intersecting cylinders may be subjected to different loading patterns in realistic engineering applications. For instance, when the

cylinder-to-cylinder intersection is designed to operate in an oceanic environment the loading may be cyclic. To account for fatigue behavior of the structure becomes important in this case. Since elastic unloading is conducted, the Bauschinger effect, or kinematic hardening, of the materials needs to be considered. Simplification of the material properties such as linear strain hardening may not be capable of representing the realistic situation after several loading cycles. A more specific description of the material properties may be necessary. The work done in Ref. 65 may be helpful in understanding the general behavior in this field.

6.2.3 Fracture Mechanics of Shell Structures

When flaws or notches exist in the structure under certain unexpected conditions, fracture of the material may occur suddenly causing the leaking or the complete failure of the structure. Especially when the intersecting cylinders, with their high stress fields around the intersection, are operated in an environment with a temperature lower than NDT of the material, brittle fracture may occur without any warning and cause extensive damage. To prevent this from occurring it is necessary to investigate the fracture mechanism of the intersecting cylinders and the progression of cracking. A lot of attention has been given to this field. But, the application of the finite element method to fracture mechanics is still mainly in its early development with applications in two-dimensional plate problems. Very little has been publised on the application of fracture criteria to shell structures. There are two major difficulties:

1. The lack of adequate finite element models to represent

the fracture behavior of shell structures.

2. A very fine mesh around the tip of the flaw is inevitable because of the high stress concentrations that occur in that region.

However, the layered system used in this study to model the structure from a fine to a coarse mesh around the tip can be utilized to cut down the computational expense.

LIST OF REFERENCES

1. "ASME Boiler and Pressure Vessel Code, Section III, Nuclear Vessels," The American Society of Mechanical Engineers, New York, 1968.

2. Lekkerkerker, J. G., "The Determination of Elastic Stresses near Cylinder-to-Cylinder Intersection," Nuclear Engineering and Design 20 (1972), 57-84.

3. Corum, J. M., Bolt, S. E., Greenstreet, W. L. and Gwaltney, R. C., "Experimental and Finite Element Stress Analysis of a Thin-Shell Cylinder-to-Cylinder Model," ASME Publication 71-PVP-36.

4. Zienkiewicz, O. C., "The Finite Element Method in Engineering Science," McGraw-Hill, London, 1971.

5. Mehringer, F. J. and Cooper, W. E., "Experimental Determination of Stresses in the Vicinity of Pipe Appendages to a Cylindrical Shell," Proc. Soc. Exper. Stress Analysis, Vol. 14, No. 2, 1957.

6. Cranch, E. T., "An Experimental Investigation of Stresses in the Neighborhood of Attachment to a Cylindrical Shell," Welding Research Council Bulletin Series, No. 60, 1960.

7. Gwaltney, R. C., Corum, J. M., Bolt, S. E. and Bryson, J. W., "Experimental Stress Analysis of Cylinder-to-Cylinder Shell Models and Comparisons with Theoretical Predictions," ASME Publication 76-PVP-10.

8. Schneider, R. W., Jackson, W. M. and Nicolls, W. R., "Photoelastic Study and Fatigue Tests of a Contoured, Integrally Reinforced Branch Connection," ASME Publication 71-PVP-5.

9. Taylor, C. E., Lind, N. C. and Schweiker, J. W., "A Three-Dimensional Photoelastic Study of Stresses around Reinforced Outlets in Pressure Vessels," T. & A. M. Report No. 137, Univ. of Illinois at Urbana-Champaign, 1958.

10. Taniguchi, K., Kono, K., Iki, T. and Setoguchi, K., "A Study of Local Stresses around Nozzles of Pressure Vessel under External Loading," Proc. 1st Int. Conf. on Pressure Vessel Technology, Delft and The Hague, 1969.

11. Flugge, W., "Stresses in Shells," 2nd Printing, Springer-Verlag, Berlin, 1962.

12. Reidelback, W., "The State of Stress at the Perpendicular Intersection of Two Right Circular Cylinders," Translated by M. M. Stanisic, General Technology Corporation Technical Note No. 3-1, 1962. Original paper appeared in Ingenieur-Archiv 30, No. 5, 1961.

13. Eringen, A. C. and Suhubi, E. S., "Stress Distribution of Two Normally Intersecting Cylindrical Shells," Nuclear Structural Engineering (Nuclear Engineering and Design), Vol. 2 (1965), No. 2.

14. Bylaard, P. P., Dohrmann, R. J. and Wang, I. C., "Stresses in Junction of Nozzle to Cylindrical Pressure Vessel for Equal Diameter of Vessel and Nozzle," Nuclear Engineering and Design, Vol. 5 (1967), pp. 349-365.

15. Pan, K. C. and Beckett, R. E., "Stress and Displacement Analysis of a Shell Intersection," Journal of Engineering for Industry (1970), pp. 303-308.

16. Hansberry, J. W. and Jones, N., "Elastic Stresses due to Axial Loads on a Nozzle Which Intersects a Cylindrical Shell," 2nd Int. Conf. on Pressure Vessel Technology, San Antonio, Texas, 1973.

17. Cranch, E. T. and Dally, J. W., "An Experimental Study of Attachments to Cylindrical and Shallow Spherical Shells," Symp. Nuclear Reactor Containment Buildings and Pressure Vessels, Royal College of Science and Technology, Glasgow, 1960, published by Butterworths, London, pp. 221-256.

18. Prince, N. and Rashid, Y. R., "Structural Analysis of Shell Intersections," Proc. 1st Conf. on Pressure Vessel Technology, Delft and the Netherlands, Sept. 29-Oct. 2, 1969.

19. Greste, O., "Finite Element Analysis of Tubular K Joint," Report No. NCSESM 70-11, University of California, Berkeley, June 1970.

20. Hellen, I. K. and Money, H. A., "The Application of Three-Dimensional Finite Elements to a Cylinder-Cylinder Intersection," Int. J. for Numerical Meth. in Eng., Vol. 2 (1970), pp. 415-418.

21. Bakhrebah, S. A. and Schnobrich, W. C., "Finite Element Analysis of Intersecting Cylinders," Civil Engineering Studies, SRS No. 400, University of Illinois at Urbana-Champaign, 1973.

22. Mahmoud Khojasteh-Bakht and Popov, "Analysis of Elastic-Plastic Shells of Revolution under Axisymmetric Loading by the Finite Element Method," University of California, Berkeley, Calif., April 1967.

23. Gupta, A. K., Mohraz, B. and Schnobrich, W. C., "Elasto-Plastic Analysis of Three-Dimensional Structures Using the Isoparametric Element," Civil Engineering Studies, SRS No. 381, University of Illinois at Urbana-Champaign, 1971.

24. Larsen, P. K. and Popov, E. P., "Elastic-Plastic Analysis of Thick-Walled Pressure Vessels with Sharp Discontinuities," Paper No. 71-PVP-23, ASME publication.

25. Ellyin, F. and Turkkan, N., "Lower Bound to Limit Pressure of Nozzle-to-Cylindrical Shell Attachment," ASME publication 71-PVP-38.

26. Schroeder, J. and Rangarajan, P., "Upper Bounds to Limit Pressures of Branch-Pipe Tee Connections," Proc. 1st Int. Conf. on Pressure Vessel Technology, Delft and The Hague (1969).

27. Vlasov, V. Z., "Thin-Walled Elastic Beams," 2nd ed., The National Science Foundation, Washington, D.C.

28. Timoshenko, S. and Woinowsky-Krieger, S., "Theory of Plates and Shells," McGraw-Hill, 1959.

29. Taylor, C. E. and Lind, N. C., "Photoelastic Study of the Stresses near Openings in Pressure Vessels," Bulletin 113, Welding Research Council, April 1966.

30. Leven, M. M., "Photoelastic Determination of the Stresses in Reinforced Openings in Pressure Vessels," Bulletin 113, Welding Research Council, April 1966.

31. Leckie, F. A. and Penny, R. K., "Shakedown Loads for Radial Nozzles in Spherical Pressure Vessels," Int. J. Solids, Structures, 3, 1967.

32. Harvey, J. F., "Theory and Design of Modern Pressure Vessels," Van Nostrand Reinhold, New York, 1974.

33. Lind, N. C., "Approximate Stress-Concentration Analysis for Pressurized Branch Pipe Connections," ASME publication 67-WA/PVP-7.

34. Nichols, R. W., "Pressure Vessel Engineering Technology," Elsevier, New York, 1971.

35. Drucker, D. C., "Limit Analysis of Cylindrical Shells under Axially Symmetric Loading," Proc. 1st Midway Conf. on Solid Mechanics, Urbana, Illinois, 1953.

36. Cloud, R. L. and Rodabaugh, E. C., "Approximate Analysis of the Plastic Limit Pressure of Nozzles in Cylindrical Shells," J. of Engineering for Power, Transactions of the ASME, Vol. 90, Series A, No. 2, 1968.

37. Hodge, P. G., "Energy. Virtual Work," Continuum Mechanics, McGraw-Hill, New York, 1970.

38. Desai, C. S. and Abel, J. F., "Introduction to the Finite Element Method," Van Nostrand Reinhold, New York, 1972.

39. Irons, B. M. and Razzaque, A., "Experience with the Patch Test or Convergence of Finite Elements," Proc. of Symp. at University of Maryland, Baltimore, Maryland, June 26-30, 1972. Issued as "The Mathematical Foundation of the Finite Element Method with Application

to Partial Differential Equations," A. K. Aziz, Ed., Academic Press, New York, 1972.

40. Argyris, J. H., "Matrix Analysis of Three-Dimensional Elastic Media, Small and Large Displacements," AIAA Journal, Vol. 3, No. 1, 1965.

41. Turner, M. J., Clough, R. W., Martin, H. C. and Topp, L. J., "Stiffness and Deflection Analysis of Complex Structures," J. Aerospace Sciences, Vol. 23, pp. 805-823, 854, 1956.

42. Hand, F., Pecknold, D. and Schnobrich, W. C., "A Layered Finite Element Non-linear Analysis of Reinforced Concrete Plates and Shells," Structural Studies Series SRS 389, University of Illinois at Urbana-Champaign, 1972.

43. Irons, B. M. and Zienkiewicz, O. C., "The Isoparametric Finite Element System -- A New Concept in Finite Element Analysis," Conf. on Recent Advances in Stress Analysis, Aero. J., Royal Aero. Soc., 1968.

44. Ahmad, S., Irons, B. M. and Zienkiewicz, O. C., "Analysis of Thick and Thin Shell Structures by Curved Finite Elements," Int. J. for Num. Methods in Engin., Vol. 2, pp. 419-451, 1970.

45. Pawsey, S. F., "The Analysis of Moderately Thick to Thin Shells by the Finite Element Method," Ph.D. Thesis, University of Calif., Berkeley, 1969.

46. Doherty, W. P., Wilson, E. L. and Taylor, R. L., "Stress Analysis of Axisymmetric Solids Utilizing Higher Order Quadrilateral Finite Elements," Report No. UC-SESM 69-3, University of Calif., Berkeley, 1970.

47. Zienkiewicz, O. C., Taylor, R. L. and Too, J. M., "Reduced Integration Technique in General Analysis of Plates and Shells," Int. J. of Num. Methods in Engin., Vol. 3, pp. 275-290, 1971.

48. Choi, C.-K. and Schnobrich, W. C., "Use of Non-Conforming Modes in Finite Element Analysis of Plates and Shells," Civil Engineering Studies, SRS No. 401, University of Illinois at Urbana-Champaign, 1973.

49. Dovey, H. H., "Extension of Three Dimension Analysis to Shell Structures Using the Finite Element Idealization," Ph.D. Thesis, University of Calif., Berkeley, 1974.

50. Bridgman, P. W., "Studies in Large Plastic Flow and Fracture with Special Emphasis on the Effects of Hydrostatic Pressure," McGraw-Hill, New York, 1952.

51. Mendelson, A., "Plasticity -- Theory and Application," MacMillan, New York, 1968.

52. Zienkiewicz, O. C., Valliappan, S. and King, I. P., "Elasto-Plastic Solutions of Engineering Problems -- 'Initial Stress,' Finite Element Approach," Int. J. Num. Meth. in Eng., Vol. 1, pp. 75-100, 1969.

53. Oden, J. T., "Finite Elements of Nonlinear Continua," McGraw-Hill, New York, 1972.

54. Tillerson, J. R., "A Treatise on Nonlinear Finite Element Analysis," Ph.D. Thesis, A&M University, Texas, 1973.

55. Salem, M. H. and Mohraz, B., "Nonlinear Analysis of Planar Reinforced Concrete Structures," Civil Engineering Studies, SRS No. 410, University of Illinois at Urbana-Champaign, 1974.

56. Nayak, G. C. and Zienkiewicz, O. C., "Elasto-Plastic Stress Analysis. A Generalization for Various Constitutive Relations Including Strain Softening," Int. J. Num. Meth. in Eng., Vol. 5, 1972.

57. Cook, R. D., "Concepts and Applications of Finite Element Analysis," John Wiley & Sons, New York, 1974.

58. Pecknold, D. A. and Schnobrich, W. C., "Finite Element Analysis of Skewed Shallow Shells," Civil Engineering Studies, SRS No. 332, University of Illinois at Urbana-Champaign, 1968.

59. Cantin, G. and Clouth, R. W., AIAA Journal 6, 1057 (1968).

60. Ashwell, D. G. and Sabir, A. B., "A New Cylindrical Shell Finite Element Based on Simple Independent Strain Functions," Int. J. Mech. Science, Pergamon Press, 1972, Vol. 14, pp. 171-183.

61. Lindberg, G. M., Olson, M. D. and Cowper, G. R., "New Development in the Finite Element Analysis of Shells," N.R.C. of Canada, Ottawa, Jan. 1970.

62. Razzaque, A., "Finite Element Analysis of Plate and Shells," Ph.D. Thesis, University of Wales, Swansea, 1972.

63. Prager, W. and Hodge, P. G., "Theory of Perfectly Plastic Solids," Wiley, New York, 1951.

64. Hodge, P. G., "An Introduction to the Mathematical Theory of Perfectly Plastic Solids," A11-S2/396, Graduate Division of Applied Mathematics, Brown University, Providence, R.I., Feb. 1950.

65. Tagart, S. W., "Plastic Fatigue Analysis of Pressure Components," ASME Pressure Vessels and Piping: Design and Analysis, Vol. 1, 1972.
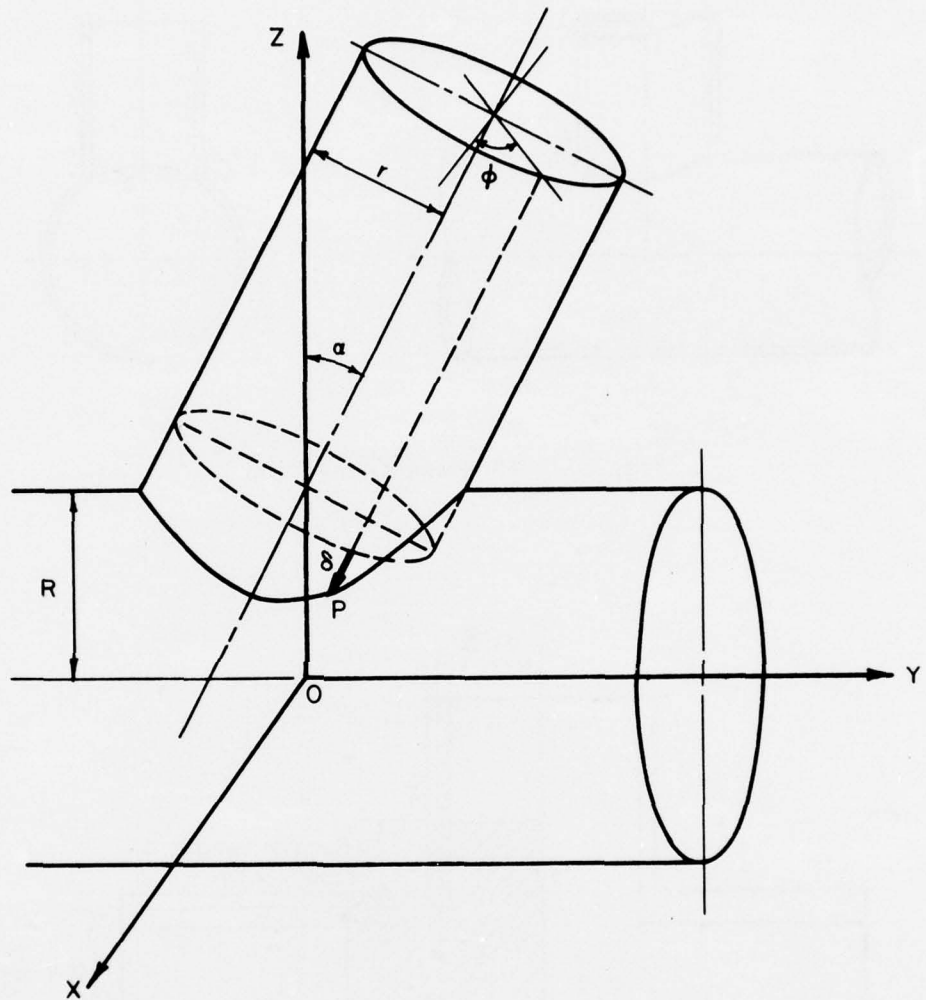
Fig. 1   Intersecting Cylinders with an Intersection Angle α
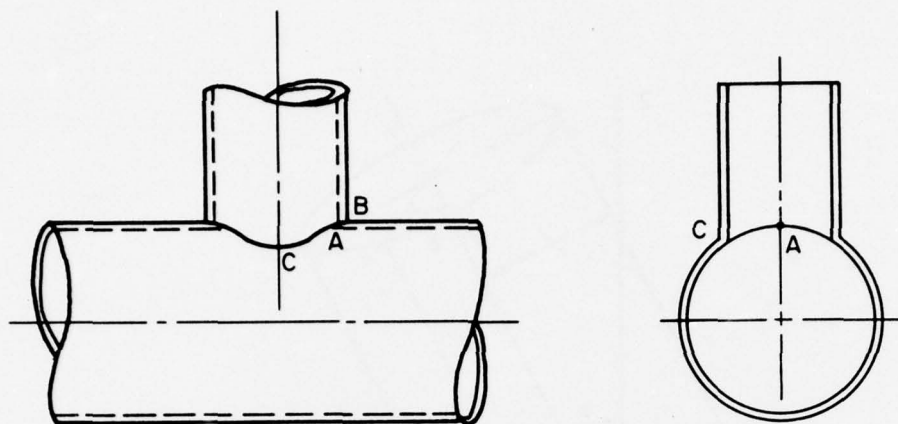
Fig. 2   "T" Shape Connection

Fig. 3   Area Method

83
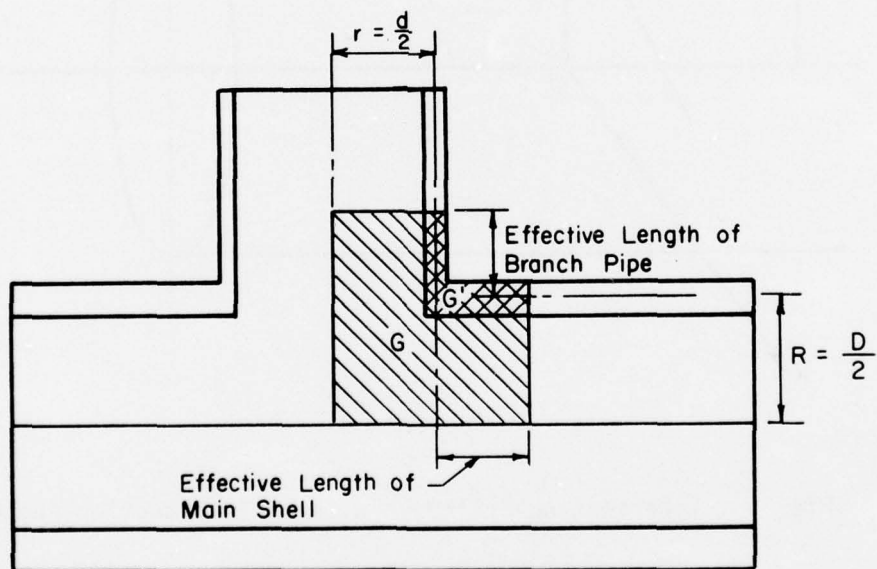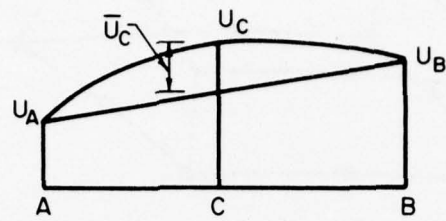
Fig. 4   Quadratic Displacement Variation along AB
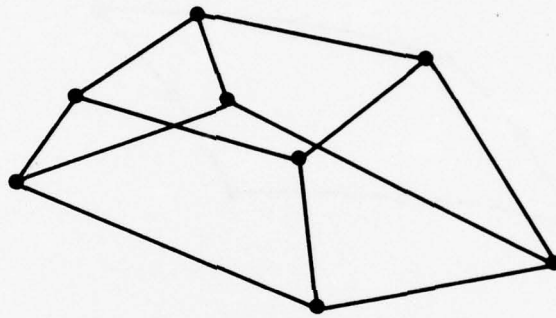
Fig. 5   8-node Brick Type Element
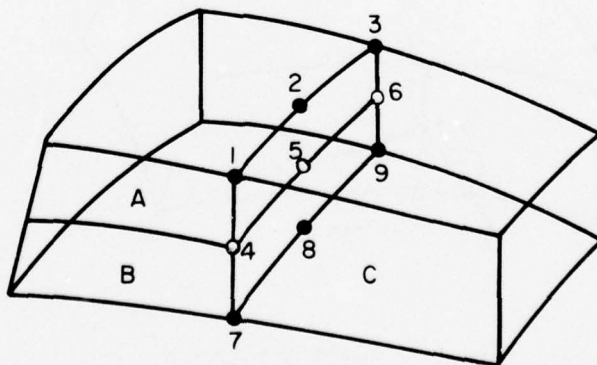
Fig. 6   3-D Transitional Element

84
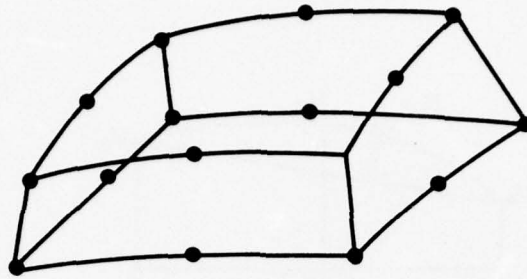
Fig. 7   Thick Shell Element
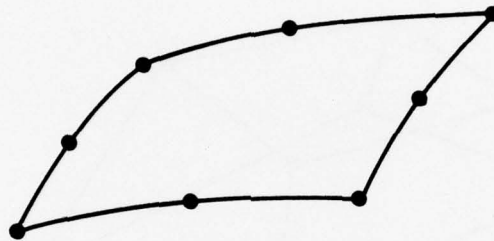
Fig. 8   Two-Dimensional Quadrilateral Element
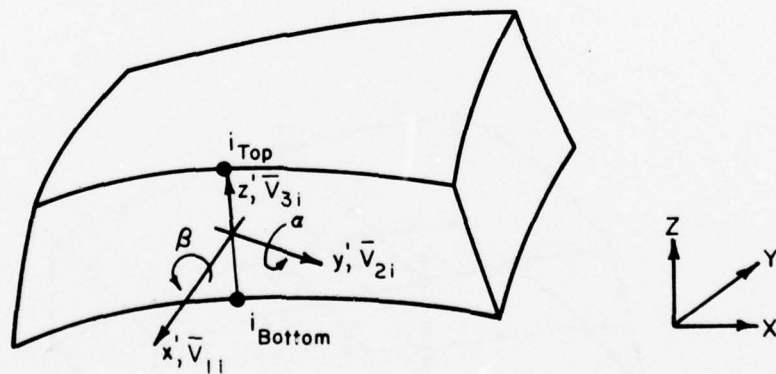
Fig. 9   Ahmad's Element
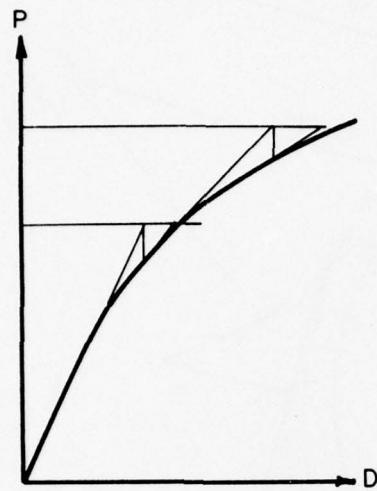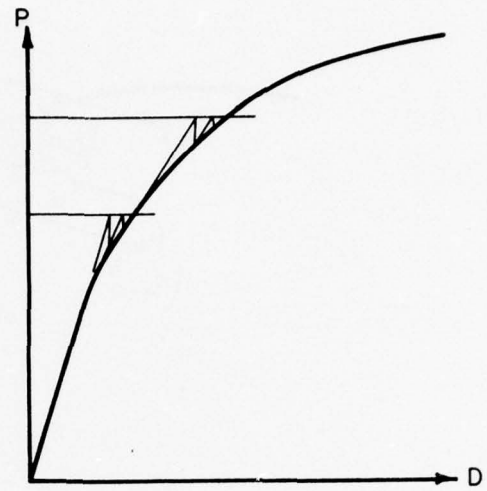
(a) Newton-Raphson Method   (b) Modified Newton-Raphson Method
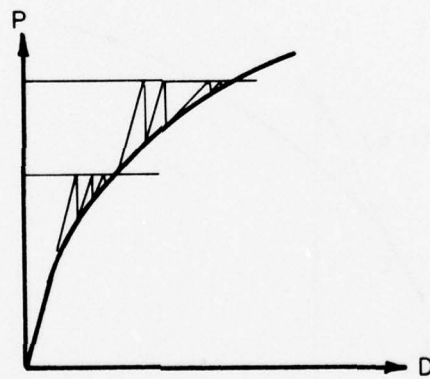
(c) Incremental-iterative Method

Fig. 10   Graphic Representation of Nonlinear Problem Solutions

86
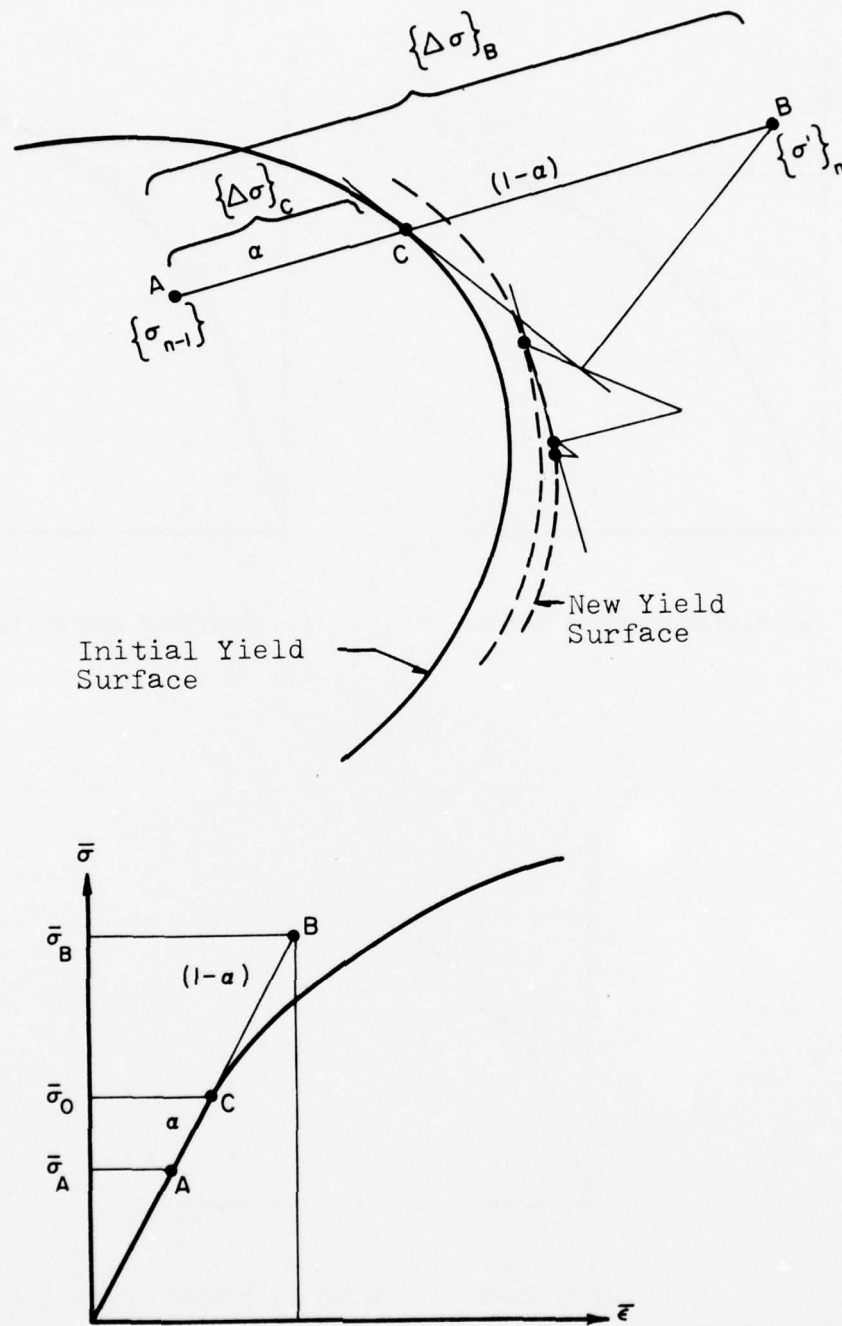
Fig. 11   Graphic Interpretation of Incremental-iterative Method
and Linear Interpolation Factor
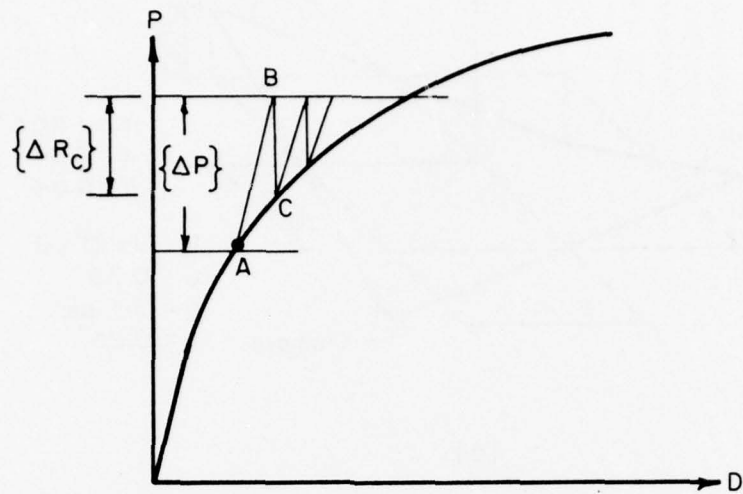
Fig. 12   Excess Nodal Forces with Initial Stiffness
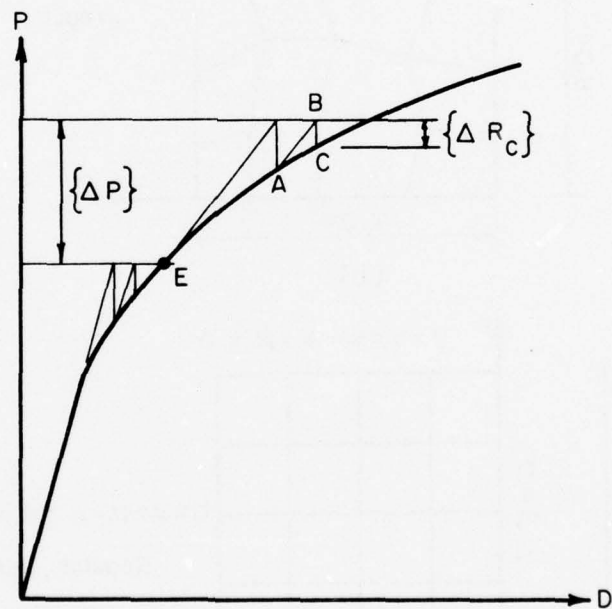
Fig. 13   Excess Nodal Forces with Updated Stiffness
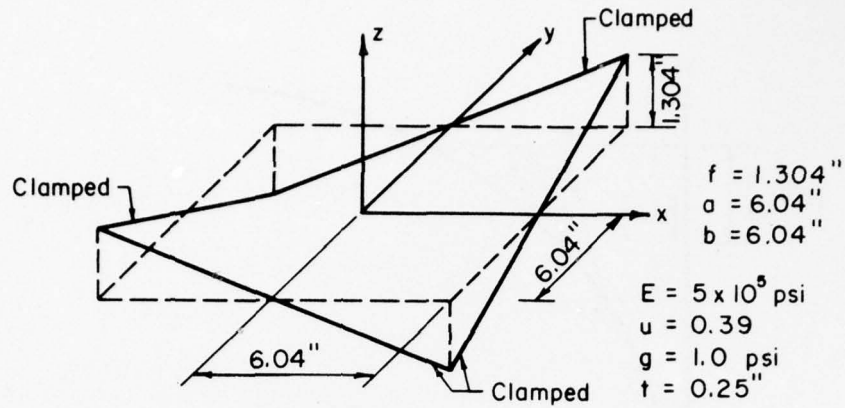
(a)
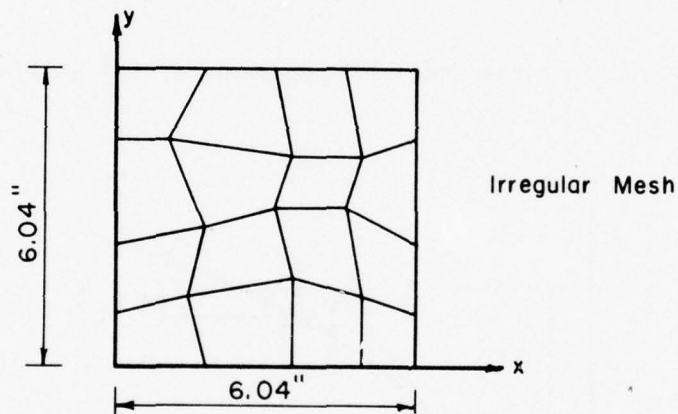
(b)
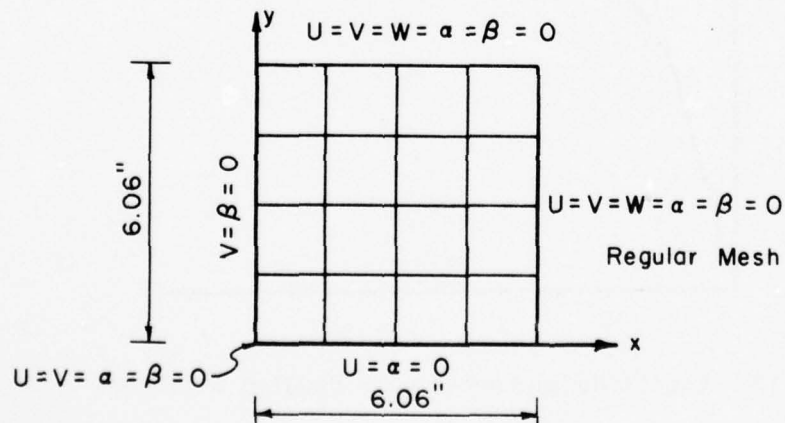
(c)

Fig. 14   Clamped Hyperbolic Parabolic under Uniform Normal Load
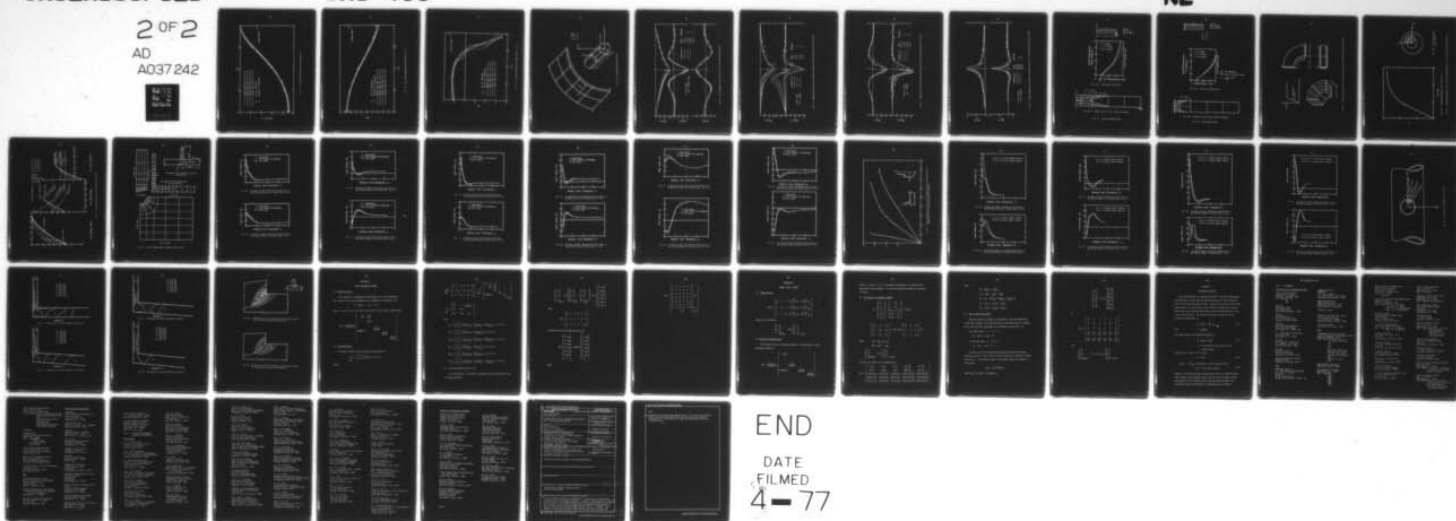
END

DATE
FILMED
4-77
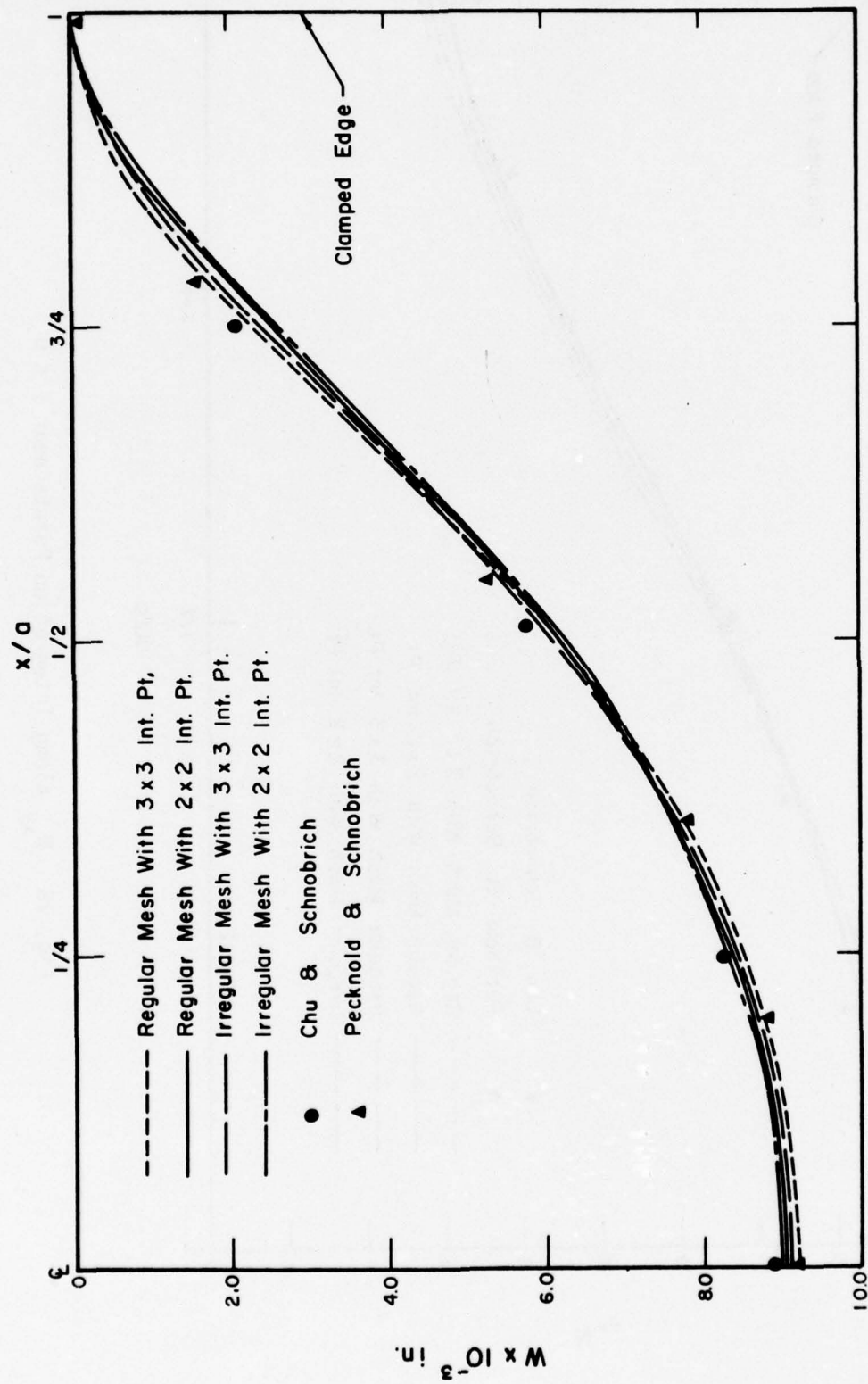
Fig. 15 Vertical Deflection across Midspan Y = 0
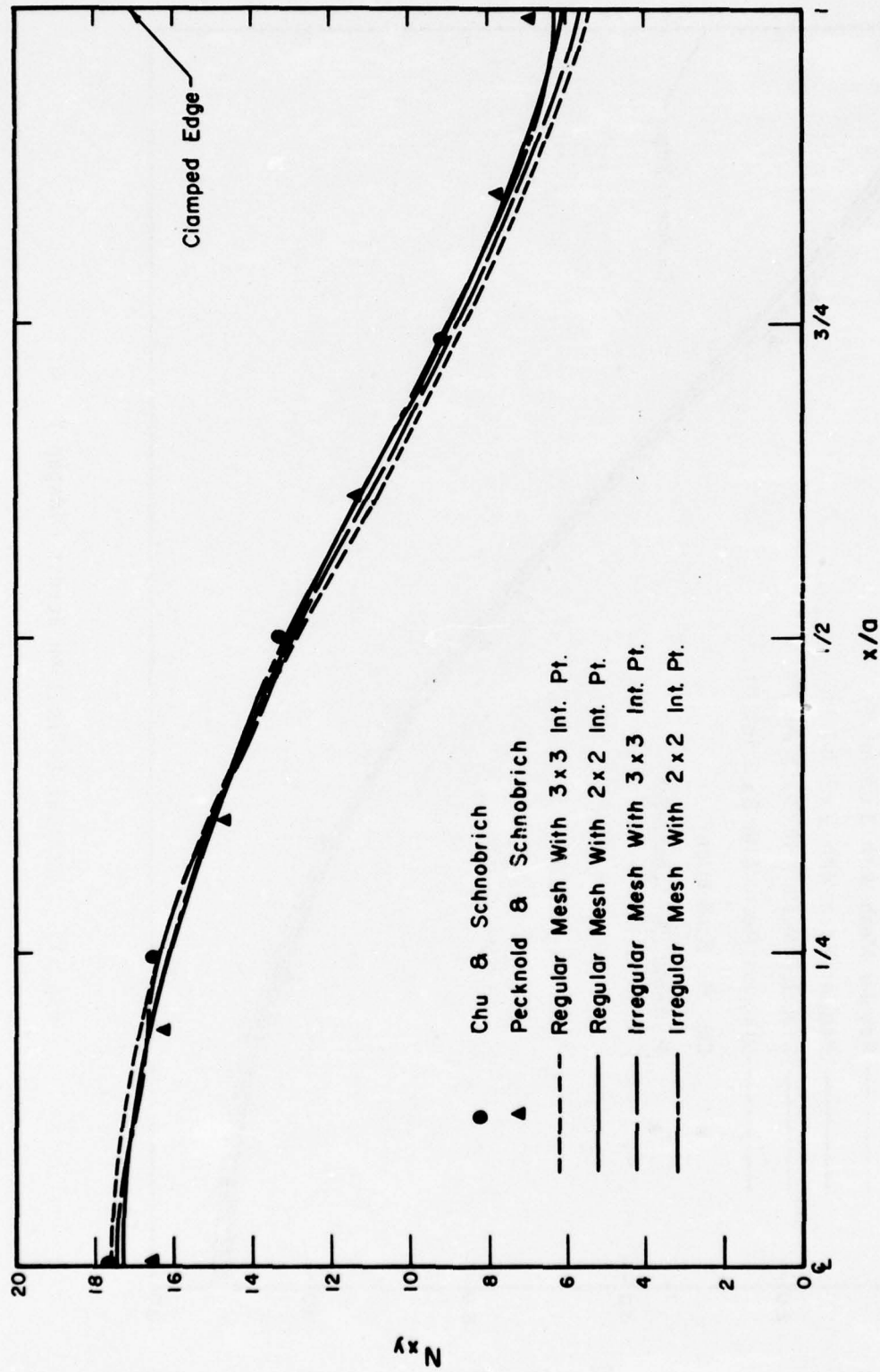
Fig. 16 N_{xy} along Integration Points near $Y = 0$
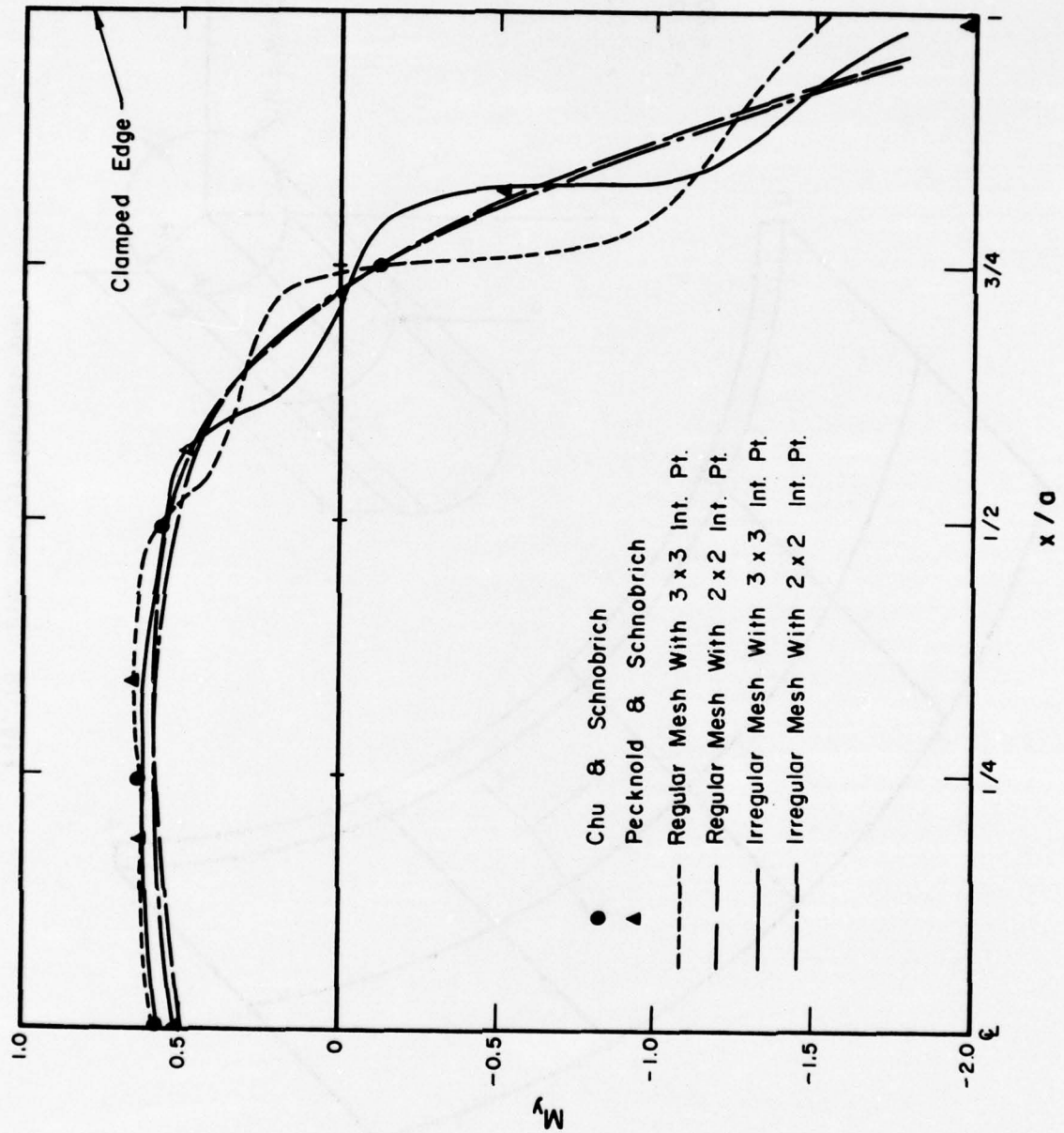
Fig. 17 M_y along Integration Points near Y = 0

92

$L = 200$
$R = 100$
$t = 1$
$\nu = 0.3$
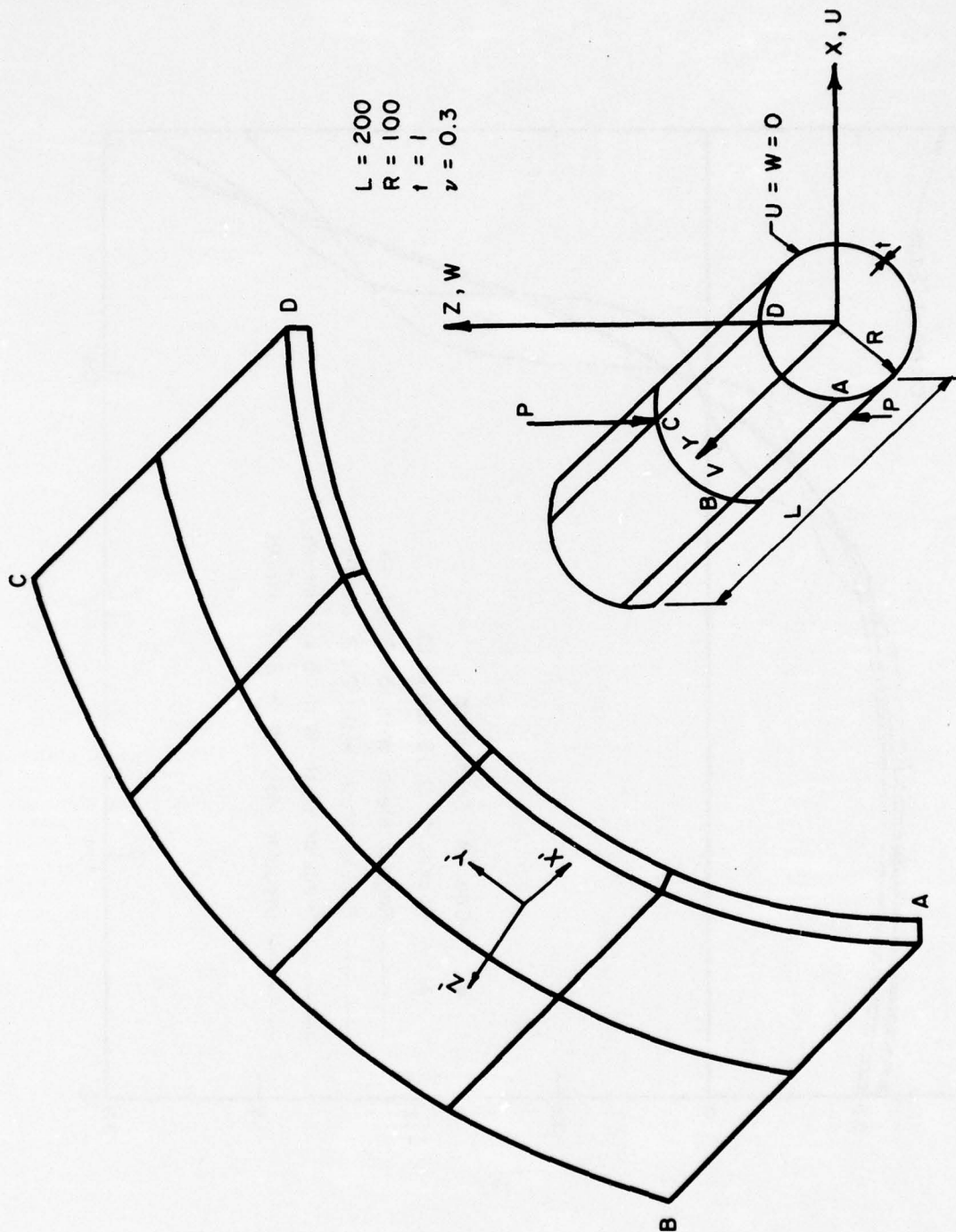
Fig. 18   Pinched Cylindrical Shell
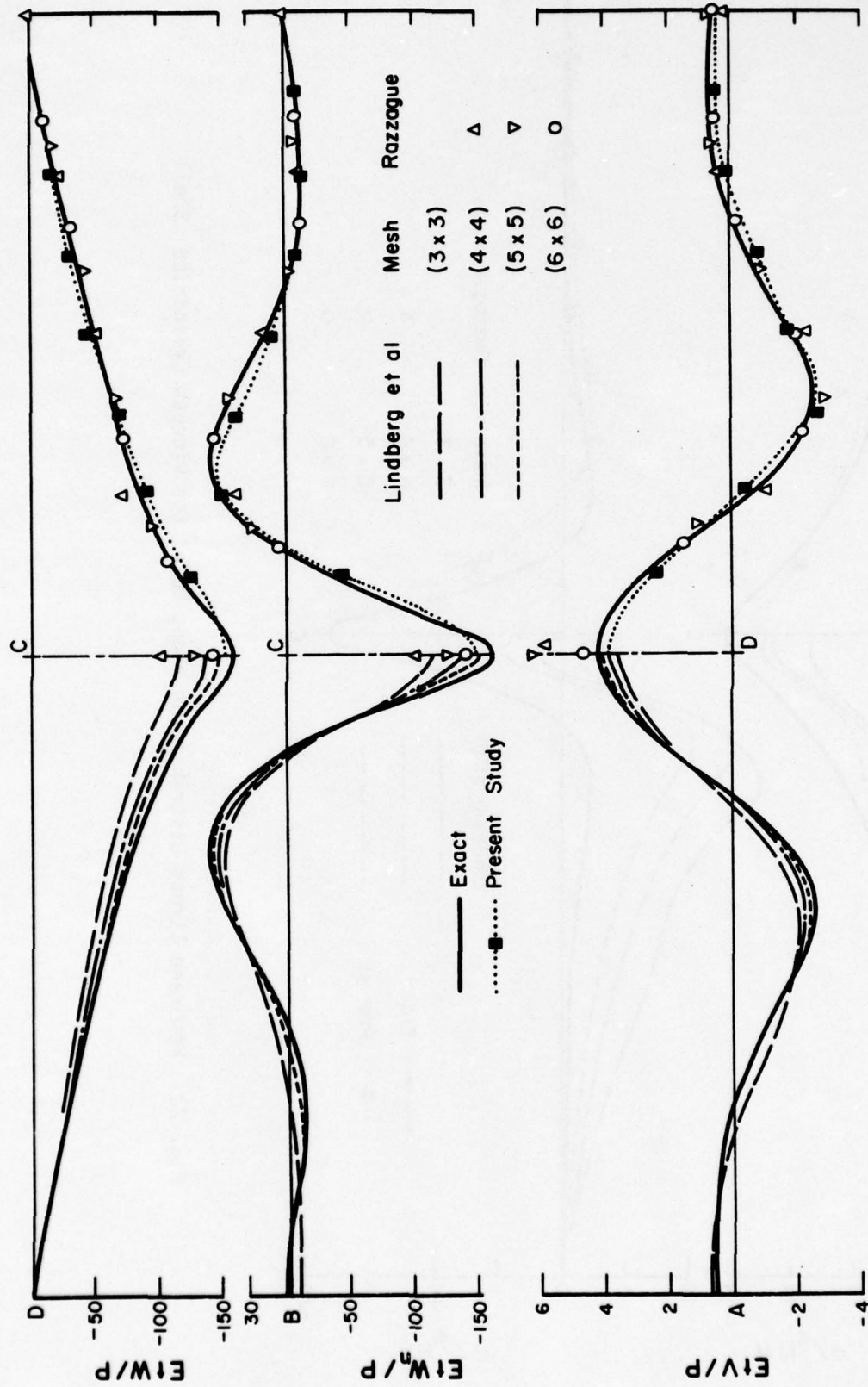
Fig. 19   Displacement Distributions for Pinched Cylindrical Shell
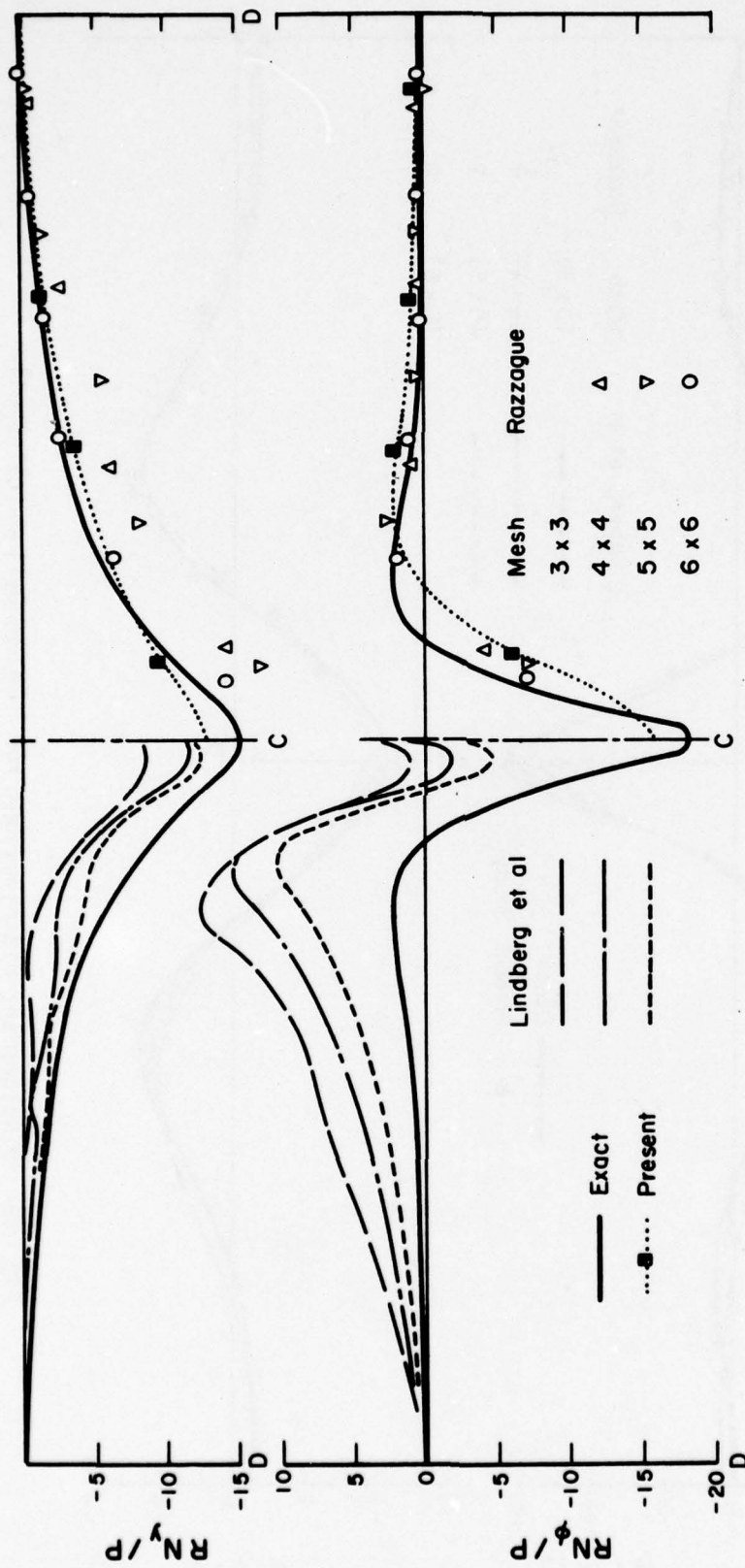
Fig. 20   Membrane Stress Distributions along DC of the Pinched Cylindrical Shell
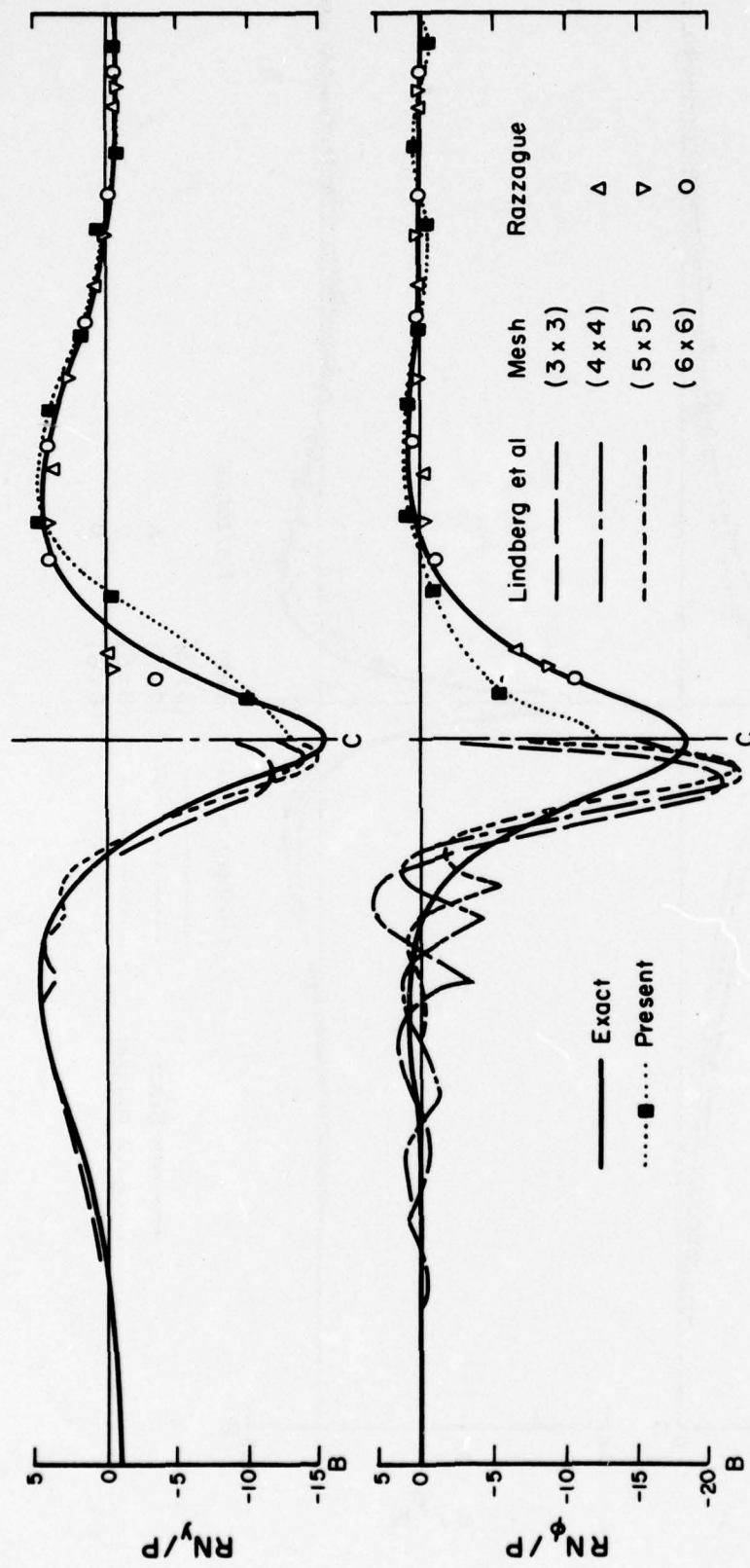
Fig. 21 Membrane Stress Distributions along BC of the Pinched Cylindrical Shell
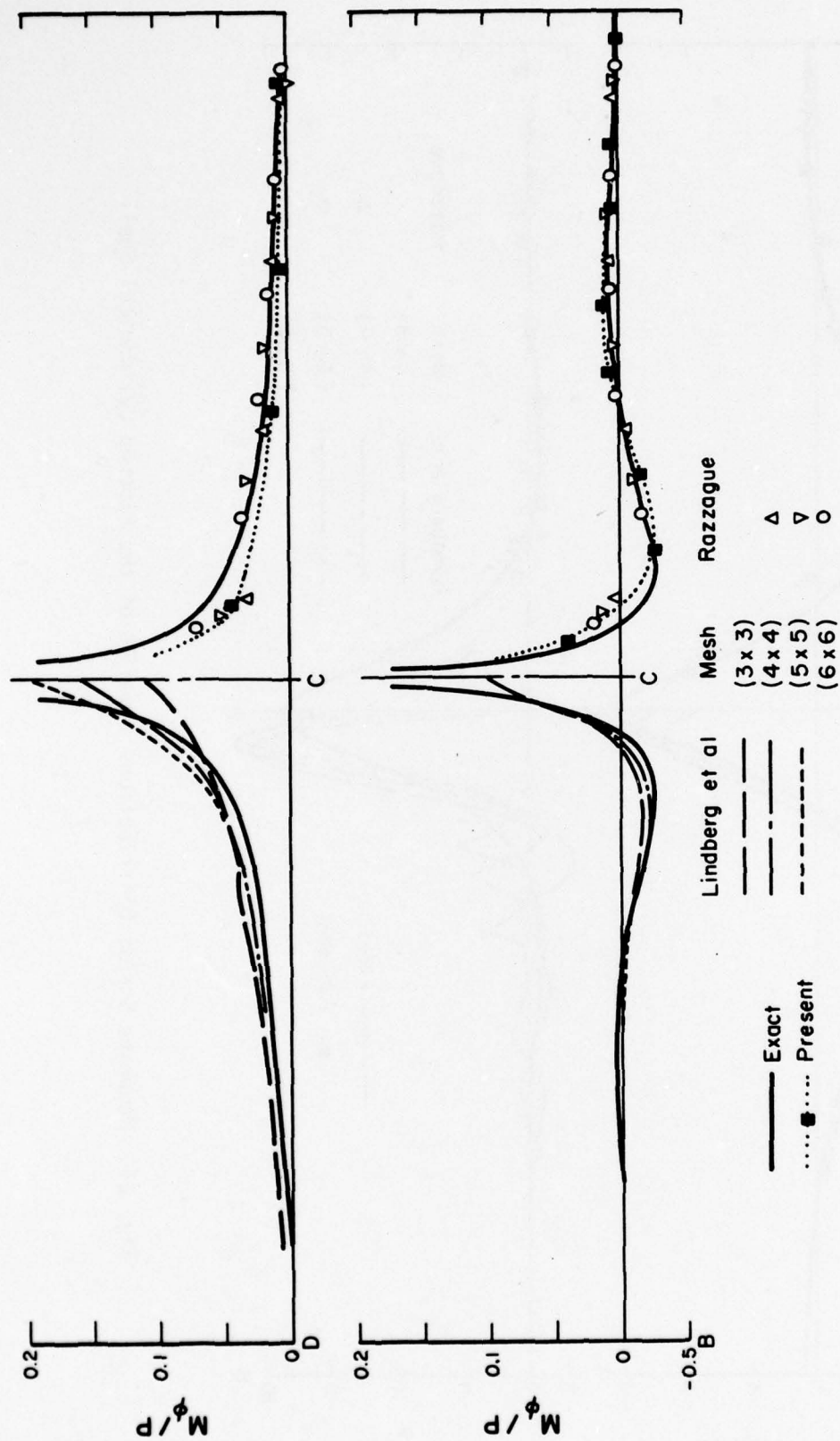
Fig. 22   Bending Moment Distributions along DC and BC of the Pinched Cylindrical Shell
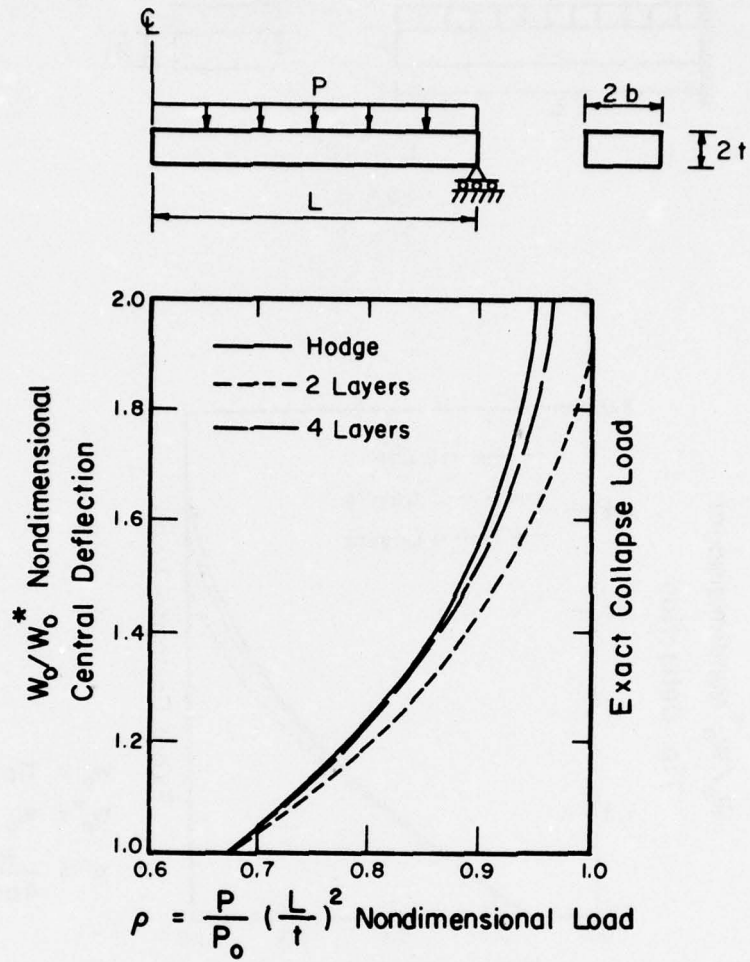
Fig. 23a   Load versus Deflection
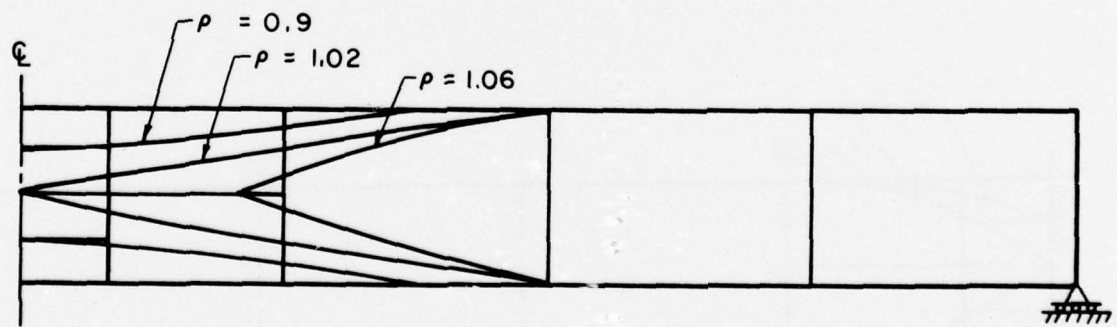
Fig. 23b   Progression of Elastic-Plastic Boundary

Fig. 23   Simply Supported Beam

$$L = 12''$$
$$2b = 3''$$
$$2t = 2''$$

W_o = Tip Deflection

W_o^* = W_o At Initial Field Load
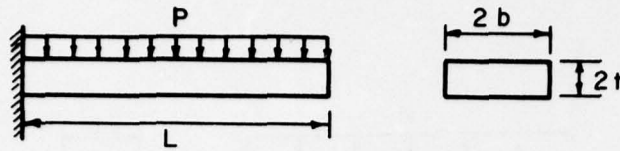
$$\rho = \frac{P}{4b\sigma_y} \left(\frac{L}{t}\right)^2$$
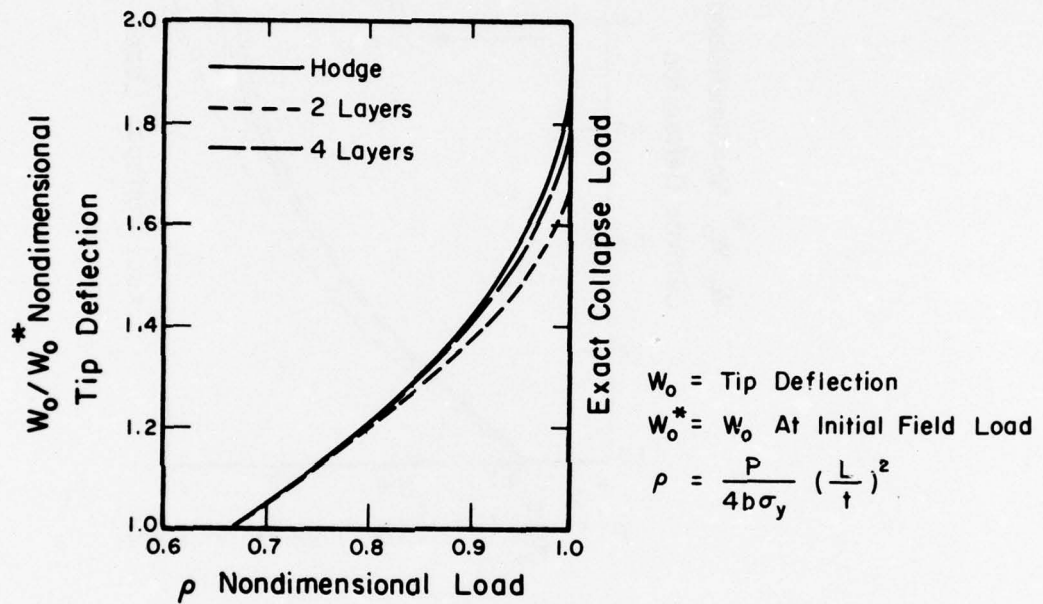
Fig. 24a   Load versus Deflection
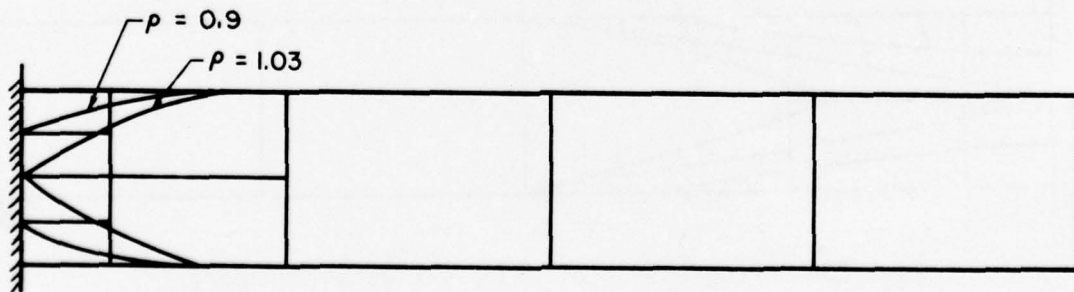
Fig. 24b   Progression of Elastic-Plastic Boundary

Fig. 24   Cantilevered Beam

99
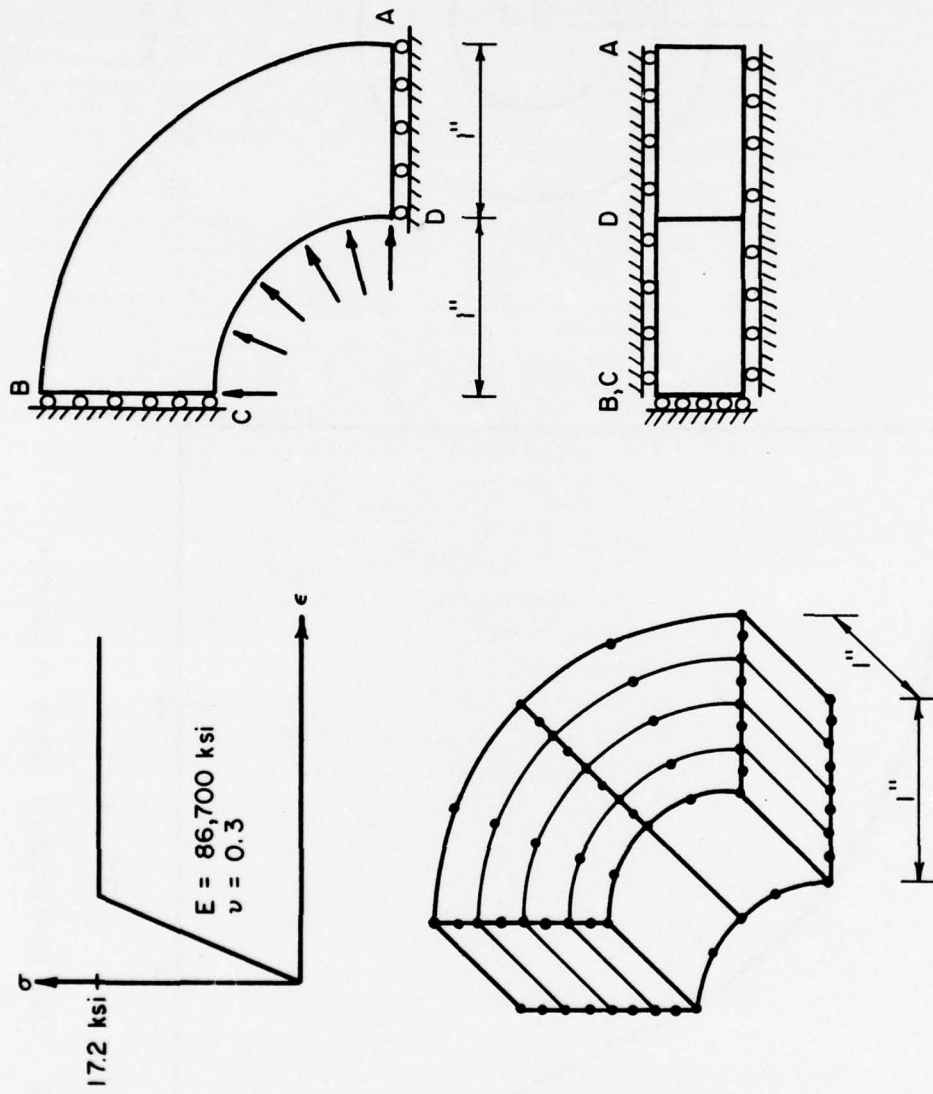
Fig. 25   Thick Hollow Circular Cylinder Subjected to a Uniform Internal Pressure

E = 86,700 ksi
ν = 0.3

17.2 ksi

100

Fig. 26b   Plastified Region
at p = 12.6

Fig. 26a   Load-displacement Curve at Point A

Fig. 26   Load-displacement Curve and Plastified Region of a Thick-walled Pressure Vessel
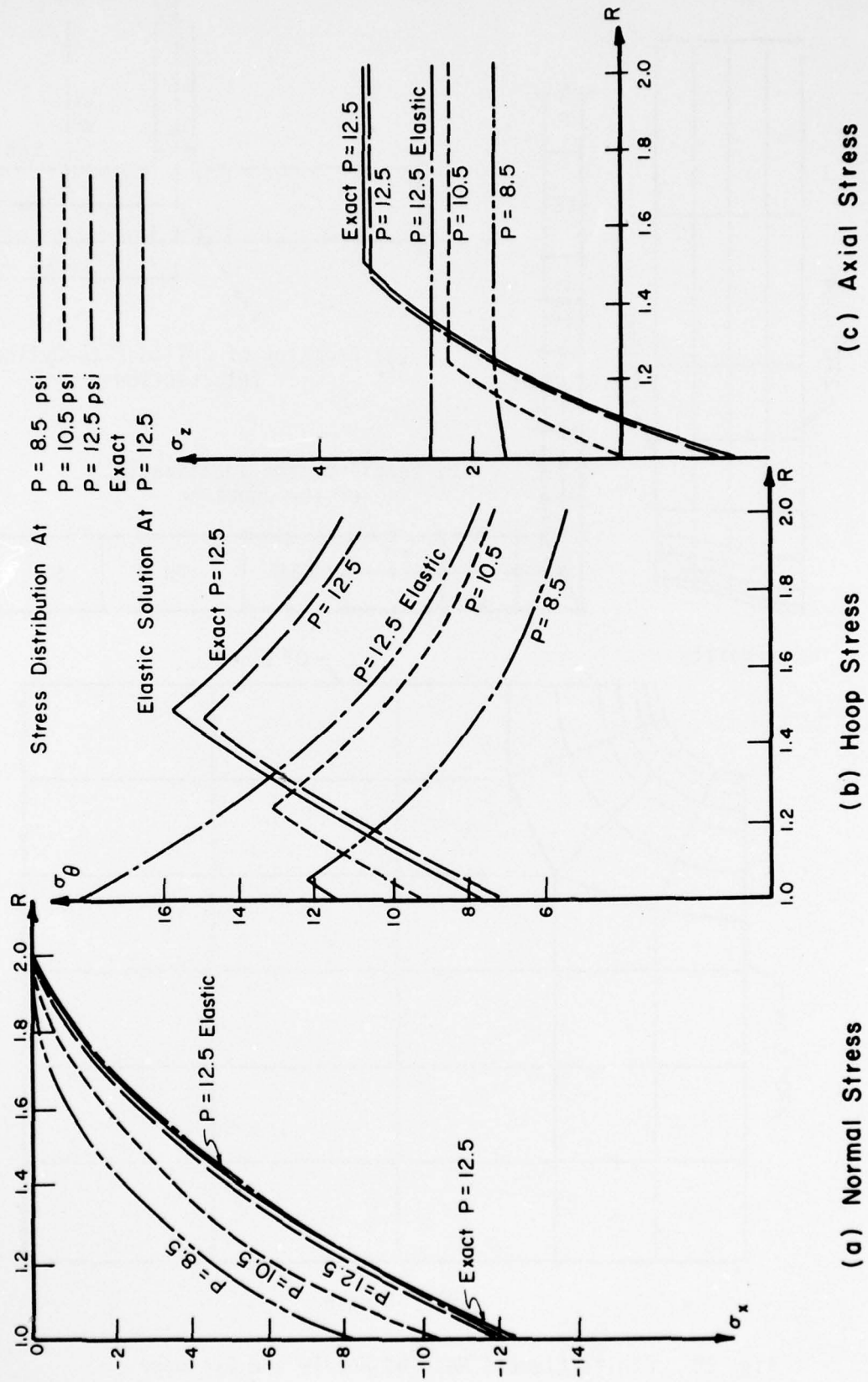
Fig. 27   Stress Variations in Different Load Levels

(a) Normal Stress

(b) Hoop Stress

(c) Axial Stress

(a) Geometry of Cylinder-to-Cylinder Intersection

(b) Detail of the Idealization of the Junction
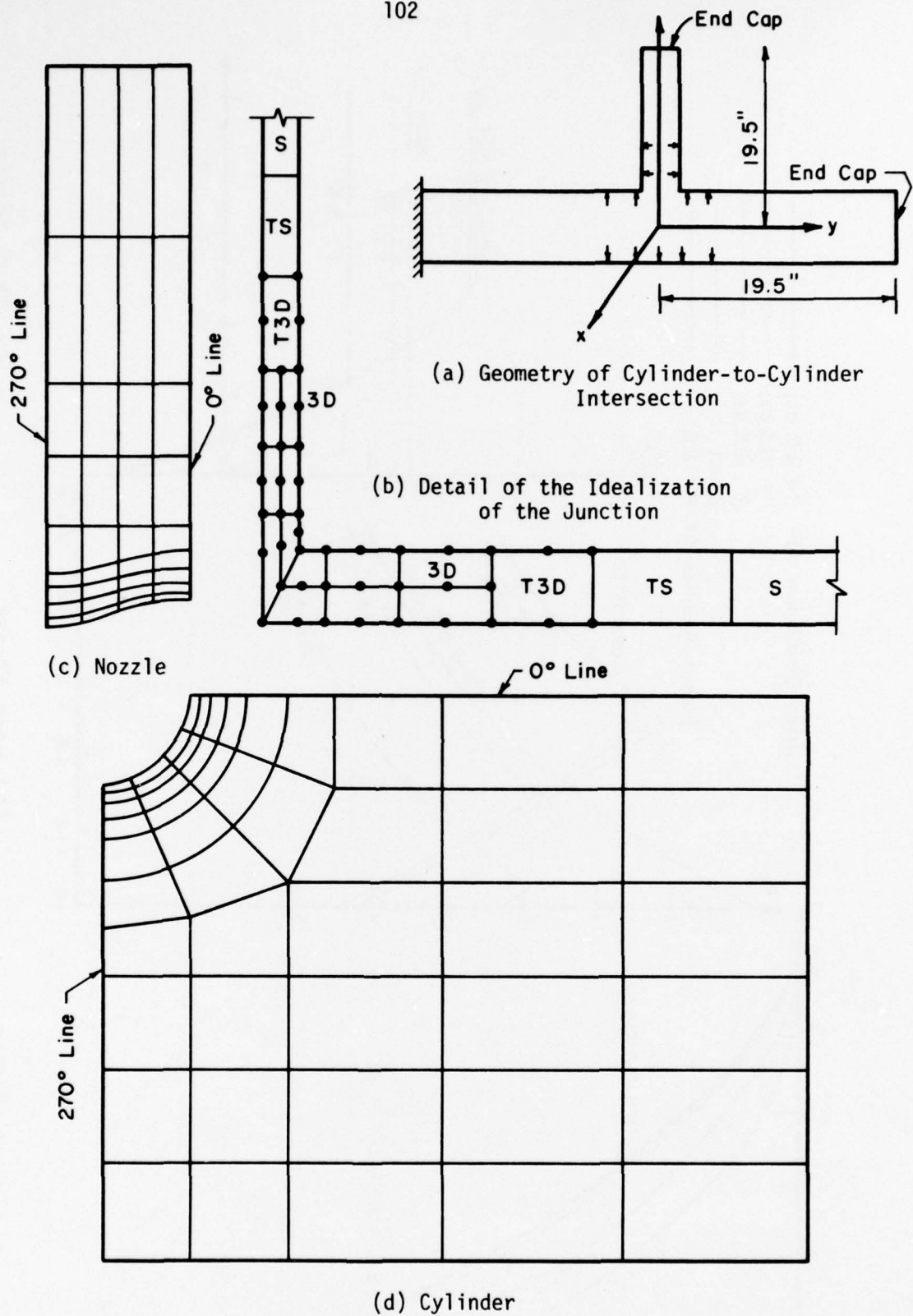
(c) Nozzle

(d) Cylinder

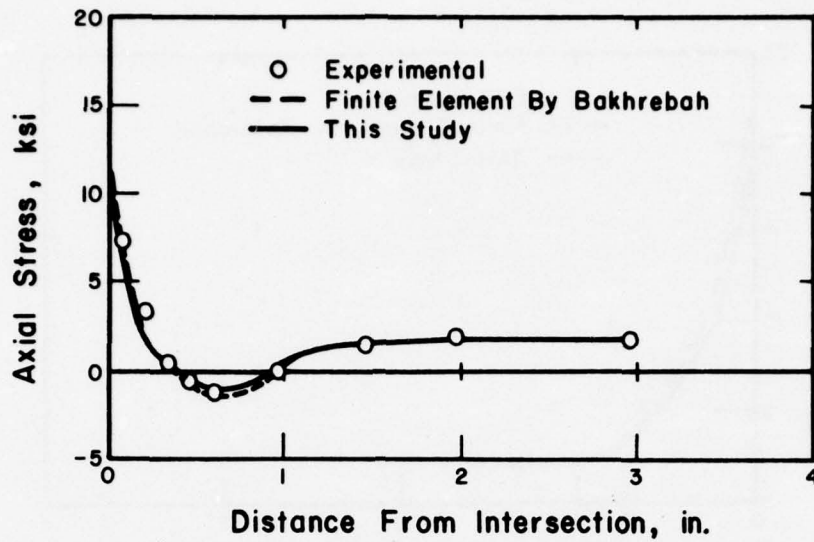Fig. 28   Finite Element Mesh of Nozzle and Cylinder
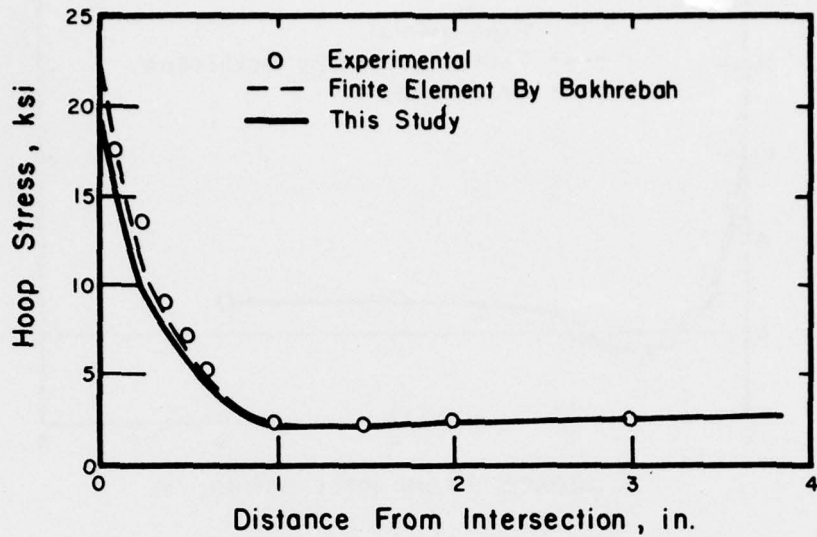
Fig. 29   Cylinder-Cylinder Intersection Hoop Stress in
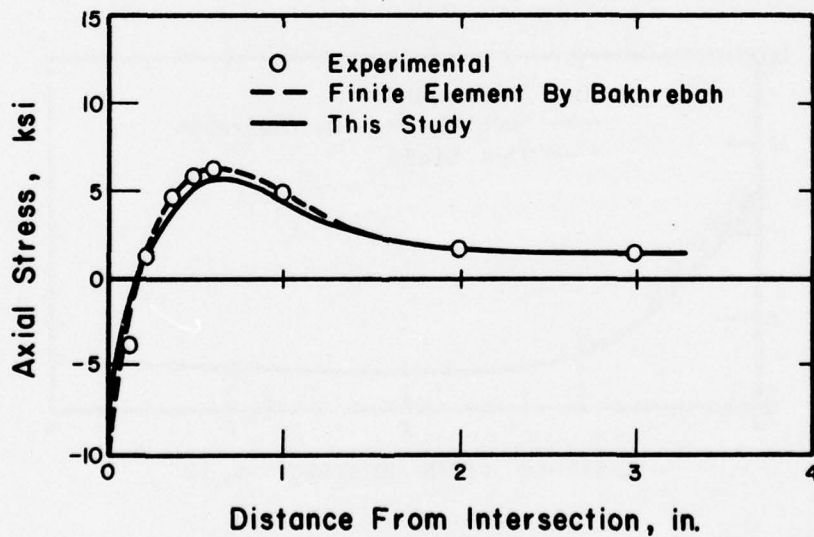   the Outside Surface of Cylinder near 0° Line
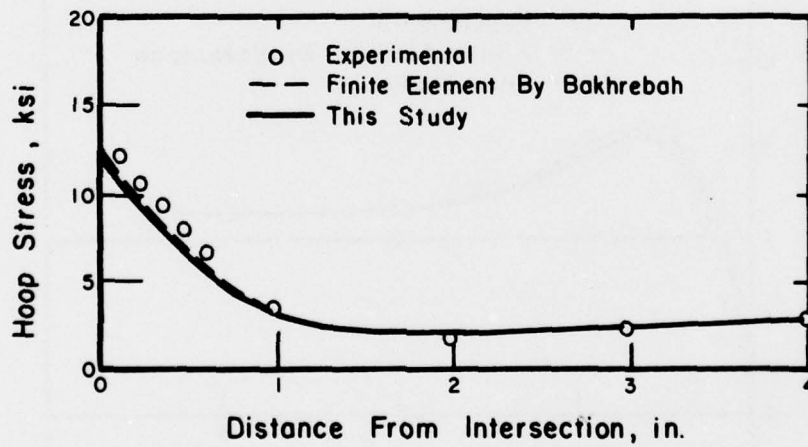
Fig. 30   Cylinder-Cylinder Intersection Hoop Stress in
           the Inside Surface of Cylinder near 0° Line

Fig. 31   Cylinder-Cylinder Intersection Axial Stress in
the Outside Surface of Cylinder near 0° Line

Fig. 32   Cylinder-Cylinder Intersection Axial Stress in
the Inside Surface of Cylinder near 0° Line

105
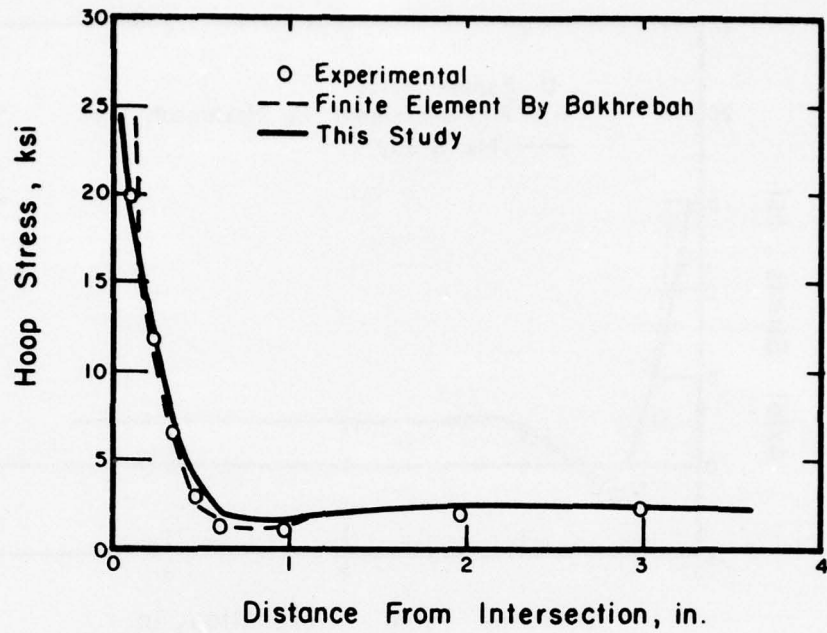

Fig. 33   Cylinder-Cylinder Intersection Hoop Stress
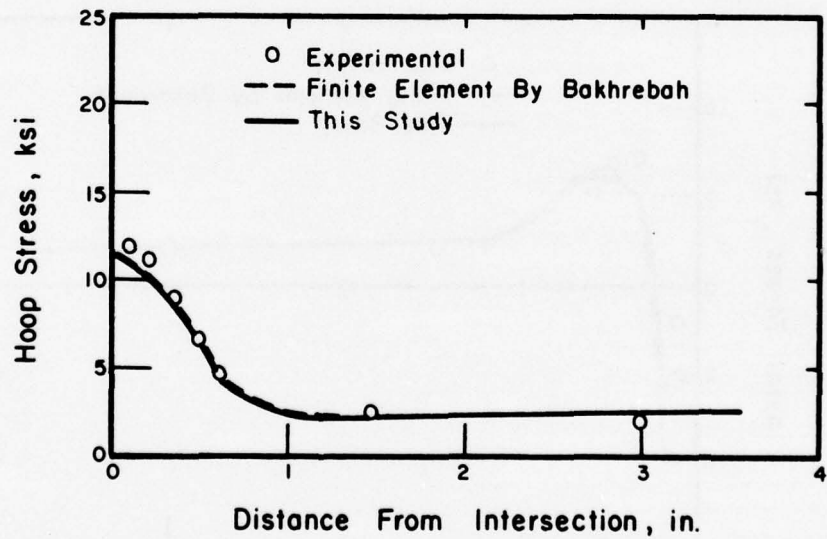in the Outside Surface of Nozzle near 0° Line

Fig. 34   Cylinder-Cylinder Intersection Hoop Stress
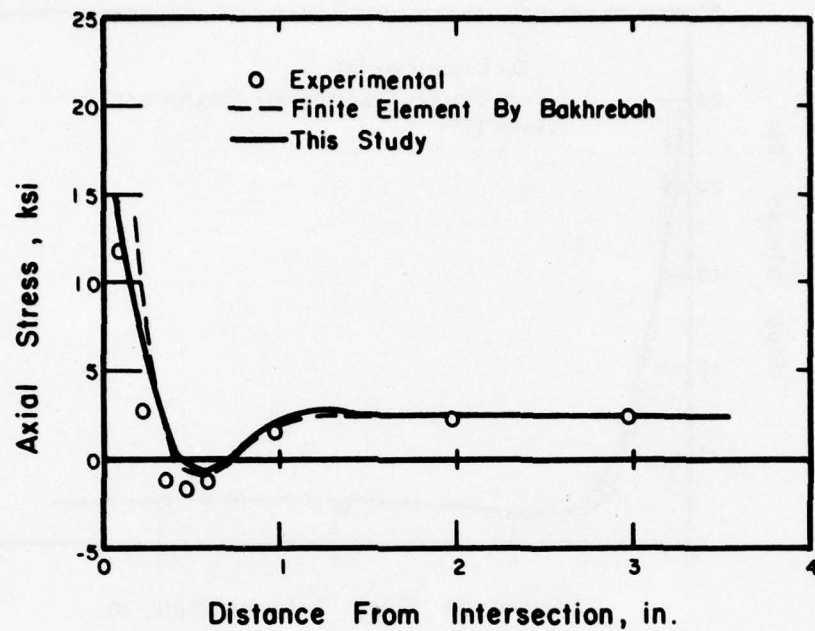in the Inside Surface of Nozzle near 0° Line

Fig. 35   Cylinder-Cylinder Intersection Axial Stress in
the Outside Surface of Nozzle near 0° Line
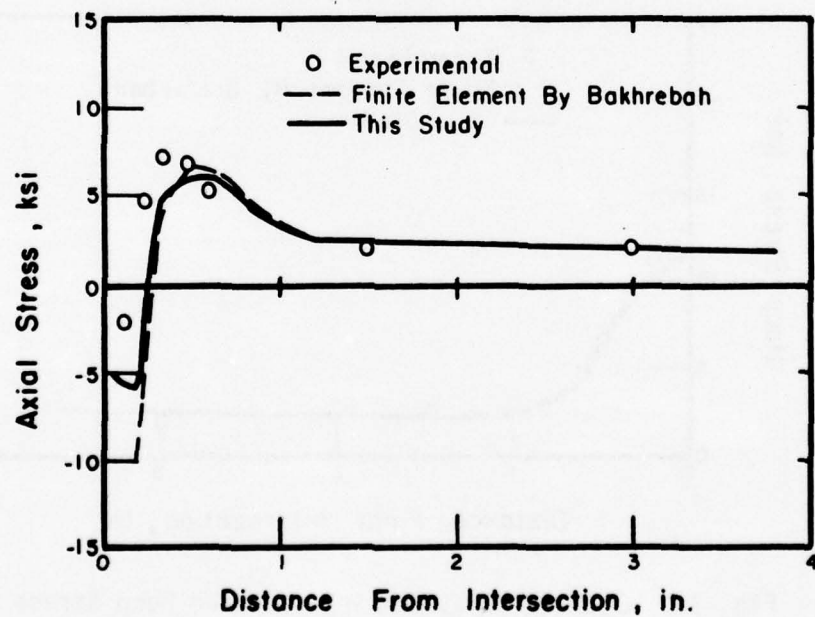

Fig. 36   Cylinder-Cylinder Intersection Axial Stress in
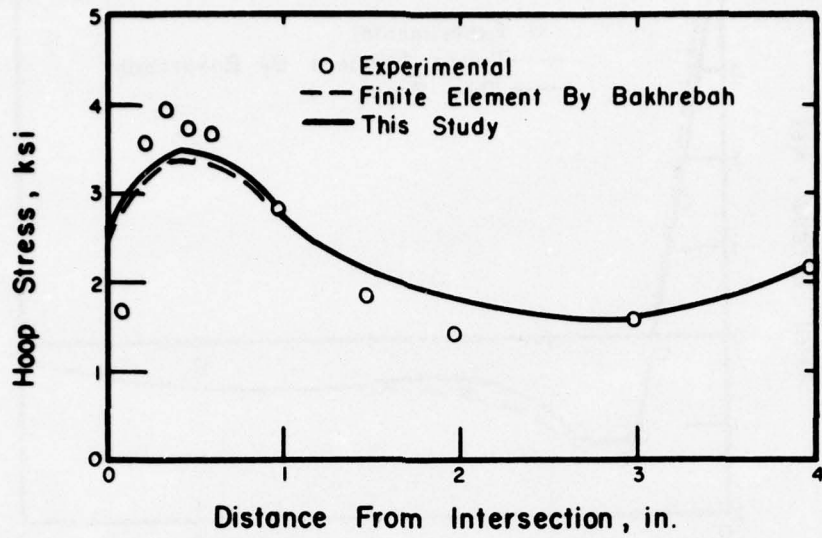the Inside Surface of Nozzle near 0° Line

Fig. 37   Cylinder-Cylinder Intersection Hoop Stress in
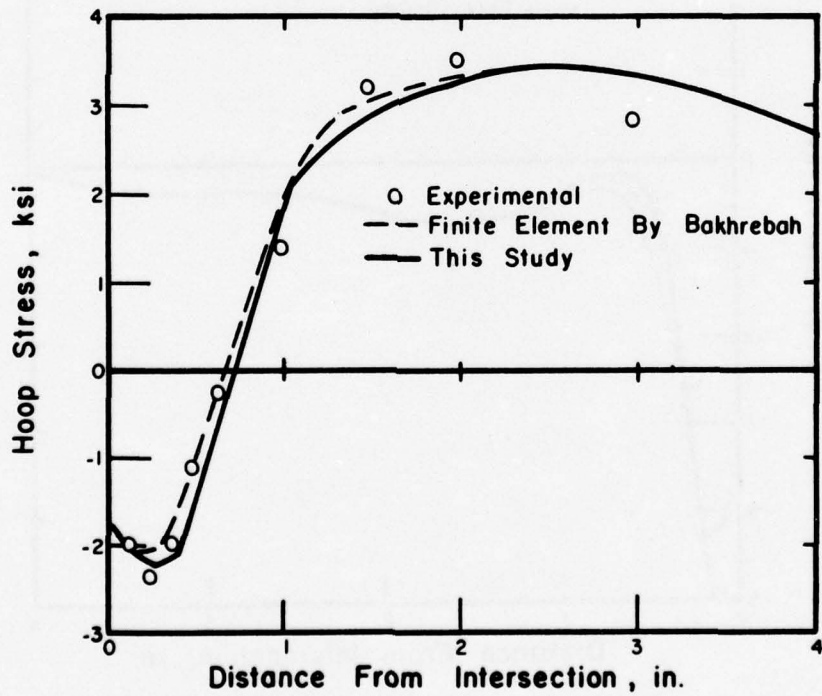the Outside Surface of Cylinder near 270° Line

Fig. 38   Cylinder-Cylinder Intersection Hoop Stress in
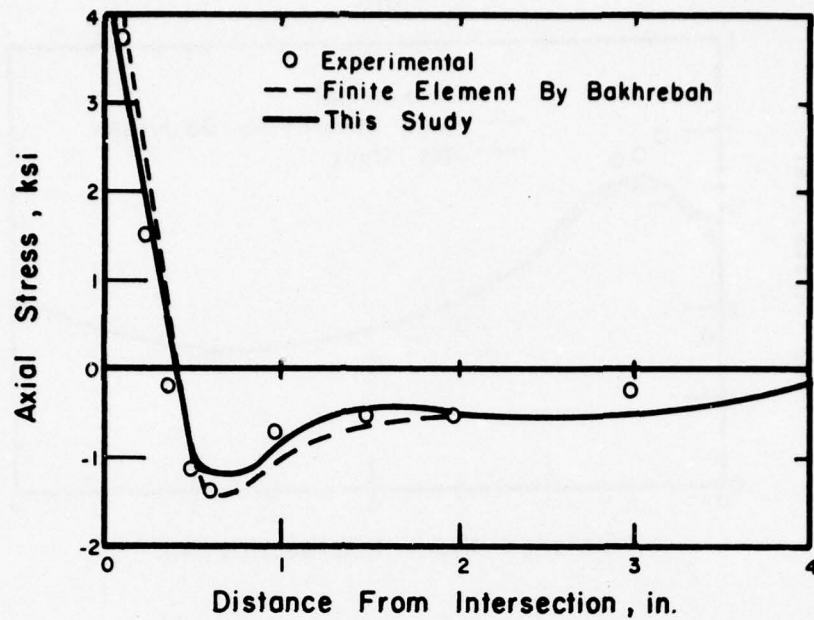the Inside Surface of Cylinder near 270° Line

Fig. 39   Cylinder-Cylinder Intersection Axial Stress in
the Outside Surface of Nozzle near 270° Line

Fig. 40   Cylinder-Cylinder Intersection Axial Stress in
the Inside Surface of Nozzle near 270° Line
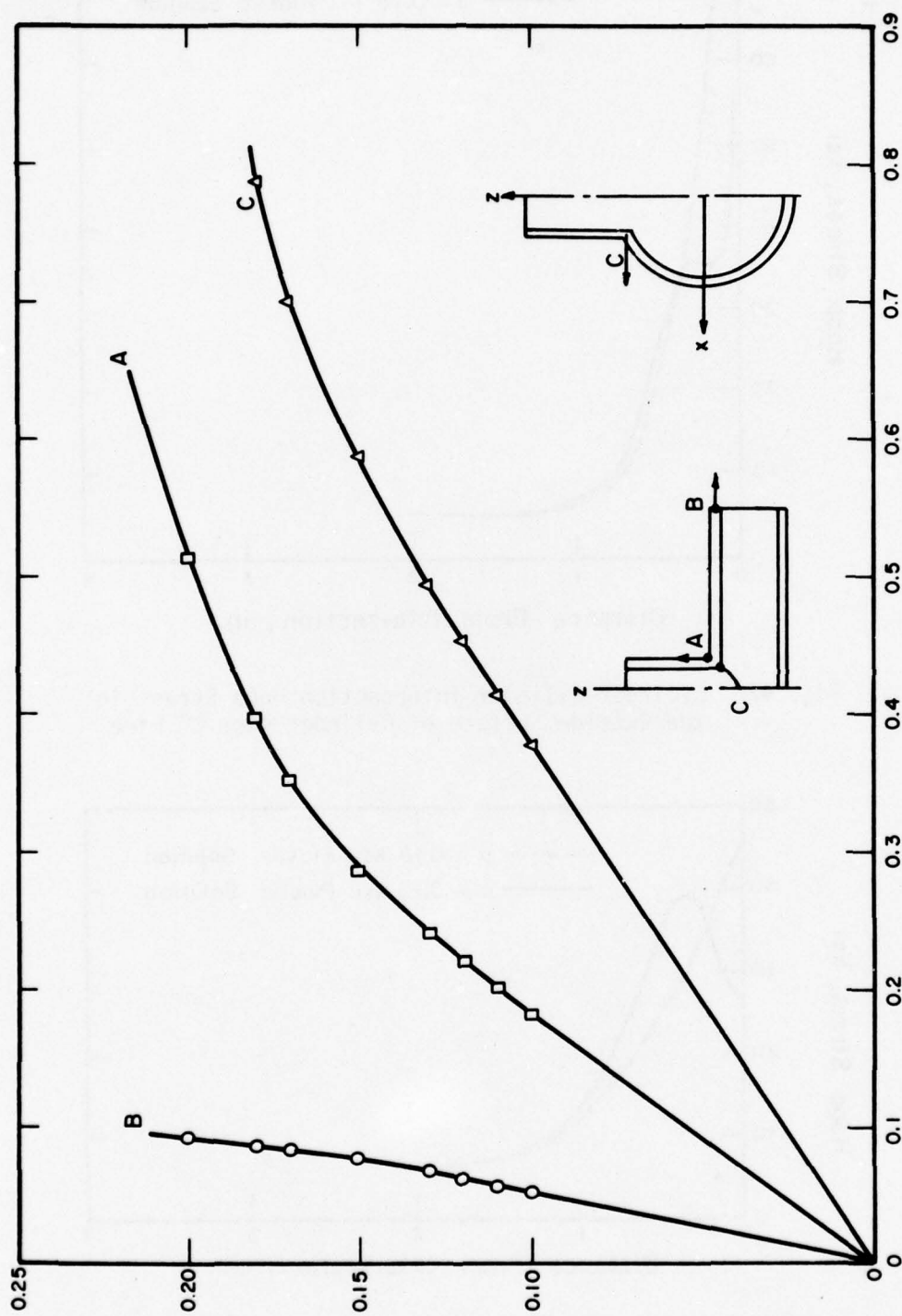
Fig. 41 Load-Displacement Curves for Cylinder-to-Cylinder Intersection
Subjected to an Increasing Internal Pressure

Fig. 42   Cylinder-Cylinder Intersection Hoop Stress in the Outside Surface of Cylinder near 0° Line

Fig. 43   Cylinder-Cylinder Intersection Hoop Stress in the Inside Surface of Cylinder near 0° Line
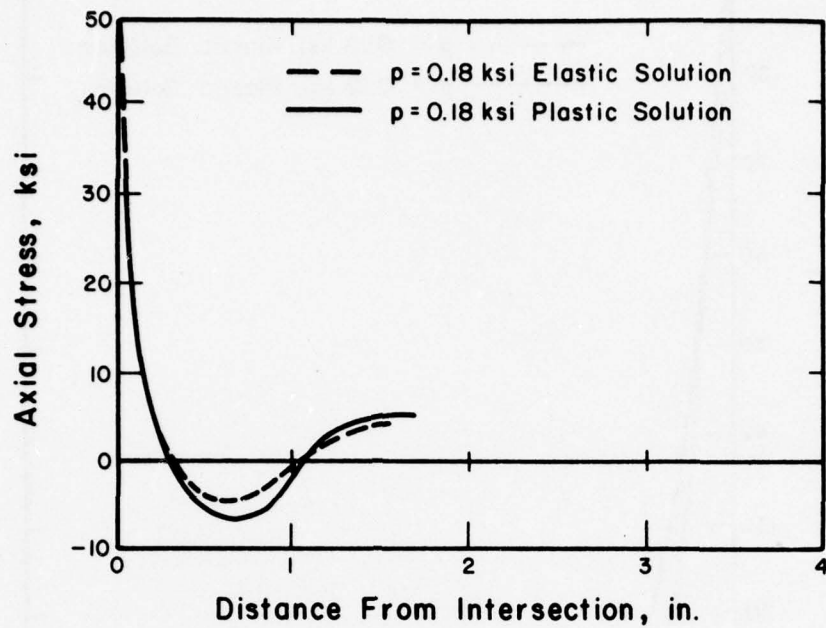
Fig. 44   Cylinder-Cylinder Intersection Axial Stress in the Outside Surface of Cylinder near 0° Line
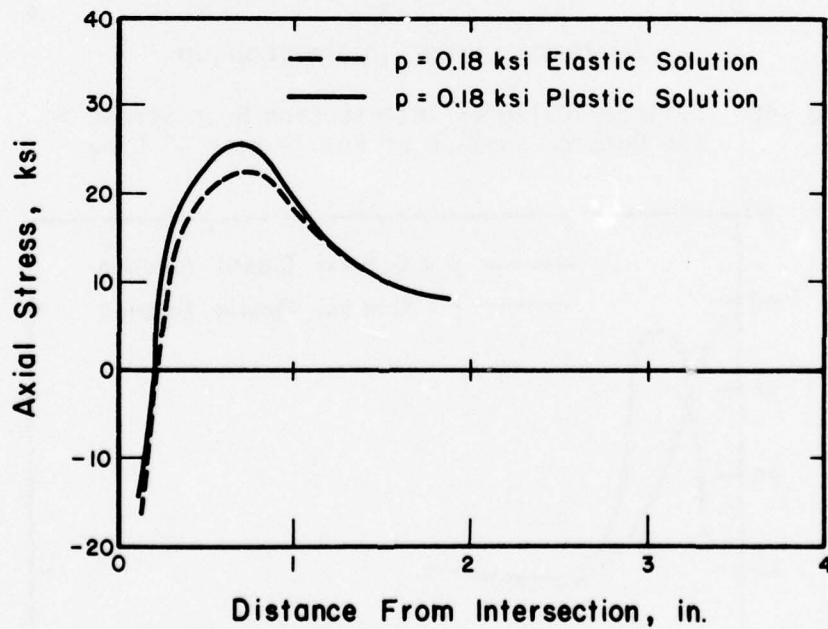
Fig. 45   Cylinder-Cylinder Intersection Axial Stress in the Inside Surface of Cylinder near 0° Line
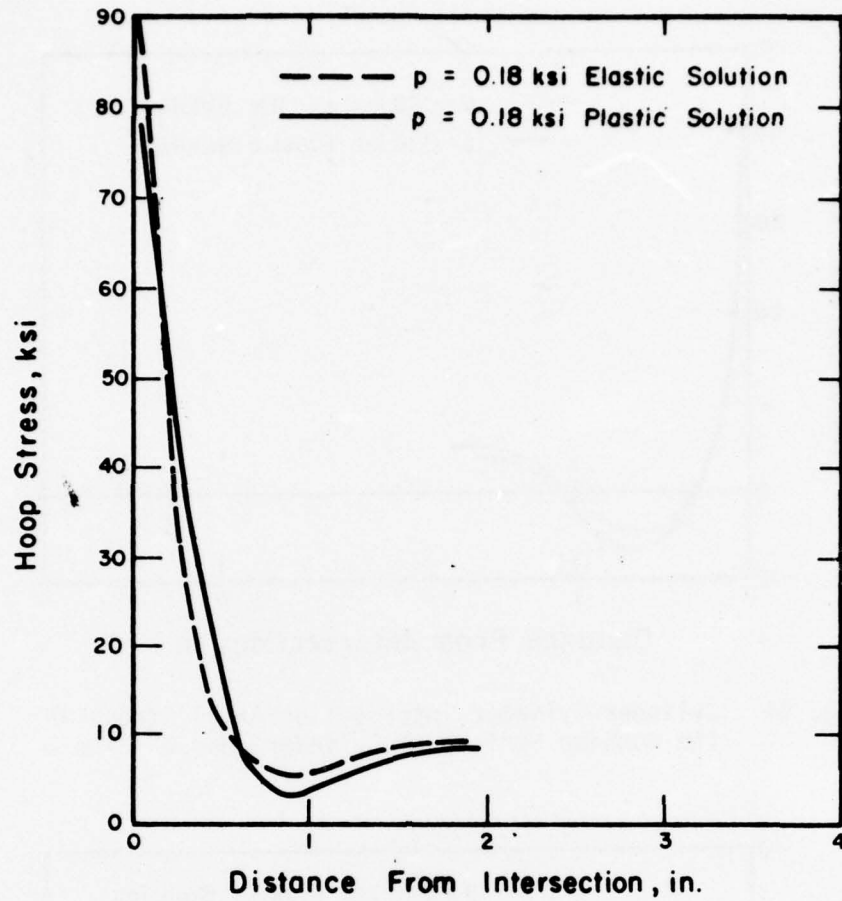
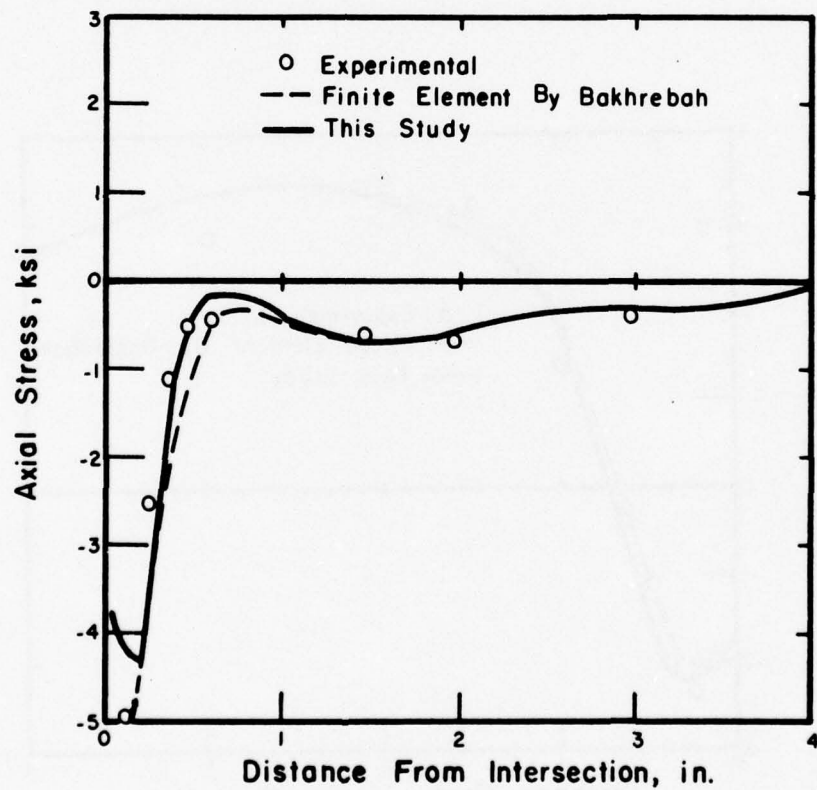Fig. 46 Cylinder-Cylinder Intersection Hoop Stress in the Outside Surface of Nozzle near 0° Line
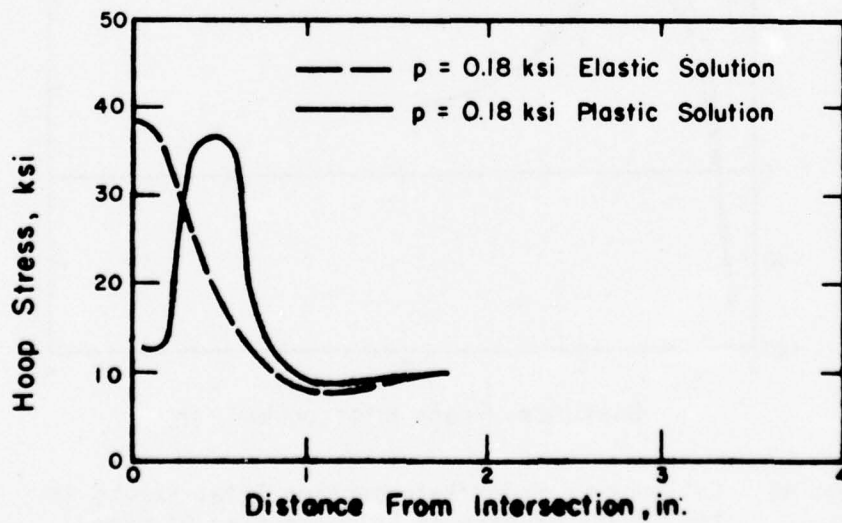
Fig. 47 Cylinder-Cylinder Intersection Hoop Stress in the Inside Surface of Nozzle near 0° Line

113
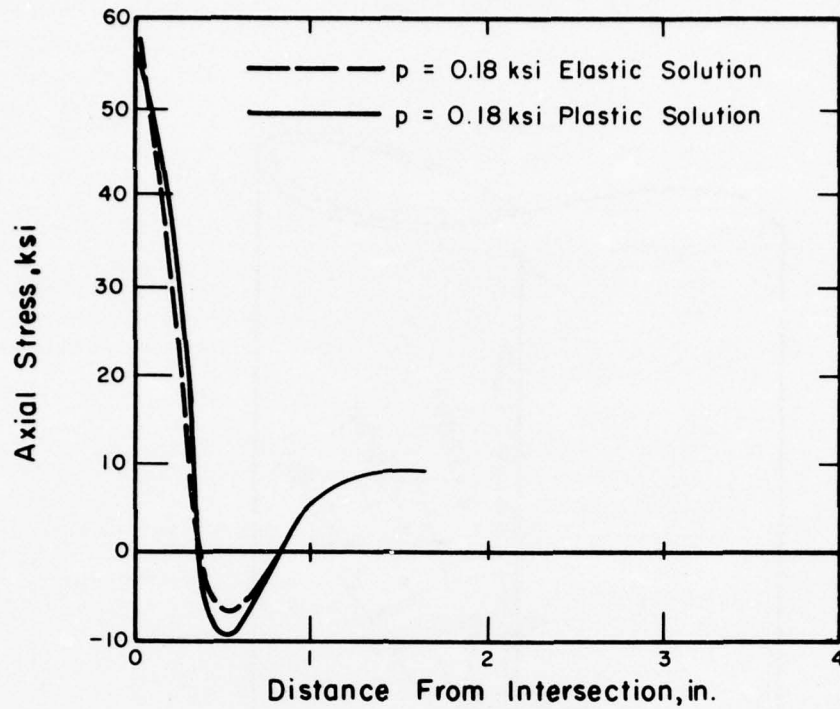
Fig. 48   Cylinder-Cylinder Intersection Axial Stress in
           the Outside Surface of Nozzle near 0° Line
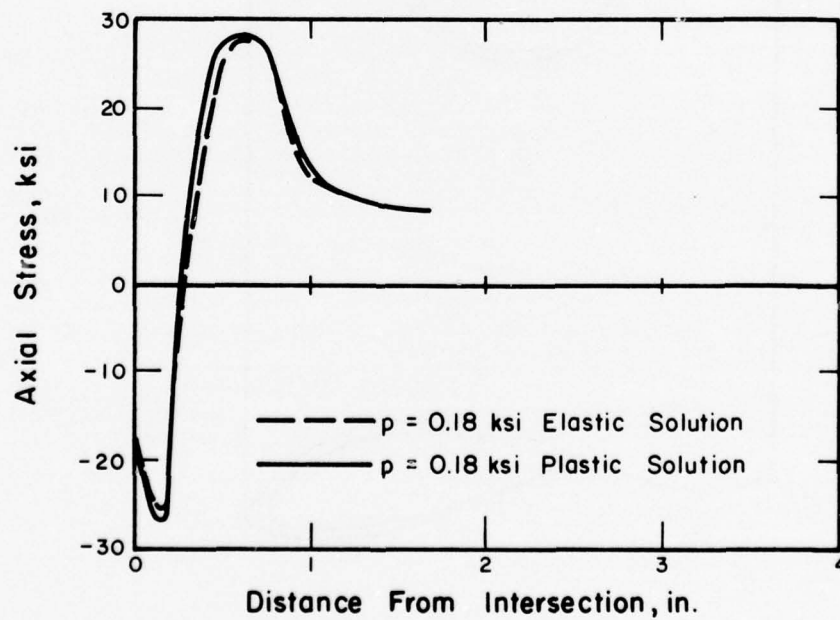
Fig. 49   Cylinder-Cylinder Intersection Axial Stress in
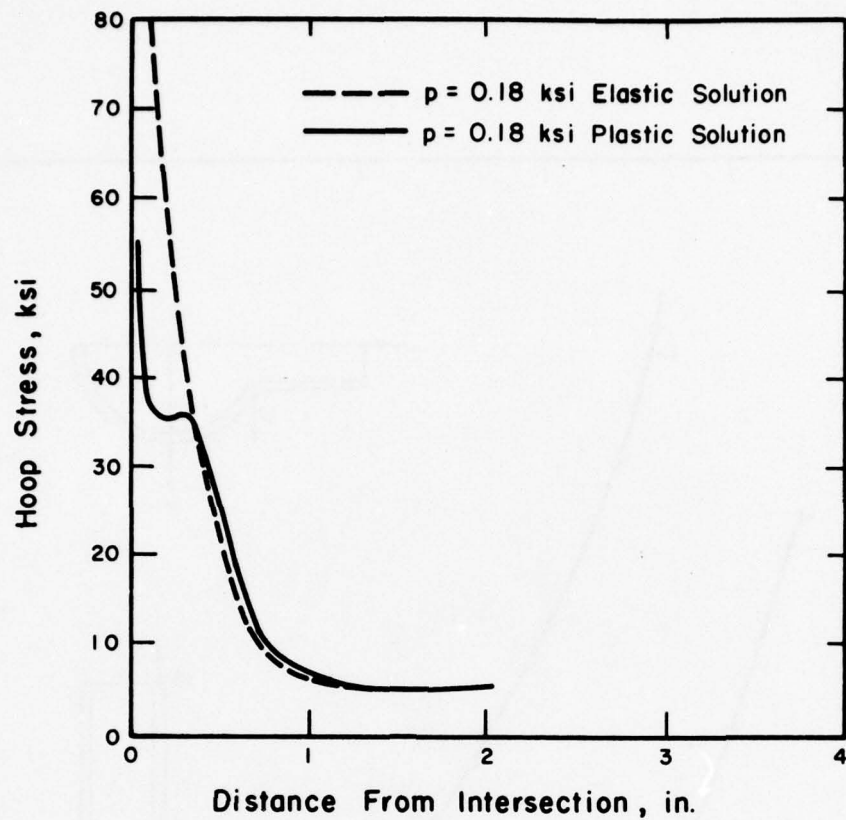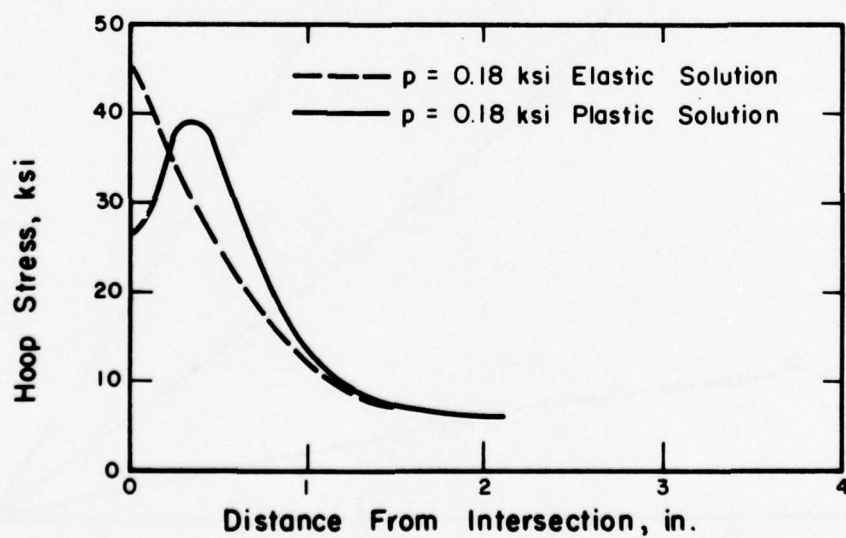   the Inside Surface of Nozzle near 0° Line
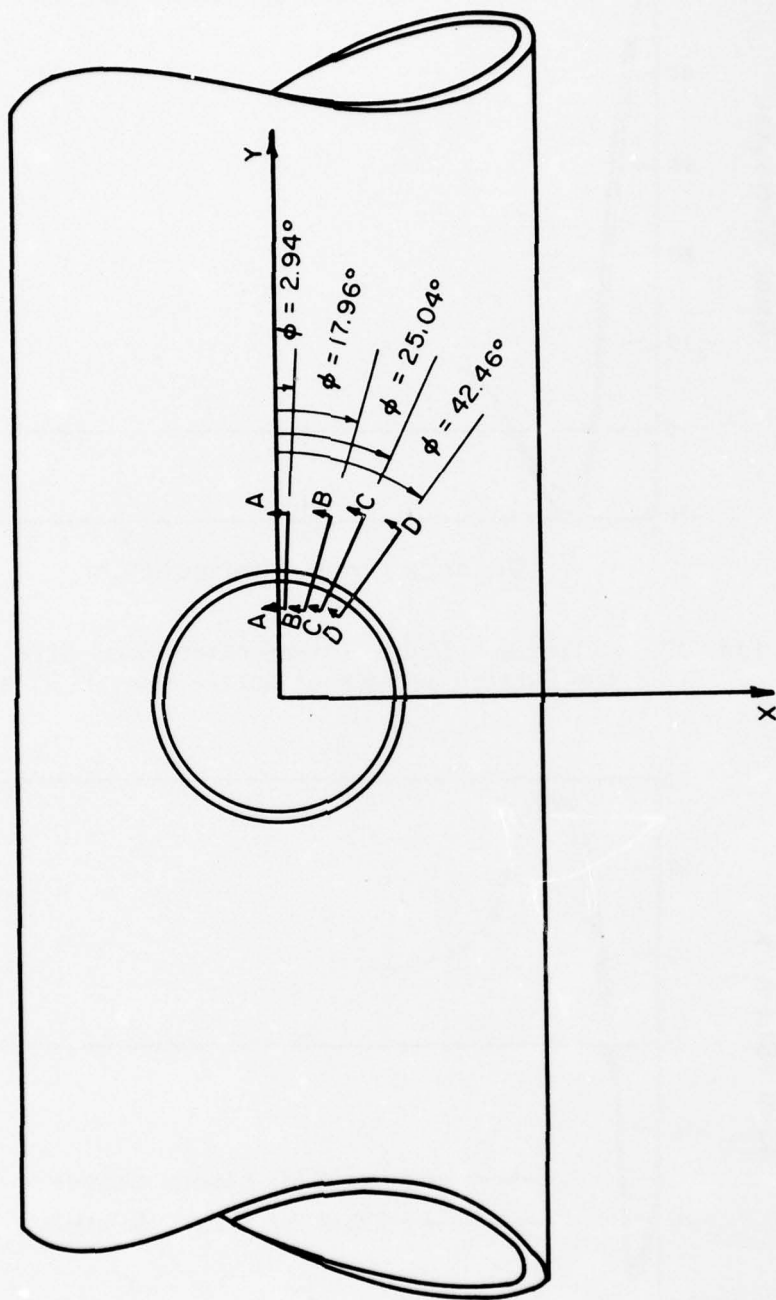
Fig. 50   Locations of Sections A, B, C and D

x   0.11 ksi
●   0.12 ksi
○   0.13 ksi
△   0.15 ksi
□   0.17 ksi
α   0.18 ksi
β   0.2   ksi
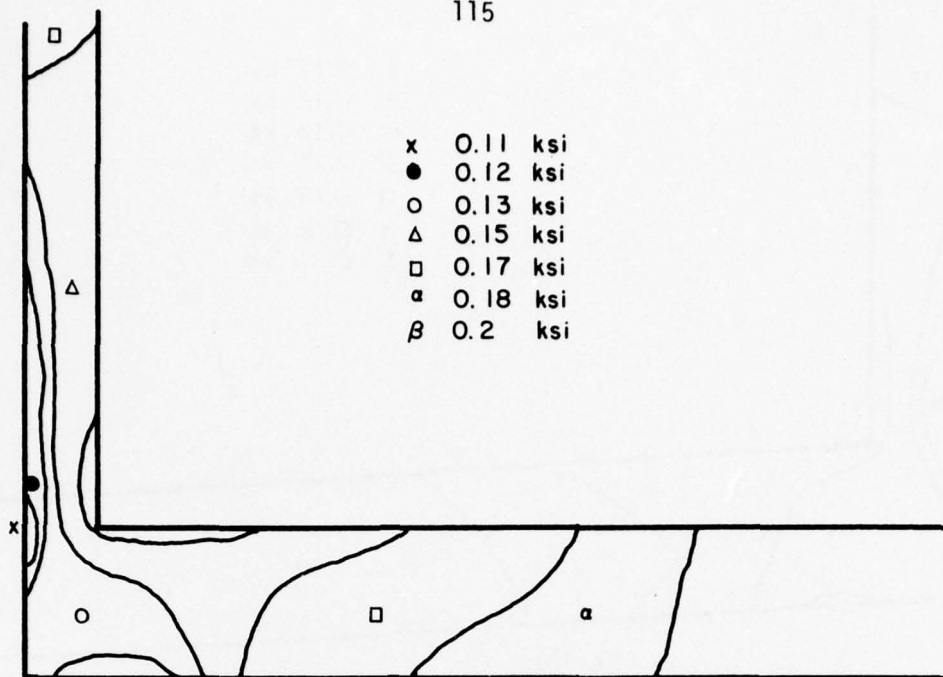
Section A

Fig. 51   Progression of Plastic Region in Section A

x   0.11 ksi
●   0.12 ksi
○   0.13 ksi
△   0.15 ksi
□   0.17 ksi
α   0.18 ksi
β   0.2   ksi
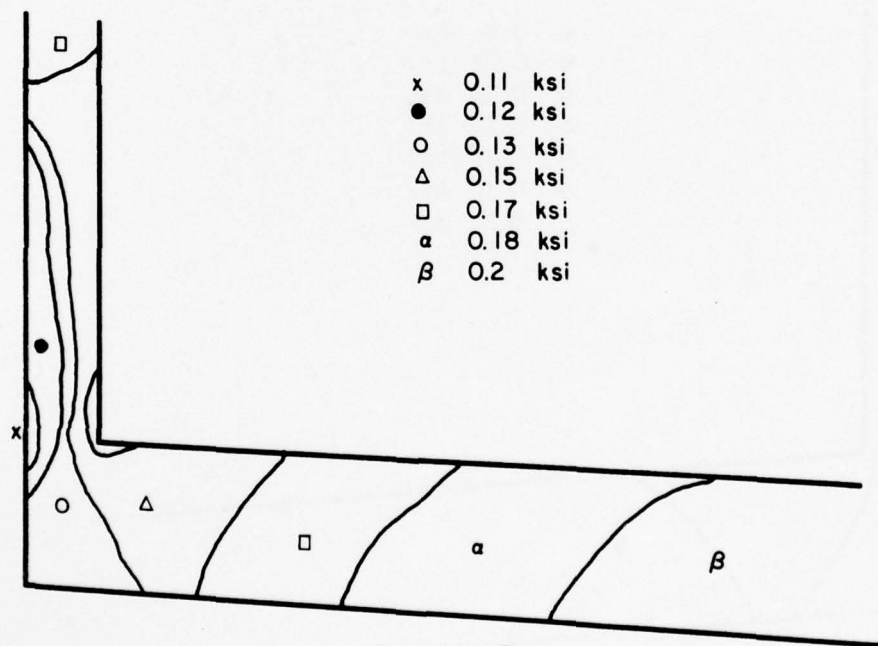
Section B

Fig. 52   Progression of Plastic Region in Section B

116
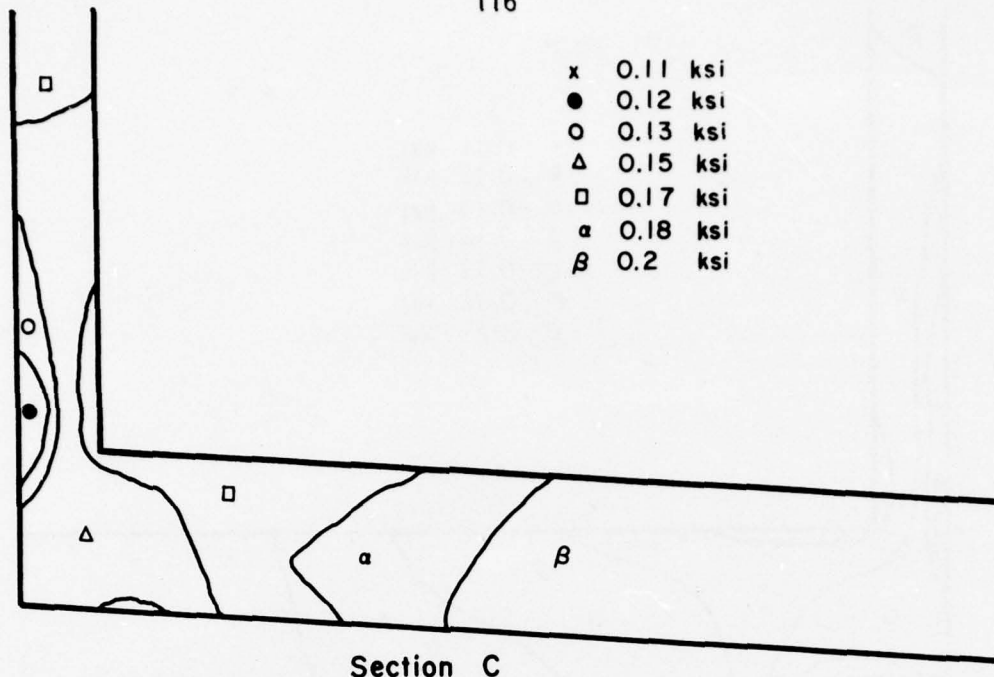
Section C

Fig. 53   Progression of Plastic Region in Section C
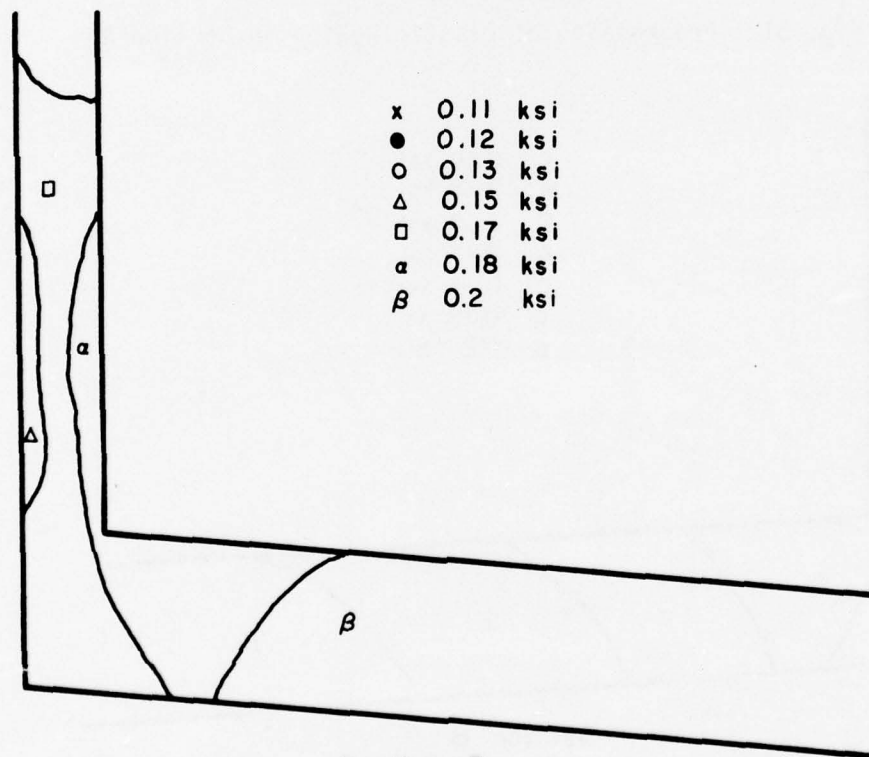
Section D

Fig. 54   Progression of Plastic Region in Section D
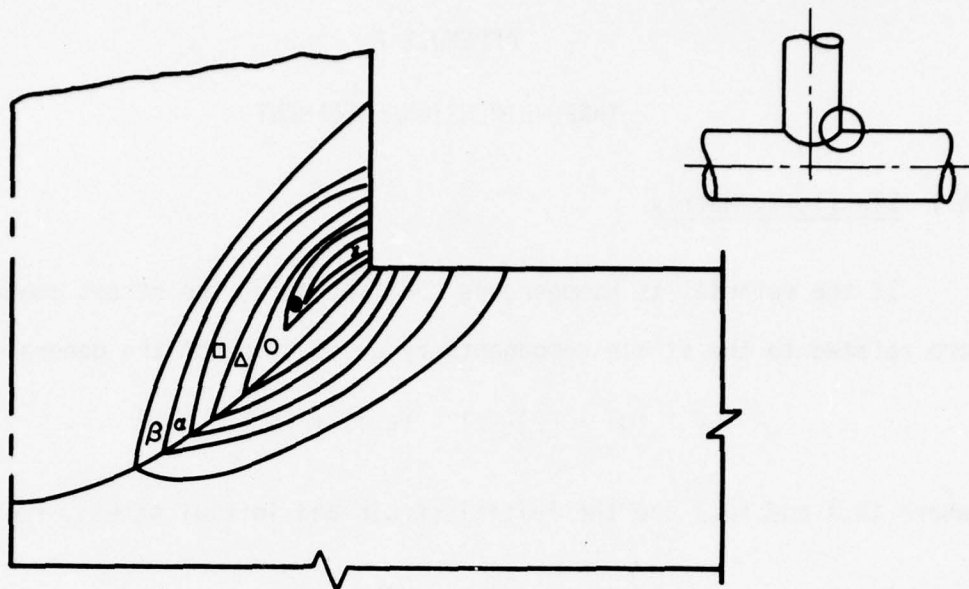
Fig. 55   Progression of Plastic Region on the Inside Surface
of a Cylinder-to-Cylinder Intersection
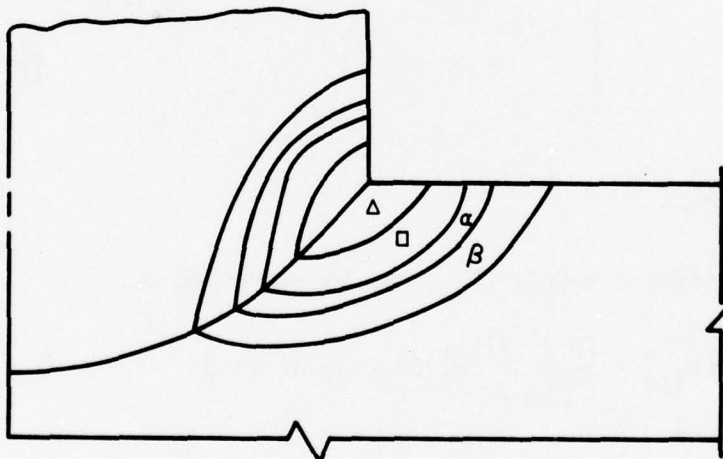
Fig. 56   Progression of Plastic Region on the Outside Surface
of a Cylinder-to-Cylinder Intersection

APPENDIX A

THREE-DIMENSIONAL ELEMENT

A.1 Elasticity Matrix

If the material is homogeneous and isotropic, the stress components are related to the strain components by an equation of the general form.

$$\{\sigma\} = [D](\{\varepsilon\} - \{\varepsilon_o\}) + \{\sigma_o\}$$

where $\{\varepsilon_o\}$ and $\{\sigma_o\}$ are the initial strain and initial stress, respectively.

$$[D] = \frac{E(1-\nu)}{(1+\nu)(1-2\nu)} \begin{bmatrix} 1 & \dfrac{\nu}{1-\nu} & \dfrac{\nu}{(1-\nu)} & \cdot & \cdot & \cdot \\ & 1 & \dfrac{\nu}{(1-\nu)} & \cdot & \cdot & \cdot \\ & & 1 & \cdot & \cdot & \cdot \\ & & & \dfrac{(1-2\nu)}{2(1-\nu)} & \cdot & \cdot \\ & \text{symmetric} & & & \dfrac{(1-2\nu)}{2(1-\nu)} & \cdot \\ & & & & & \dfrac{(1-2\nu)}{2(1-\nu)} \end{bmatrix}$$

A.2 Stiffness Matrix

The nodal stiffness matrix $[K_{ij}]$ can be expressed as:

$$[K_{ij}] = \int_{-1}^{1} \int_{-1}^{1} \int_{-1}^{1} B_i^T \, DB_J \, |J| \, d\xi \, d\eta \, d\zeta$$

3x3

where

$$[B]^T_i = \begin{bmatrix} B_1 & 0 & 0 & B_2 & 0 & B_3 \\ 0 & B_2 & 0 & B_1 & B_3 & 0 \\ 0 & 0 & B_3 & 0 & B_2 & B_1 \end{bmatrix}_i \quad , \quad D = \begin{bmatrix} D_{11} & D_{12} & D_{13} & \cdot & \cdot & \cdot \\ & D_{22} & D_{23} & \cdot & \cdot & \cdot \\ & & D_{33} & \cdot & \cdot & \cdot \\ & & & D_{44} & \cdot & \cdot \\ \text{Symmetric} & & & & D_{55} & \cdot \\ & & & & & D_{66} \end{bmatrix}$$

3×6 $\qquad$ 6×6

$$K_{ij} = \begin{bmatrix} A_{11} & & \text{Symmetric} \\ A_{21} & A_{22} & \\ A_{31} & A_{32} & A_{33} \end{bmatrix}$$

3×3

with

$$A_{11} = \int_{-1}^{1}\int_{-1}^{1}\int_{-1}^{1} (B^T_{1i}D_{11}B_{1j} + B^T_{2i}D_{44}B_{2j} + B^T_{3i}D_{66}B_{3j}) \, |J| \, d\xi \, d\eta \, d\zeta$$

$$A_{21} = \int_{-1}^{1}\int_{-1}^{1}\int_{-1}^{1} (B^T_{2i}D_{21}B_{1j} + B^T_{1i}D_{44}B_{2j}) \, |J| \, d\xi \, d\eta \, d\zeta$$

$$A_{22} = \int_{-1}^{1}\int_{-1}^{1}\int_{-1}^{1} (B^T_{2i}D_{22}B_{2j} + B^T_{1i}D_{44}B_{1j} + B^T_{3i}D_{55}B_{3j}) \, |J| \, d\xi \, d\eta \, d\zeta$$

$$A_{31} = \int_{-1}^{1}\int_{-1}^{1}\int_{-1}^{1} (B^T_{1i}D_{66}B_{3j} + B^T_{3i}D_{13}B_{1j}) \, |J| \, d\xi \, d\eta \, d\zeta$$

$$A_{32} = \int_{-1}^{1}\int_{-1}^{1}\int_{-1}^{1} (B^T_{3i}D_{23}B_{2j} + B^T_{2i}D_{55}B_{3j}) \, |J| \, d\xi \, d\eta \, d\zeta$$

$$A_{33} = \int_{-1}^{1}\int_{-1}^{1}\int_{-1}^{1} (B_{3i}D_{33}B_{3j} + B_{1i}D_{55}B_{2j} + B_{1i}D_{66}B_{1j}) \, |J| \, d\xi \, d\eta \, d\zeta$$

A.3 T3D Transformation Matrix [C]

For the mid-node i, the nodal displacement can be transformed to top and bottom nodes by

$$\begin{Bmatrix} u_i \\ v_i \\ w_i \end{Bmatrix}_{mid} = \frac{1}{2} \left(\begin{Bmatrix} u_i \\ v_i \\ w_i \end{Bmatrix}_{top} + \begin{Bmatrix} u_i \\ v_i \\ w_i \end{Bmatrix}_{bot} \right) = [C] \begin{Bmatrix} u_{i\ top} \\ v_{i\ top} \\ w_{i\ top} \\ u_{i\ bot} \\ v_{i\ bot} \\ w_{i\ bot} \end{Bmatrix}$$

where

$$[C] = \begin{bmatrix} \frac{1}{2} & 0 & 0 & \frac{1}{2} & 0 & 0 \\ 0 & \frac{1}{2} & 0 & 0 & \frac{1}{2} & 0 \\ 0 & 0 & \frac{1}{2} & 0 & 0 & \frac{1}{2} \end{bmatrix}$$

Introducing into [B] formulation, we get

$$[B] \begin{Bmatrix} u_{i\ top} \\ v_{i\ top} \\ w_{i\ top} \\ u_{i\ mid} \\ v_{i\ mid} \\ w_{i\ mid} \\ \overline{U} \end{Bmatrix} = [B][A] \begin{Bmatrix} u_{i\ top} \\ v_{i\ top} \\ w_{i\ top} \\ u_{i\ bot} \\ v_{i\ bot} \\ w_{i\ bot} \\ \overline{U} \end{Bmatrix}$$

where

$$[A] = \begin{bmatrix} \begin{array}{cccccc|c} 1 & 0 & 0 & 0 & 0 & 0 & \\ 0 & 1 & 0 & 0 & 0 & 0 & \\ 0 & 0 & 1 & 0 & 0 & 0 & \{0\} \\ \frac{1}{2} & 0 & 0 & \frac{1}{2} & 0 & 0 & \\ 0 & \frac{1}{2} & 0 & 0 & \frac{1}{2} & 0 & \\ 0 & 0 & \frac{1}{2} & 0 & 0 & \frac{1}{2} & \\ \hline & & \{0\}^T & & & & [I] \end{array} \end{bmatrix}$$

APPENDIX B

AHMAD'S SHELL ELEMENT

B.1 Shape Function

$$
[N^*]_i = \begin{bmatrix} N_i & 0 & 0 & N_i \dfrac{t_i \zeta}{2} \theta_{11} & -N_i \dfrac{t_i \zeta}{2} \theta_{12} \\[2em] 0 & N_i & 0 & N_i \dfrac{t_i \zeta}{2} \theta_{21} & -N_i \dfrac{t_i \zeta}{2} \theta_{22} \\[2em] 0 & 0 & N_i & N_i \dfrac{t_i \zeta}{2} \theta_{31} & -N_i \dfrac{t_i \zeta}{2} \theta_{32} \end{bmatrix}
$$

where $[\theta]$ is defined as

$$
\begin{Bmatrix} x \\ y \\ z \end{Bmatrix}_{global} = [\theta]_i \begin{Bmatrix} x' \\ y' \\ z' \end{Bmatrix}_{i,\ local}
$$

B.2 Material Properties [D']

The [D] matrix for an anisotropic material is constructed in local coordinate system as:

$$
[D] = \frac{E(1-\nu)}{(1+\nu)(1-2\nu)} \begin{bmatrix} 1 & \left(\dfrac{\nu}{1-\nu}\right) & \cdot & \cdot & \cdot \\[1em] & 1 & \cdot & \cdot & \cdot \\[1em] & & \dfrac{1-2\nu}{2(1-\nu)k} & \cdot & \cdot \\[1em] \text{Symmetric} & & & \dfrac{1-2\nu}{2(1-\nu)k} & \cdot \\[1em] & & & & \dfrac{(1-2\nu)}{2(1-\nu)k} \end{bmatrix}
$$

where k is taken as 1.2, as indicated by Zienkiewicz, to construct the same shear strain energies as in real distributions through the thickness of shells.

B.3 [B'] Matrix for Ahmad's Element

$$\{\varepsilon'\}=\begin{Bmatrix} \varepsilon_{x'} \\ \varepsilon_{y'} \\ \gamma_{x'y'} \\ \gamma_{x'z'} \\ \gamma_{y'z'} \end{Bmatrix} = \begin{Bmatrix} u'_{,x'} \\ v'_{,y'} \\ u'_{,y'} + v'_{,x'} \\ w'_{,x'} + u'_{,z'} \\ w'_{,y'} + v'_{,z'} \end{Bmatrix} = [B']\{u\}$$

$$\begin{bmatrix} u'_{,x'} & v'_{,x'} & w'_{,x'} \\ u'_{,y'} & v'_{,y'} & w'_{,y'} \\ u'_{,z'} & v'_{,z'} & w'_{,z'} \end{bmatrix} = [\theta]^T [J^*] \begin{bmatrix} u_{,\xi} & v_{,\xi} & w_{,\xi} \\ u_{,\eta} & v_{,\eta} & w_{,\eta} \\ u_{,\zeta} & v_{,\zeta} & w_{,\zeta} \end{bmatrix} [\theta]$$

where
$$[\theta] = [\overline{v}_1, \overline{v}_2, \overline{v}_3]$$

$$[J^*] = [J]^{-1} \quad , \text{ and}$$

$$\begin{Bmatrix} x \\ y \\ z \end{Bmatrix}_{global} = [\mu]_i \begin{Bmatrix} x' \\ y' \\ z' \end{Bmatrix}_{i, local}$$

The $[B']_i$ for node i can be expressed as:

$$[B']_i = \begin{bmatrix} \theta_{11}a_1 & \theta_{21}a_1 & \theta_{31}a_1 & a'_1 P_1 \frac{t_i}{2} & a'_1 Q_1 \frac{t_i}{2} \\ \theta_{12}a_2 & \theta_{22}a_2 & \theta_{32}a_2 & a'_2 P_2 \frac{t_i}{2} & a'_2 Q_2 \frac{t_i}{2} \\ \theta_{11}a_2+\theta_{12}a_1 & \theta_{21}a_2+\theta_{22}a_1 & \theta_{31}a_2+\theta_{32}a_1 & (a'_2 P_1+a'_1 P_2)\frac{t_i}{2} & (a'_2 Q_1+a'_1 Q_2)\frac{t_i}{2} \\ \theta_{12}a_3+\theta_{13}a_2 & \theta_{22}a_3+\theta_{23}a_2 & \theta_{32}a_3+\theta_{33}a_2 & (a'_3 P_2+a'_2 P_3)\frac{t_i}{2} & (a'_3 Q_2+a'_2 Q_3)\frac{t_i}{2} \\ \theta_{11}a_3 \ \theta_{13}a_1 & \theta_{21}a_3+\theta_{23}a_1 & \theta_{31}a_3+\theta_{33}a_1 & (a'_3 P_1+a'_1 P_3)\frac{t_i}{2} & (a'_3 Q_1+a'_1 Q_3)\frac{t_i}{2} \end{bmatrix}$$

where

$$A_m = J^*_{m1}N_{i,\xi} + J^*_{m2}N_{i,\eta}$$

$$a_m = \theta_{1m}A_1 + \theta_{2m}A_2 + \theta_{3m}A_3$$

$$a'_m = a_m\zeta + (J^*_{13}\theta_{1m} + J^*_{23}\theta_{2m} + J^*_{33}\theta_{3m})\, N_i$$

$$P_m = \theta_{1m}\mu_{11} + \theta_{2m}\mu_{21} + \theta_{3m}\mu_{31}$$

$$Q_m = \theta_{1m}\mu_{12} + \theta_{2m}\mu_{22} + \theta_{3m}\mu_{32}$$

B.4 Shell Transition Element

When the departure concept is incorporated in the two-dimensional curved shell element, the shape functions of the nodes that are intended to be converted then connected to a 3D element can be written as:

for corner nodes, $\xi_i = -1$, $\eta_i \approx \pm 1$

$$N_i = \frac{-1}{4}(1 + \eta_i\eta)(1 - \xi)\,\xi$$

for midside nodes, $\xi_i = -1$, $\eta_i = 0$

$$N_i = \frac{1}{2}(1 - \xi)(1 - \eta^2)$$

The $[B']$ matrix can be obtained by substituting these new shape functions into Eq. (3.29), then use $[B']$ to construct a modified stiffness matrix $[K'_s]$. The stiffness matrix of the shell transition element is obtained by

$$[K_T] = [C_s]^T[K'_s][C_s]$$

where $[C_s]_i$ for node i is defined as

$$
\left\{ \begin{array}{c} u \\ v \\ w \\ \alpha \\ \beta \end{array} \right\}_i = [C_s]_i \left\{ \begin{array}{c} u_{top} \\ v_{top} \\ w_{top} \\ u_{bot} \\ v_{bot} \\ w_{bot} \end{array} \right\}_i
$$

or

$$
[C_s]_i = \begin{bmatrix} \dfrac{1}{2} & 0 & 0 & \dfrac{1}{2} & 0 & 0 \\[2mm] 0 & \dfrac{1}{2} & 0 & 0 & \dfrac{1}{2} & 0 \\[2mm] 0 & 0 & \dfrac{1}{2} & 0 & 0 & \dfrac{1}{2} \\[2mm] \dfrac{v_{11}}{t} & \dfrac{v_{12}}{t} & \dfrac{v_{13}}{t} & \dfrac{-v_{11}}{t} & \dfrac{-v_{12}}{t} & \dfrac{-v_{13}}{t} \\[2mm] \dfrac{-v_{21}}{t} & \dfrac{-v_{22}}{t} & \dfrac{-v_{23}}{t} & \dfrac{v_{21}}{t} & \dfrac{v_{22}}{t} & \dfrac{v_{23}}{t} \end{bmatrix}_i
$$

with

$$
\left\{ \begin{array}{c} x \\ y \\ z \end{array} \right\}_{global} = [\, \bar{v}_1, \, \bar{v}_2, \, \bar{v}_3 \,]_i \left\{ \begin{array}{c} x \\ y \\ z \end{array} \right\}_{i,\ local}
$$

APPENDIX C

VON MISES CRITERION

From the experimental investigations [50], it has been demonstrated that hydrostatic stress does not produce yielding in a ductile material even for very high hydrostatic stress. Based on this fact, the distortion energy theory, or the Von Mises yield criterion, assumes that yielding begins when the distortion energy equals the distortion energy at yield in the simple tension. The distortion energy of a material can be written in general form as:

$$U_d = \frac{1}{2G} J_2 = \frac{3}{4G} \tau_{oct}^2 \qquad \text{(C.1)}$$

with

$$G = \frac{E}{2(1+\nu)}$$

For simple tension, the distortion energy is

$$U_d = \frac{1}{2G} J_2 = \frac{3}{2G} \sigma_o^2 \qquad \text{(C.2)}$$

$$\sigma_o = \text{first initial yield stress of the}$$
$$\text{simple tension}$$

From Eq. (C.1) and Eq. (C.2), we get

$$J_2 = \frac{1}{3} \sigma_o^2 \qquad \text{(C.3)}$$

Since $J = \frac{3}{2} \tau_{oct}^2$, therefore Eq. (C.3) can be written as

$$\tau_{oct} = \tau_{oct, \text{ simple tension}} \qquad \text{(C.4)}$$

Equation (C.4) indicates that yielding occurs when the octahedral shear stress reaches the octahedral shear stress at yield in simple tension. The Von Mises yield criterion usually provides good agreement with experimental data if the material is homogeneous and isotropic.

PART I - GOVERNMENT

Administrative & Liaison Activities

Chief of Naval Research
Department of the Navy
Arlington, Virginia 22217
Attn: Code 474 (2)
471
222

Director
ONR Branch Office
495 Summer Street
Boston, Massachusetts 02210

Director
ONR Branch Office
219 S. Dearborn Street
Chicago, Illinois 60604

Director
Naval Research Laboratory
Attn: Code 2629 (ONRL)
Washington, D.C. 20390 (6)

U.S. Naval Research Laboratory
Attn: Code 2627
Washington, D.C. 20390

Director
ONR - New York Area Office
715 Broadway - 5th Floor
New York, New York 10003

Director
ONR Branch Office
1030 E. Green Street
Pasadena, California 91101

Defense Documentation Center
Cameron Station
Alexandria, Virginia 22314 (12)

Army

Commanding Officer
U.S. Army Research Office Durham
Attn: Mr. J.J. Murray
CRD-AA-IP
Box CM, Duke Station
Durham, North Carolina 27706 (2)

Commanding Officer
AMXMR-ATL
Attn: Mr. R. Shea
U.S. Army Materials Res. Agency
Watertown, Massachusetts 02172

Watervliet Arsenal
MAGGS Research Center
Watervliet, New York 12189
Attn: Director of Research

Technical Library

Redstone Scientific Info. Center
Chief, Document Section
U.S. Army Missile Command
Redstone Arsenal, Alabama 35809

Army R & D Center
Fort Belvoir, Virginia 22060

Navy

Commanding Officer and Director
Naval Ship Research & Development Center
Bethesda, Maryland 20034
Attn: Code 042 (Tech. Lib. Br.)
17 (Struc. Mech. Lab.)
172
172
174
177
1800 (Appl. Math. Lab.)
5412S (Dr. W.D. Sette)
19 (Dr. M.M. Sevik)
1901 (Dr. M. Strassberg)
1945
196 (Dr. D. Feit)
1962

Naval Weapons Laboratory
Dahlgren, Virginia 22448

Naval Research Laboratory
Washington, D.C. 20375
Attn: Code 8400
8410
8430
8440
6300
6390
6380

Undersea Explosion Research Div.
Naval Ship R & D Center
Norfolk Naval Shipyard
Portsmouth, Virginia 23709
Attn: Dr. E. Palmer
       Code 780

Naval Ship Research & Development Center
Annapolis Division
Annapolis, Maryland 21402
Attn: Code 2740 - Dr. Y.F. Wang
             28 - Mr. R.J. Wolfe
            281 - Mr. R.B. Niederberger
           2814 - Dr. H. Vanderveldt

Technical Library
Naval Underwater Weapons Center
Pasadena Annex
3202 E. Foothill Blvd.
Pasadena, California 91107

U.S. Naval Weapons Center
China Lake, California 93557
Attn: Code 4062 - Mr. W. Werback
             4520 - Mr. Ken Bischel

Commanding Officer
U.S. Naval Civil Engr. Lab.
Code L31
Port Hueneme, California 93041

Technical Director
U.S. Naval Ordnance Laboratory
White Oak
Silver Spring, Maryland 20910

Technical Director
Naval Undersea R & D Center
San Diego, California 92132

Supervisor of Shipbuilding
U.S. Navy
Newport News, Virginia 23607

Technical Director
Mare Island Naval Shipyard
Vallejo, California 94592

U.S. Navy Underwater Sound Ref. Lab.
Office of Naval Research
P.O. Box 8337
Orlando, Florida 32806

Chief of Naval Operations
Dept. of the Navy
Washington, D.C. 20350
Attn: Code Op07T

Strategic Systems Project Office
Department of the Navy
Washington, D.C. 20390
Attn: NSP-001 Chief Scientist

Deep Submergence Systems
Naval Ship Systems Command
Code 39522
Department of the Navy
Washington, D.C. 20360

Engineering Dept.
U.S. Naval Academy
Annapolis, Maryland 21402

Naval Air Systems Command
Dept. of the Navy
Washington, D.C. 20360
Attn: NAVAIR 5302 Aero & Structures
              5308 Structures
             52031F Materials
                604 Tech. Library
                320B Structures

Director, Aero Mechanics
Naval Air Development Center
Johnsville
Warminster, Pennsylvania 18974

Technical Director
U.S. Naval Undersea R & D Center
San Diego, California 92132

Engineering Department
U.S. Naval Academy
Annapolis, Maryland 21402

Naval Facilities Engineering Command
Dept. of the Navy
Washington, D.C. 20360
Attn: NAVFAC 03 Research & Development
             04 Research & Development
          14114 Tech. Library

Naval Sea Systems Command
Dept. of the Navy
Washington, D.C. 20360
Attn: NAVSHIP 03 Res. & Technology
             031 Ch. Scientist for R & D
           03412 Hydromechanics
             037 Ship Silencing Div.
             035 Weapons Dynamics

Naval Ship Engineering Center
Prince George's Plaza
Hyattsville, Maryland 20782
Attn: NAVSEC 6100 Ship Sys Engr & Des Dep
6102C Computer-Aided Ship Des
6105G
6110 Ship Concept Design
6120 Hull Div.
6120D Hull Div.
6128 Surface Ship Struct.
6129 Submarine Struct.

Air Force

Commander WADD
Wright-Patterson Air Force Base
Dayton, Ohio 45433
Attn: Code WWRMDD
AFFDL (FDDS)
Structures Division
AFLC (MCEEA)

Chief, Applied Mechanics Group
U.S. Air Force Inst. of Tech.
Wright-Patterson Air Force Base
Dayton, Ohio 45433

Chief, Civil Engineering Branch
WLRC, Research Division
Air Force Weapons Laboratory
Kirtland AFB, New Mexico 87117

Air Force Office of Scientific Research
1400 Wilson Blvd.
Arlington, Virginia 22209
Attn: Machanics Div.

NASA

Structures Research Division
National Aeronautics & Space Admin.
Langley Research Center
Langley Station
Hampton, Virginia 23365

National Aeronautical & Space Admin.
Associate Administrator for Advanced
Research & Technology
Washington, D.C. 02546

Scientific & Tech. Info. Facility
NASA Representative (S-AK/DL)
P.O. Box 5700
Bethesda, Maryland 20014

Other Government Activities

Commandant
Chief, Testing & Development Div.
U.S. Coast Guard
1300 E. Street, N.W.
Washington, D.C. 20226

Technical Director
Marine Corps Dev. & Educ. Command
Quantico, Virginia 22134

Director
National Bureau of Standards
Washington, D.C. 20234
Attn: Mr. B.L. Wilson, EM 219

Dr. M. Gaus
National Science Foundation
Engineering Division
Washington, D.C. 20550

Science & Tech. Division
Library of Congress
Washington, D.C. 20540

Director
Defense Nuclear Agency
Washington, D.C. 20305
Attn: SPSS

Commander Field Command
Defense Nuclear Agency
Sandia Base
Albuquerque, New Mexico 87115

Director Defense Research & Engrg
Technical Library
Room 3C-128
The Pentagon
Washington, D.C. 20301

Chief, Airframe & Equipment Branch
FS-120
Office of Flight Standards
Federal Aviation Agency
Washington, D.C. 20553

Chief, Reserach and Development
Maritime Administration
Washington, D.C. 20235

Deputy Chief, Office of Ship Constr.
Maritime Administration
Washington, D.C. 20235
Attn: Mr. U.L. Russo

4

Atomic Energy Commission
Div. of Reactor Devel. & Tech.
Germantown, Maryland 20767

Ship Hull Research Committee
National Research Council
National Academy of Sciences
2101 Constitution Avenue
Washington, D.C. 20418
Attn: Mr. A.R. Lytle

PART 2 - CONTRACTORS AND OTHER
         TECHNICAL COLLABORATORS

Universities

Dr. J. Tinsley Oden
University of Texas at Austin
345 Eng. Science Bldg.
Austin, Texas 78712

Prof. Julius Miklowitz
California Institute of Technology
Div. of Engineering & Applied Sciences
Pasadena, California 91109

Dr. Harold Liebowitz, Dean
School of Engr. & Applied Science
George Washington University
725 - 23rd St., N.W.
Washington, D.C. 20006

Prof. Eli Sternberg
California Institute of Technology
Div. of Engr. & Applied Sciences
Pasadena, California 91109

Prof. Paul M. Naghdi
University of California
Div. of Applied Mechanics
Etcheverry Hall
Berkeley, California 94720

Professor P.S. Symonds
Brown University
Division of Engineering
Providence, Rhode Island 02912

Prof. A.J. Durelli
The Catholic University of America
Civil/Mechanical Engineering
Washington, D.C. 20017

Prof. R.B. Testa
Columbia University
Dept. of Civil Engineering
S.W. Mudd Bldg.
New York, New York 10027

Prof. H.H. Bleich
Columbia University
Dept. of Civil Engineering
Amsterdam & 120th Streets
New York, New York 10027

Prof. F.L. DiMaggio
Columbia University
Dept. of Civil Engineering
616 Mudd Building
New York, New York 10027

Prof. A.M. Freudenthal
George Washington University
School of Engineering &
   Applied Science
Washington, D.C. 20006

D.C. Evans
University of Utah
Computer Science Division
Salt Lake City, Utah 84112

Prof. Norman Jones
Massachusetts Inst. of Technology
Dept. of Naval Architecture &
      Marine Engrng
Cambridge, Massachusetts 02139

Professor Albert I. King
Biomechanics Research Center
Wayne State University
Detroit, Michigan 48202

Dr. V.R. Hodgson
Wayne State University
School of Medicine
Detroit, Michigan 48202

Dean B.A. Boley
Northwestern University
Technological Institute
2145 Sheridan Road
Evanston, Illinois 60201

Prof. P.G. Hodge, Jr.
University of Minnesota
Dept. of Aerospace Engng & Mechanics
Minneapolis, Minnesota 55455

Dr. D.C. Drucker
University of Illinois
Dean of Engineering
Urbana, Illinois 61801

Prof. N.M. Newmark
University of Illinois
Dept. of Civil Engineering
Urbana, Illinois 61801

Prof. E. Reissner
University of California, San Diego
Dept. of Applied Mechanics
La Jolla, California 92037

Prof. William A. Nash
University of Massachusetts
Dept. of Mechanics & Aerospace Engng.
Amherst, Massachusetts 01002

Library (Code 0384)
U.S. Naval Postgraduate School
Monterey, California 93940

Prof. Arnold Allentuch
Newark College of Engineering
Dept. of Mechanical Engineering
323 High Street
Newark, New Jersey 07102

Dr. George Herrmann
Stanford University
Dept. of Applied Mechanics
Stanford, California 94305

Prof. J. D. Achenbach
Northwestern University
Dept. of Civil Engineering
Evanston, Illinois 60201

Director, Applied Research Lab.
Pennsylvania State University
P.O. Box 30
State College, Pennsylvania 16801

Prof. Eugen J. Skudrzyk
Pennsylvania State University
Applied Research Laboratory
Dept. of Physics - P.O. Box 30
State College, Pennsylvania 16801

Prof. J. Kempner
Polytechnic Institute of Brooklyn
Dept. of Aero. Engrg. & Applied Mech.
333 Jay Street
Brooklyn, New York 11201

Prof. J. Klosner
Polytechnic Institute of Brooklyn
Dept. of Aerospace & Appl. Mech.
333 Jay Street
Brooklyn, New York 11201

Prof. R.A. Schapery
Texas A & M University
Dept. of Civil Engineering
College Station, Texas 77840

Prof. W.D. Pilkey
University of Virginia
Dept. of Aerospace Engineering
Charlottesville, Virginia 22903

Dr. K.D. Schaeffer
University of Maryland
Aerospace Engineering Dept.
College Park, Maryland 20742

Prof. K.D. Willmert
Clarkson College of Technology
Dept. of Mechanical Engineering
Potsdam, New York 13676

Dr. J.A. Stricklin
Texas A & M University
Aerospace Engineering Dept.
College Station, Texas 77843

Dr. L.A. Schmit
University of California, LA
School of Engineering & Applied Science
Los Angeles, California 90024

Dr. H.A. Kamel
The University of Arizona
Aerospace & Mech. Engineering Dept.
Tucson, Arizona 85721

Dr. B.S. Berger
University of Maryland
Dept. of Mechanical Engineering
College Park, Maryland 20742

Prof. G.R. Irwin
Dept. of Mechanical Engineering
University of Maryland
College Park, Maryland 20742

Dr. S.J. Fenves
Carnegie-Mellon University
Dept. of Civil Engineering
Schenley Park
Pittsburgh, Pennsylvania 15213

Dr. Ronald L. Huston
Dept. of Engineering Analysis
Mail Box 112
University of Cincinnati
Cincinnati, Ohio 45221

Prof. George Sih
Dept. of Mechanics
Lehigh University
Bethlehem, Pennsylvania 18015

Prof. A.S. Kobayashi
University of Washington
Dept. of Mechanical Engineering
Seattle, Washington 98105

Librarian
Webb Institute of Naval Architecture
Cresent Beach Road
Glen Cove, New York 11542

Prof. Daniel Frederick
Virginia Polytechnic Institute
Dept. of Engineering Mechanics
Blacksburg, Virginia 24061

Prof. A.C. Eringen
Dept. of Aerospace & Mech. Sciences
Princeton University
Princeton, New Jersey 08540

Dr. S.L.Koh
School of Aero., Astro. & Engr. Sc.
Purdue University
Lafayette, Indiana 47907

Prof. E.H. Lee
Div. of Engrg. Mechanics
Stanford University
Stanford, California 94305

Prof. R.D. Mindlin
Dept. of Civil Engrg.
Columbia University
S.W. Mudd Building
New York, New York 10027

Prof. S.B. Dong
University of California
Dept. of Mechanics
Los Angeles, California 90024

Prof. Burt Paul
University of Pennsylvania
Towne School of Civil & Mech. Engrg.
Rm. 113 - Towne Building
220 S. 33rd Street
Philadelphia, Pennsylvania 19104

Prof. H.W. Liu
Dept. of Chemical Engr. & Metal.
Syracuse University
Syracuse, New York 13210

Prof. S. Bodner
Technion R & D Foundation
Haifa, ISRAEL

Prof. R.J.H. Bollard
Chairman, Aeronautical Engr. Dept.
207 Guggenheim Hall
University of Washington
Seattle, Washington 98105

Prof. G.S. Heller
Division of Engineering
Brown University
Providence, Rhode Island 02912

Prof. Werner Goldsmith
Dept. of Mechanical Engineering
Div. of Applied Mechanics
University of California
Berkeley, California 94720

Prof. J.R. Rice
Division of Engineering
Brown University
Providence, Rhode Island 02912

Prof. R.S. Rivlin
Center for the Application of Mathematics
Lehigh University
Bethlehem, Pennsylvania 18105

Library (Code 0384)
U.S. Naval Postgraduate School
Monterey, California 93940

Dr. Francis Cozzarelli
Div. of Interdisciplinary Studies/Research
School of Engineering
State University of New York
Buffalo, New York 14214

7

Industry and Research Institutes

Library Services Department
Report Section Bldg. 14-14
Argonne National Laboratory
9700 S. Cass Avenue
Argonne, Illinois 60440

Dr. M.C. Junger
Cambridge Acoustical Associates
129 Mount Auburn St.
Cambridge, Massachusetts 02138

Dr. L.H. Chen
General Dynamics Corporation
Electric Boat Division
Groton, Connecticut 06340

Dr. J.E. Greenspon
J.G. Engineering Research Associates
3831 Menlo Drive
Baltimore, Maryland 21215

Dr. S. Batdorf
The Aerospace Corporation
P.O. Box 92957
Los Angeles, California 90009

Dr. K.C. Park
Lockheed Palo Alto Research Laboratory
Dept. 5233, Bldg. 205
3251 Hanover Street
Palo Alto, California 94304

Library Newport News Shipbuilding and
   Dry Dock Company
Newport News, Virginia 23607

Dr. W.F. Bozich
McDonnell Douglas Corporation
5301 Bolsa Avenue
Huntington Beach, California 92647

Dr. H.N. Abramson
Southwest Research Institute
Technical Vice President
Mechanical Sciences
P.O. Drawer 28510
San Antonio, Texas 78284

Dr. R.C. DeHart
Southwest Research Institute
Dept. of Structural Research
P.O. Box 28510
San Antonio, Texas 78284

Dr. M.L. Baron
Weidlinger Associates
Consulting Engineers
110 East 59th Street
New York, New York 10022

Dr. W.A. von Riesemann
Sandia Laboratories
Sandia Base
Albuquerque, New Mexico 87115

Dr. T.L. Geers
Lockheed Missiles & Space Co.
Palo Alto Research Laboratory
3251 Hanover Street
Palo Alto, California 94304

Dr. J.L. Tocher
Boeing Computer Services, Inc.
P.O. Box 24346
Seattle, Washington 98124

Mr. William Caywood
Code BBE, Applied Physics Laboratory
8621 Georgia Avenue
Silver Spring, Maryland 20034

Mr. P.C. Durup
Lockheed-California Company
Aeromechanics Dept., 74-43
Burbank, California 91503

102075

REPORT DOCUMENTATION PAGE

READ INSTRUCTIONS
BEFORE COMPLETING FORM

1. REPORT NUMBER. UILU-ENG-76-2026	2. GOVT ACCESSION NO.	3. RECIPIENT'S CATALOG NUMBER

4. TITLE *(and Subtitle)* NONLINEAR ANALYSIS OF INTERSECTING CYLINDERS BY THE FINITE ELEMENT METHOD.	5. TYPE OF REPORT & PERIOD COVERED Technical Report
	6. PERFORMING ORG. REPORT NUMBER SRS No. 435

7. AUTHOR(s) Hsin-Chang Chen William C. Schnobrich	8. CONTRACT OR GRANT NUMBER(s) N00014-75-C-0164

9. PERFORMING ORGANIZATION NAME AND ADDRESS Department of Civil Engineering University of Illinois at Urbana-Champaign Urbana, Illinois 61801	10. PROGRAM ELEMENT, PROJECT, TASK AREA & WORK UNIT NUMBERS Project No. NR 064-183

11. CONTROLLING OFFICE NAME AND ADDRESS Office of Naval Research, Code N00014 Department of the Navy Arlington, Virginia 22217	12. REPORT DATE December 1976
	13. NUMBER OF PAGES 126

14. MONITORING AGENCY NAME & ADDRESS*(if different from Controlling Office)* Material Science Division Structural Mechanics Division (Code 474) Office of Naval Research (800 Quincy Street) Arlington, Virginia 22217	15. SECURITY CLASS. *(of this report)* UNCLASSIFIED
	15a. DECLASSIFICATION/DOWNGRADING SCHEDULE

16. DISTRIBUTION STATEMENT *(of this Report)*

APPROVED FOR PUBLIC RELEASE: DISTRIBUTION UNLIMITED

17. DISTRIBUTION STATEMENT *(of the abstract entered in Block 20, if different from Report)*

18. SUPPLEMENTARY NOTES

176 010

19. KEY WORDS *(Continue on reverse side if necessary and identify by block number)*

INTERSECTING CYLINDERS; PRESSURE VESSEL;
FINITE ELEMENT METHOD

20. ABSTRACT *(Continue on reverse side if necessary and identify by block number)*

A finite element procedure is presented for the analysis of intersecting cylinders with elastic-plastic behavior. A special layered system is utilized in the region of the intersection where the high stress gradient exists while two-dimensional curved shell elements are used throughout the remainder of the structure, this to minimize computational efforts. A problem of two normally intersecting cylinders under internal pressure is solved. The stresses as the outer and inner fibers of the shells are evaluated and ⟶

DD $\begin{smallmatrix} \text{FORM} \\ \text{1 JAN 73} \end{smallmatrix}$ **1473**   EDITION OF 1 NOV 65 IS OBSOLETE

[20]

compared with available experimental data. It is found that yielding
starts from the region where the two cylindrical walls intersect
perpendicularly, then spreads out along the intersection line with
increased load.